# Experimental Fracture Toughness Of A Lightly Bonded Interface

by

Diana M. Gomez Rodriguez

A thesis
presented to the University of Waterloo
in fulfillment of the
thesis requirement for the degree of
Masters of Applied Science
in
Civil Engineering

Waterloo, Ontario, Canada, 2017

This thesis consists of material all of which I authored or co-authored: see Statement of Contributions included in the thesis. This is a true copy of the thesis, including any required final revisions, as accepted by my examiners.

I understand that my thesis may be made electronically available to the public.

# Statement of Contributions

There are two section within this manuscript that were completed with the help of other authors, they are Appendix B: Conference Publication ARMA 2016 and Appendix C: Non-Destructive Testing Journal Article.

The material presented in Appendix B: Conference Publication ARMA 2016 was co-author by myself, my supervisor and Dr. Robert Gracie. The following manuscript is a verbatim copy of the published material. In this article, Dr. Maurice Dusseault and Dr. Robert Gracie contributed with ideas during the design phase and methodology implementation of the experiment. They provided guidance and feedback during the writing process ranging from technical comments to editing the final copy of the article. The contents of this appendix have been incorporated within a conference proceeding that was published by the American Rock Mechanics Association (ARMA) on its 50$^{th}$ Symposium. Gomez Rodriguez, D. M., Dusseault, M. B., & Gracie, R. (2016). "Cohesion and Fracturing in a Transparent Jointed Rock Analogue". *50th US Rock Mechanics / Geomechanics Symposium*.

The material presented in Appendix C: Non-Destructive Testing Journal Article consists of an article to be presented to the Journal of Geotechniacl and Geoenvironmental Engineering. The following material is a verbatim copy of the article coauthored by myself, my supervisor, Sabah Hassan Fartosy, Dr. Giovanni Cascante, and Dr. Dipanjan Basu. I developed, implemented, and analyzed the results from the methodology for specimen fabrication and fracture growth procedure. Mr. Fartosy developed, implemented, and analyzed the results from the testing set up and methodology for non-destructive testing. During all these phases Dr. Cascante provided great guidance. Dr. Dusseault and Dr. Basu provided further guidance and recommendations to produce a more comprehensive article. The article was written by myself for 30% of the content and 70% by Sabah. He also produced all the final graphs presented in the manuscript. Dr. Cascante, Dr. Basu, and Dr. Dusseault provided feedback and throughout technical and grammatical editing. The contents of this appendix have been incorporated within a journal article that will be submitted for publication in the Journal of Geotechnical and Geoenvironmental Engineering. Hassan, S., Gomez Rodriguez, D., Cascante, G., Basu, D., and Dusseault, M., "Effects of a fracture on ultrasonic wave velocity and attenuation in a homogeneous medium".

# Abstract

The geomechanical behaviour of natural fractured media (NFM) is governed by existing planes of weakness. These planes of weakness can be open fractures, partially closed joints, or cemented veins, and they are classified in groups, joint sets, based on the similarities among them. Some joint sets exhibit cohesion due to infill material emplaced along the walls of the fractures. The geometry of the joint sets in combination with the rigidity of the intact rock allows for shear events to occur when the rock mass is stimulated by hydraulic fracturing. A methodology is produced to create an analogue cohesive fracture within a transparent rock analogue, polymethylmethacrylate (PMMA), and an experimental technique to measure the cohesion or fracture toughness is developed in this study. The methodology is produced to create the cohesive interface is applied by creating cohesive cube specimens to study the interaction the interaction between the hydraulic fracture and the fracture media.

The cohesive interface was achieved using the thermal bonding properties of PMMA where two blocks of the material were fused together at 149˚C (300˚F) under different applied stresses – 6, 12, and 24kPa - and different time intervals – 6, 12, 24, and 48 hours. The specimens were rectangular plates with a circular hole at their center and along the interface. This hole serves as fracture initiation point when subjected to uniaxial load perpendicular to the interface during the fracture toughness test. This test created a controlled fracture where the fracture length increases proportionally to the load increment.

Measurements for the fracture length were taken at different load input levels. This information, along with the specimen geometry, and the load and displacement record, served to calculate the fracture toughness of each specimen using Griffith's principles. The ultimate load approach and the mid-point approach were used to analyze the results from this test. The ultimate load approach provided lower coefficient of variability in the scenarios of thick 25mm specimens than for the thin ones; while the mid-point approach provided lower coefficient of variability for the thin 12mm specimens than the ultimate load approach. This is because the mid-point approach truncates the results to minimize the buckling effect. The thick time variable specimens resulted in low coefficient of variability using both approaches. The time variable testing was stopped at a maximum load close to that corresponding to the midpoint approach. Validation of the compressive test was completed by using the standard Compact Tension (CT) procedure where one of the time variable scenarios was tested. This served to prove that the methodology for creating the annealed surface is reliable and it delivers a weakly bonded interface. Nevertheless, more CT testing is recommended to form a relationship between the uniaxial compression test and the standard CT methodology. Furthermore, an experimental procedure is explained for the hydraulic fracturing emulation using a cohesive cube within a costume made set up.

# Acknowledgements

This thesis and all the hard work could have not been completed without the help and support from many people who encouraged me throughout the duration of this graduate program. I would first like to thank my thesis supervisor Dr. Maurice Dusseault, who provided me with innovating ideas and practical guidance. He consistently allowed this research to be my own work, but steered me in the right direction whenever he thought I needed it. I thank him for his moral support in the struggles I faced and for editing of my work to make it more comprehensible. To my first reader Dr. Robert Gracie who provided me with technical advice throughout this research and for helping me to find solutions when I confronted a setback. I would like to thank Dr. Gracie for all insight he provided during writing this thesis and improvements that resulted from his valuable comments.

I would like to thank the technicians of the different laboratories in the department of Civil Engineering that were involved in this research. Most importantly, I am grateful for all the help of Douglas Hirst who guided me through the experimental implementation of this research, from the design phase to his instructions on how to carry out the test in a safe manner. To Richard Forgett, Fred Bakker, Graeme Addair, Jorge Cruz, and other staff from the Engineering Machine Shop, for their help during the design and construction of the hydraulic fracturing frame, as well as all the material and guidance they provided when I was machining the parts needed to carry out this study. To Jeff Wemp who has provided with the opportunity to work with high speed cameras and other technical advice he has given me. To Giovanni Cascante and Sabah Fartosy for allowing me to collaborate with them in non-destructive research and learn material beyond the scope of this work.

Finally, I must express my very profound gratitude to my friends and family, my parents and sisters, specially to Angelica Stutz and her family for being my family, and to William-Henri Sellier for providing me with unfailing support and continuous encouragement throughout my years of study and through the process of researching and writing this thesis. This accomplishment would not have been possible without them. Thank you.

# Table of Contents

# List of Figures

# List of Tables

# 1 Introduction

Rocks present defects at all scales, from microscopic size such as imperfections in the crystal lattice to kilometers in length such as plate boundaries. A rock mass is composed of a matrix or intact rock and the natural fracture system, this is also known as Natural Fracture Media (NFM) (Blanton, 1982; Zoback, et al., 1977). These systems consist of one or more joint sets. Each joint set represents a group of similar discontinuities such as all of them being joints, fissures, foliation, faults or veins. These discontinuities govern the way that a rock mass behaves. They decrease the strength of the material while increasing its permeability (Bonnet et al., 2001). Likewise, discontinuities reduce the strength and yields failure in metals and other materials used in different applications (Inglis, 1913). Thus, studying these discontinuities, the creation of fractures, and characterizing them provide a greater understanding of their behavior at depth.

The fracture strength within materials is determined by laboratory testing. Furthermore, the strength of the fracture in homogenous materials are evaluated under various standard tests such as the three-point test, the four-point test, the Brazilian Tensional test or the CT test (ASTM INTERNATIONAL, 1997; ASTM INTERNATIONAL, 2001; ASTM INTERNATIONAL, 2016; Hooton, et al., 1997). Each of these test is adequate for testing a certain type of material; the CT test is for metals and the three and four-point test is for brittle material such as concrete and ceramics; while the Brazilian test is commonly used for rocks and to study fracture coalescence. Unfortunately, these tests often create an instantaneous uncontrollable fracture propagation resulting in only one-point result. The collected data in these tests consist of the load at which the material fails and the geometry of the specimen being broken.

Hydraulic fracturing is a complex process which increases the permeability of the stimulated volume of rock mass (Barton, 2014; Gil et al., 2011). This process is important due to the wide variety of applications across different industries. Numerical models help to broaden the understanding of what happens at depth. These numerical models are carried out using simplifications and they are validated with the field data (Jeffrey & Bunger, 2007). Another way to calibrate these models is using physical simulation tests that shares the same simplification. With this purpose, a uniaxial compression frame was designed and built to be used in a physical hydraulic fracturing emulation.

## 1.1 Context

Fracture characterization is an important part of material science. There are various standard tests to characterize fractures in different types of materials such as, the three-point flexural test, the four-point

flexural test, the Izod impact test, the Charpy impact test, the compact Tension (CT) test, and the Brazilian Tensile test. These tests provide different advantages and disadvantages; to minimize these disadvantages, materials with similar rheological characteristics are subjected to the same standard test. Additionally, some of the compressive tests proposed in the literature will be reviewed.

The three-point test (ASTM INTERNATIONAL, 2016) is suited for rigid to semi-rigid materials such as plastics. It delivers a point load along a bar specimen creating a catastrophic failure at the contact point when a maximum load is reached. The fracture toughness is calculated from the catastrophic failure. The four-point test (ASTM INTERNATIONAL, 2010) is similar to the three-point test. This test is good for rigid and semi-rigid materials such as plastics. However, this tests creates a loading area, the fracture grows occurs along this area from a weak point in a catastrophic manner yielding a single point result again. The behaviour of catastrophic failure with a single point result is also typical of impact tests such as the Izod and the Charpy tests. In these cases, the fracture toughness is calculated based on the potential energy from the impacting object.

On the other hand, some pulling tests can achieve a short phase of stable fracture propagation as is the case of the Compact Tension (CT) test. Thus, this test is used in this study for comparison and validation of the results of the proposed compression test. The CT test is usually used to calculate the fracture toughness in mode I of metals. Nevertheless, Jud et al. (1981) completed a series of CT tests using PMMA among other welding polymers and thermal healing. Their study focused on the characterization of the healed interface and comparison between different materials. No stress was applied during the healing process of the specimen preparation. A hot press on the major faces of the specimen were used to anneal the surfaces together. The objective of their work was to compare how far the heat annealed the surface based on the amount of heat exposure measured by the time variable proving their proposed heat dispersion model.

A standard test in the compressive regime is the Brazilian test. This consist of a disk shape specimen loaded at two opposing points on the circumference until catastrophic failure occurs. This test has been used by some studies such as Haeri et al. (2014) or Tang et al. (2001) to study fracture coalescence. These studies focused on how fractures develop from an artificially emplaced notch and how, in some cases, they connect to other notches present within the same specimen. Different notch geometries were considered in both studies. However, the Brazilian test does not develop a controlled fracture and hence, the fracture propagation is studied after catastrophic failure has occurred providing a single point result.

Other non-standard tests have been proposed in the literature which involve different specimen geometry being subjected to compressional forces. Jiefan et al. (1990) study the strain field and failure mechanism

in an uniaxially compressed marble plate of similar geometry as the one proposed here. Jiefan et al. proposed creating a linear notch at the center of the specimen with varying angle between specimens. The material was not transparent, hence back illumination was used to observe the fracture growth. In some cases, they used infill material within the notch to see the effect it has in the fracture development. However, they did not consider this infill material within the fracture but just at the initial point and a cohesive interface was not considered. Transparent material PMMA was used in different non-standard compressive studies. Arruda et al. (1995) uniaxially compressed cubes of the intact preheated PMMA material at low strain rates. The heating preparation temperature ranged from room temperature to the glass transition temperature. The study focused on the strain and temperature dependency of failure of PMMA by closely analyzing the stress-strain relations. On the other hand, Ayatollahi et al. (2015), studied the fracture mechanics of PMMA under uniaxial compression at room temperature under low strain rates. This study involved a non-traditional specimen geometry named v-notch step cottage geometry with a v-notch on the side of the specimen. The v-notch permitted the loading stress to concentrate at the acute end of the notch and initiate fracture that propagated perpendicular to the loading direction. This study however, did not considered an annealed interface as the previously mentioned studies did.

Hydraulic fracturing is a technology used in a variety of disciplines such as waste management and the oil and gas industry. Hydraulic fracturing is a natural phenomenon that occurs in the mid ocean ridge and it forms dykes and sills (Motoki & Sichel, 2008). In waste management, the hydraulic fracture is used to store waste material at depth. It is created by injecting the fracturing fluid mixed with finely crushed waste into the desire formation for long periods of time. In the oil and gas industry, it is used to enhance the permeability of the rock mass in tight formations and help achieve a higher recovery factor in the reservoir. The hydraulic fracturing technique has helped to develop new resource fields which previously were not economically feasible such as are oil shale and shale gas.

The first time this technology was used was as an experimental test in 1947 (King & Corporation, 2012). It was not until 1949 when the first commercial application occurred by Halliburton, then a cementing company that was license for the use of this technology. The original technique was applied to over 350 wells within the first year yielding about a 75% increase in production (Montgomery et al., 2010). This favorable production increase resulted in the frequent use of hydraulic fracturing over the next decades and widespread interest to advance the technique for improved results. Hydraulic fracturing is a complex process that results from the interaction of various factors, such as the in-situ conditions of the location to be stimulated, the geomechanical properties of the rock mass, the fracturing fluid properties, rate of injection and pressurization, and many other variables. (Hubbert & Willis, 1972). For this reason, hydraulic fracturing is widely used as well competition technique that is extensively researched.

Experimental work was carried out at the early stages of this technology (Hubbert & Willis, 1972; Papadopulos, et al., 1973; Rubin, 1983; Zoback et al., 1977). The high financial and time cost make this research approach less desirable than using numerical models such as computer simulations. These numerical models provide an insight of what happens at depth during the implementation of this technique. They are developed using simplifying assumptions that allow us to run these simulations in a timely manner. These models are built with a specific focus and field data collected from fracturing jobs that share this focus are used to calibrate these models. Laboratory experimental data using the same simplifying assumptions would be a good method for the calibration of these numerical models. Unfortunately, this is not frequently done due to the scarcity of experimental results.

## 1.2 Research Motivation

Discontinuities in the rock mass generate a large degree of anisotropy in their geomechanical behavior. Their behavior is governed by the characteristics of these discontinuities such as the level of cohesion within the fracture, the level of roughness along the fracture walls, the discontinuity orientation, geometry, and scale, among other factors. Large to medium size discontinuities play an important role in the geomechanical behavior of the rock mass are not well represented in core specimens or small samples taken onsite. Additionally, the integrity of these samples is uncertain as low cohesion between fracture walls would be lost due to deterioration of the sample from the retrieval process. Furthermore, the wide range of scale of fractures makes it difficult to obtain a representative element volume (REV) that can be tested in the laboratory. A REV is the minimum volume of a composite material, such as rock mass, that produces values of characteristics that represent the rock mass. Hence, analogues are used to better understand the material properties and behavior of the intended site. Rock analogues can be attained from retrieving larger specimens from a similar rock composition and joint geometry from another more accessible location. However, testing of these specimens is costly due to their large volume. Hence, a good alternative is to create analogues in the laboratory that suits the specimen size and provides a way to study these discontinuities. For this reason, this research looks to create a methodology to create an analogue weakly bonded interface. The chosen material was a colourless and transparent polymer with the ability to self-bond under the right conditions. Furthermore, testing of these fractures is generally completed using standard test that delivers catastrophic failure and only one point information. Few standard testing procedures allow for the visualization of a propagating fracture front. A test that produces a fracture of stable propagation was desirable to see and better understand the fracture front geometry as well as the energy used to open the fracture.

Additionally, hydraulic fracturing has been widely performed for many years with partial knowledge of what happens at depth. The complexity of the hydraulic fracturing process and the different unknowns and uncertainties of the rock mass makes it difficult to fully model this technique. Some of these uncertainties are, for example, the geomechanical properties derived from samples taken from the formation at depth and the integrity of the rock samples due to the destressing process. The representativeness of the sample is disputed when compared to the rock mass, this is an issue of scale. Similarly, the state of natural fractures at depth are unknowns. Therefore, models have intrinsic assumptions that makes them manageable and, hence, they must be calibrated to recorded data. Simplified numerical models have been created throughout the years and they provide us with insight information and better understanding of this technique (Gil et al., 2011). These models use the recorded data from the field and compares it to the results of the model in attempt to calibrate said models. A useful way to calibrate numerical models is to use experimental data collected from running simplified representation of hydraulic fracturing, using similar assumption to those in the numerical models. This was carried out by some authors but it is not commonly done. Most research efforts have been put into numerical modelling and experimental modelling has been eluded due to its high financial and timely cost. Additionally, questions of their validity when compared to a full scale hydraulic fracturing job are raised due to scale and other restrictions. The focus of this research is to provide a better insight in the interaction between the new hydraulic fracture with a cohesive fractured medium rock mass analogue made using PMMA and the proposed methodology for surface annealing process.

## 1.3 Research Objective

In this research, a methodology to create and evaluate a weakly bonded cohesive surface was developed. A procedure to create a hydraulic fracturing emulation using the bonding methodology is also presented. These are three main objectives that were considered for this research:

1. **Cohesive Analogue Interface:** Develop a methodology for creating a weakly bonded surface in a rock analogue.

2. **Stable Fracture Propagation Test:** Develop an experimental methodology for the evaluation of fracture toughness of interfaces in which fracture propagate in a stable manner.

3. **Hydraulic Fracturing Emulation:** Develop an experimental methodology to study the interaction of a hydraulic fracture with weakly bonded surface in a 3D rock analogue specimen.

**Cohesive Analogue Interface:** The homogeneous material used to develop this methodology is a plastic known as polymethylmethacrylate (PMMA) which is readily available, elastic, strong, transparent and has been used in several previous studies. This material has the property to fuse with itself through thermal annealing. Using this property, a methodology is developed to create rectangular slabs of PMMA containing a single weakly bonded interface. This can serve as analogue for weakly cemented joints in the rock mass. The transparency of the interface, the medium and the control growth serves to create a visual fracture propagation in real time. This methodology can be applied to create specimens used for testing and studying the influence of planes of weakness in the rock mass such as flow through fractured media or the interaction with a hydraulic fracture.

**Stable Fracture Propagation Test:** The proposed testing procedure must allow for controlled fracture growth in a compression regime. This compression produces a quasi-static fracture propagation along the interface where the characterization is desirable. The annealed specimens were subjected to uniaxial load similarly to the way a fracture would develop in rocks at depth. This test characterizes the cohesion level of the annealed fabricated interface. In this study, intact specimens of PMMA are also tested using the uniaxial compression procedure for comparison purposes. Compact Tension (CT) testing is performed to validate the proposed procedure and compare results.

**Hydraulic Fracturing Emulation:** A uniaxial transparent compression frame was designed and constructed to appreciate the interaction between a new hydraulic fracture and the cohesive fracture media. The presented experimental procedure serves as a basis for emulations that concentrate on studying this interaction. The cohesive analogue plane methodology is applied in the 3D specimen preparation. Some considerations for the design of this frame is the ability to host different specimen sizes to be tested ranging from 15cm to 50cm per side cubes. Another consideration was to create a frame that would be versatile enough to be converted into a biaxial and possibly triaxial compression frame. This can be achieved with further design and a given specimen external dimensions. A digital way to measure the fracture opening was also desired.

## 1.4 Research Scope and Limitations

The scope of this study includes the investigation of an annealed interface in PMMA and the degree of cohesion for a thermally bonded interface produced under different conditions. The conditions considered during this research are different specimen thickness in the geometry, different thermal healing stresses

and different thermal healing times. Only applied stresses of up to 24kPa were studied as having significantly larger stress would require a different set up. Similarly, only one temperature was used in the generation of these interfaces. The temperature used here is slightly lower than the melting point of the material but close enough to produce partial melting and weak bonds. The geometry of the specimens consisted of a rectangular plate shape with a single interface. Double interface specimens were not considered for the fracture toughness study due to their higher complexity factor.

The cohesion between the walls of the surface was characterized by a uniaxial compression test that created a fracture in a stable propagation. The test was carried out in displacement controlled compression frame at a slow strain rate. Specimens were tested to characterize the material properties, and the cohesion of the annealed interface. Griffith's theorem was used to evaluate the fracture toughness of each specimen. Photoelasticity was conducted in some specimens to better understand the behavior of the propagating fracture. Also, a series of compact tension (CT) testing was carried out for a single set of conditions to validate the annealed methodology and to compare results between the proposed uniaxial compression test and the CT standard test.

Furthermore, a hydraulic fracture emulation was intended, for this a methodology was establish. This encompass to create a uniaxial compression test capable of testing different sizes of specimens, a compressive and an injecting fluid system, and an experimental procedure to carry out the emulation. The specimens were created using the annealing methodology.

## 1.5 Thesis Overview

This manuscript is broken down into different chapters and appendices. There are 6 chapters in total including the introduction as the first chapter and conclusions and recommendations as the last chapter.

Chapter 2 is the methodology developed to complete the research presented in this manuscript. This takes into consideration the production of single interface samples using different geometries, pressures, and times. It also presents the development of the fracture toughness experimental set up, including a short photo-elasticity study, and calculation of results. This chapter includes the methodology for the compact tension (CT) testing included in the study to validate the strength of the created bond and the proposed testing methodology.

Chapter 3 is dedicated to presenting the results of the controlled stable fracture propagation. Two approaches are presented in this study to evaluate the results, the ultimate point approach and the mid-point approach. A statistical summary of the 61 specimens tested in this research is presented analyzed through both approaches.

Chapter 4 presents the discussion of the results, including the errors and limitations of the annealing methodology and the stable fracture propagation test. One of the errors discussed in this section is buckling and its effects on the results using both approaches. This chapter has a summary of the journal article written in collaboration with Sabah Fartosy, Dr. Giovanni Cascante, Dr. Maurice Dusseault and Dr. Dipanaja Basu.

Chapter 5 encompasses the application of the bonding methodology in a hydraulic fracturing emulation. For this experiment, a uniaxial frame was designed and built, the compression system and fluid injection system were acquired, calibrated and put together. Visual digital calibration for the fracture opening was completed, as well as the specimen preparation. However, this research is still ongoing and no results have yet been produced.

Chapter 6 is the conclusions and recommendations. This is a summary of the finding of this research and it also considers recommendations of the work ahead. The list of references used in this research appears after chapter 6.

Lastly, a series of appendices have been prepared to supplement this manuscript. Appendix A is accompanying information to the work described in the main body. This includes photos of the tested specimens and information on each specimen, as well as, summary information for both approaches and Euler's calcula. Appendix B is a conference article in collaborations with Dr. Maurice Dusseault and Dr. Robert Gracie presented at the 50$^{th}$ American Rock Mechanics Association (ARMA) in Houston Texas in 2016. Ultimately, Appendix C is a journal article to be submitted about non-destructing testing prepared by Sabah Hassan Fartosy, Dr. Giovanni Cascante, Dr. Maurice Dusseault, and Dr. Dipanjan Basu.

# 2 Methodology

## 2.1 Specimen Preparation

A total of 63 PMMA specimens were prepared and tested in this study of which 61 specimens were in annealed condition and 2 specimens were intact. These specimens were categorized in eleven different scenarios based on their geometry and thermal bonding conditions as shown in Table 1. The first scenario – SC00 – consisted of two intact specimens cut from a solid 25 mm thick sheet of PMMA. These two specimens were rectangular prisms of dimensions 152 mm long and 101 mm wide. Similarly, all other 61 specimens have the same outer dimensions and an annealed interface located at 50 mm width. These annealed specimens were categorized in ten different scenarios including the 9CT scenario used for calibration.

Table 1: Deterministic characteristics studied during this test. Scenario 0 consist of two intact specimens used to assess the qualities of PMMA.

<table>
<tr><th>Scenario</th><th>Samples</th><th>Mass</th><th>Pressure</th><th>Thickness</th><th>Time</th><th>Temp</th></tr>
<tr><td>0</td><td>2</td><td colspan="2">Solid</td><td>1 in<br>25.4mm</td><td colspan="2">Intact</td></tr>
<tr><td>1</td><td>7</td><td>1 kg</td><td>6 kPa</td><td rowspan="3">½ in<br>12.7mm</td><td rowspan="4">6 hours</td><td rowspan="10">300 °F<br>149 °C</td></tr>
<tr><td>2</td><td>6</td><td>2 kg</td><td>12 kPa</td></tr>
<tr><td>3</td><td>6</td><td>4 kg</td><td>24 kPa</td></tr>
<tr><td>4</td><td>6</td><td>2 kg</td><td>6 kPa</td><td rowspan="6">1 in<br>25.4mm</td></tr>
<tr><td>5</td><td>6</td><td>4 kg</td><td>12 kPa</td></tr>
<tr><td>6</td><td>6</td><td>8 kg</td><td>24 kPa</td></tr>
<tr><td>7</td><td>6</td><td rowspan="4">8 kg</td><td rowspan="4">24 kPa</td><td>12 hours</td></tr>
<tr><td>8</td><td>6</td><td>24 hours</td></tr>
<tr><td>9</td><td>6</td><td>48 hours</td></tr>
<tr><td>9CT</td><td>6</td><td>48 hours</td></tr>
</table>

The first three scenarios – SC01, SC02 and, SC03 – are made out PMMA sheets of 12 mm (½″) thickness, making in total 19 thin specimens. The thin specimens were prone to buckling and as result, all other specimens were made with thicker material. This thickness increase significantly decreased the amount of buckling and provided more accurate fracture toughness values. In total, the following six scenarios of annealed specimens – SC04, SC05, SC06, SC07, SC08, SC09 and SC09CT – account for a total of 42 specimens made from 25 mm (1″) thick PMMA sheet. SC04, SC05, and SC06 - consisted of the same bonding conditions as those of SC01, SC02, and SC03, but with thicker specimens. To maintain these same bonding conditions, the load input was double so that the applied bonding stress remained the same. The values of fracture toughness averages among the pressure variant tested scenarios had similar results.

Hence, SC07, SC08, and SC09 were bonded under longer thermal healing times and the same stress condition as that of SC06. All scenarios with exception of SC09CT were tested using the proposed uniaxial compression approach presented in this study. Furthermore, a standard compact test - SC09CT - was completed in accordance to the ASTM D5045 and ASTM E399 guidelines for validation and comparison with the results of this study. The methodology carried out for this scenario will be discussed in detail at the end of this section.

All annealed specimens presented in this study were subjected to thermal bonding. This consists of putting two pieces of PMMA of 152 mm long and 50 mm wide in direct contact with each other in an oven under some bonding stress for a determined time as dictated by a given scenario. For all pieces being prepared, the surfaces B in the specimen schematic presented Figure 1 were milled and grinded to ensure a smooth contact surface and smooth loading surface of the specimen. The two pieces to be bonded were put adjacent to each other are held together sideways in a steel frame jig, as illustrated in Figure 1, so that the applied stress occurs at the contact surface to be annealed. This set up consists of two L-shape steel plates clamped together adjacent to faces A on Figure 1. Subsequently, the two pieces of PMMA and the steel set up are put within a cold oven to continue with the loading step. A 25 mm or 12 mm steel square bar– depending on the thickness of the pieces - is placed on top of the bonding specimen and the dead weights are balanced on top of this bar. The placement of the bar ensures that the stress caused by the dead weights and gravity is distributed equally across the contact surface and the specimen only and not carried by the steel frame. The dead weight is place per scenario condition requirements for which the specimen is being prepared. The oven is closed and turned on to 149 ˚C or 300 ˚F and the assembly stays in the oven for a given time dictated by the scenario for which the specimen is being prepared. Once this time has been completed, the oven is turned off and the oven doors are open to decrease the temperature inside the oven and of the specimens. The steel frame with the loaded specimen remains in the cooling oven until room temperature has been reached. This prevents rapid cooling and debonding due to thermal shrinkage. Once the set up is cooled, the dead weights and square bar are removed from the set up, the set up is removed from the oven, and the annealed specimen is retrieved from the set up. A visual inspection is performed of the annealed interface to ensure complete adhesion of the contact surface. The annealed and intact specimens are then taken to the mill machine to smooth surface C in the specimen schematic Figure 1. This surface will be used as the loading surface during testing; smoothing it decreases the friction between the specimen and the loading frame and reduces the likelihood of friction effect in the results. Additionally, this step ensures that all specimens have the same dimensions and this surface is perpendicular to the annealed surface. Once all specimens measure the same dimension, the six specimens of scenario SC09CT are set apart for further milling. All other specimens to be tested under uniaxial compression have a central 6 mm diameter hole. This hole cuts through the annealed interface

and it extends throughout the thickness of the specimen. Due to this center hole, the stress concentrates immediately around the cavity. Thus, at the vertex of the central hole and the annealed interface serves as fracture initiation point during the fracture propagation test. Interestingly, the fracture initiation point for the solid specimens occur at this same location. Once the center hole was in place, the specimens' annealed surface is inspected to identify the possible damage from drilling the hole as shown in Figure 1.

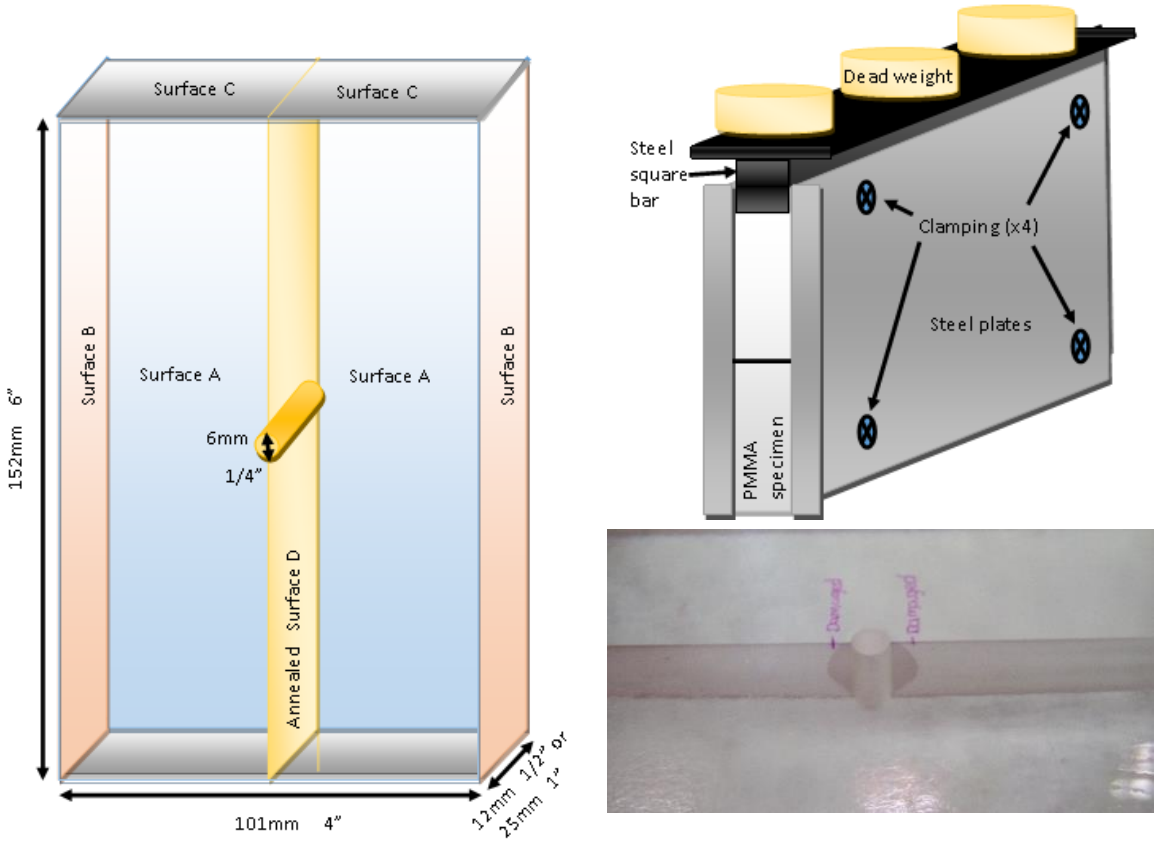


Figure 1: Left, schematic of specimen to be annealed showing the different surfaces. Top right, typical specimen in steel frame jig stress chamber in the oven during cooling phase immediately after thermal bonding is completed but before retrieving from the oven. Bottom right, typical damage arising from specimen preparation emplacement of the center hole.

## 2.2 Testing Set Up and Calculations

This subsection describes the proposed uniaxial compression test presented in this study. For a description of the compact tension test performed to validate the proposed test please refer to the next subsection.

Two uniaxial compression frames were used for testing all the specimens for scenarios SC00 to SC09, these are the MTS 810 and the MTS 322. The MTS 810 is a smaller frame with a maximum load output

of 100 kilo Newton (kN) which is preferred for testing the thin – 12 mm or ½″ – specimens (Material Testing Systems, 2006). The thick – 25 mm or 1″ – specimens were tested using the MTS 322 as the maximum load output is 250 kN (Material Testing Systems, 2009). To ensure no bias or discrepancies from the change of loading frame, extra specimens from SC02 were tested in the MTS 322. There were no differences in results between the specimens tested in the different frames. Only six specimens were considered in this study for this scenario and they were chosen based on their geometry, those with the closest length to 150 mm (6″) were included. These frames were put in displacement control at a rate of 0.1mm/min. The frames recorded the displacement input in mm and resulting load input in kN every 0.5 secs for the duration of the test.

Once the specimens were approved for testing per the establish criteria – little to no damage - and the respective frame was chosen, a closer inspection was performed by measuring the specimen in all its dimension and recording any damage cause by the specimen preparation process. At this point, a first photograph of the specimen was taken and then the specimen was placed in the frame and under the actuator. The actuator was lowered to approach contact with the specimen. The frame measurements are zeroed and specimen is preloaded to 0.5 kN. The test starts when the actuator commences to displace to compress the specimen and the frames. Simultaneously, the frame records the displacement (mm) and load (kN) data and plots on a graph as illustrated in Figure 2.

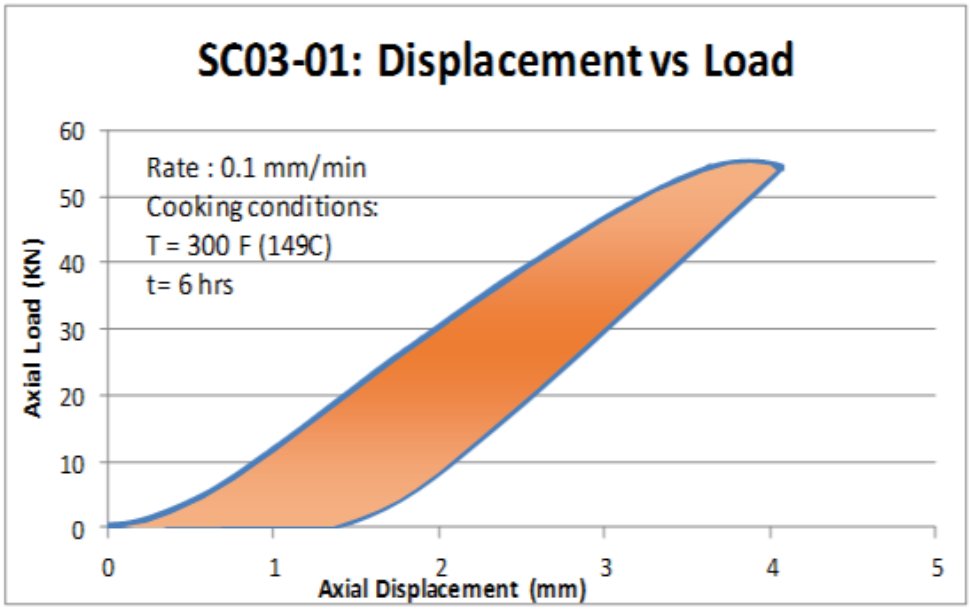


Figure 2: Typical loading and unloading curve in the displacement (mm) versus load (kN) curve. This is the data obtained from the MTS 810 frame and then it is used to calculated the energy and subsequently the fracture toughness. The orange area under the loading curve and over the unloading curve is the energy used to grow the fracture at the interface of this specimen.

As the actuator moves down, the load increases and the fracture initiates and propagates. At given load levels, a visual inspection is carried out and the fracture propagation is marked and a picture is taken as shown in Figure 3. The load levels at which the measurements were taken differ from the thin to the thick specimens because the thin specimens do not require as high load as the thick ones to reach the maximum fracture propagation. The test is considered complete and the maximum fracture propagation is achieved when the loading rate decreases in comparison to the displacement rate. After the test is deemed completed, the specimens are unloaded and retrieved from the loading frame. During the testing of scenarios SC01, SC02, and SC03, - thin specimens - the displacement and load inputs were recorded for the unloading phase. This was possible as the elastic rebound of these thin specimens is less than that of the thick specimens. On the other hand, the thick specimens were unloaded in a manually controlled step manner to ensure the integrity of the specimen after test completion.

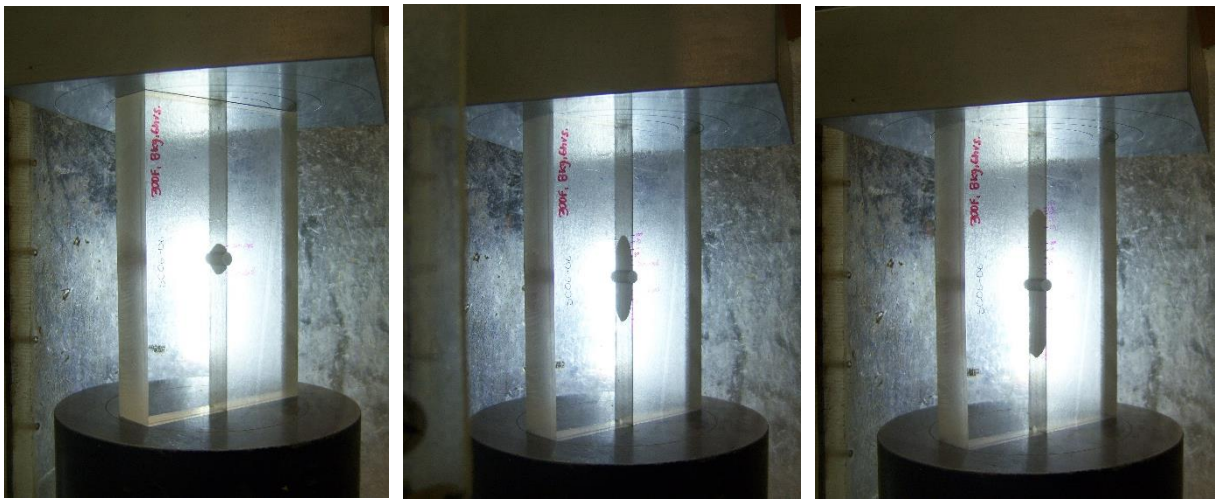

Figure 3: Specimen SC06-06 being tested in the MTS 322 at 0.1mm/min. Across the pictures the fracture growth is seen. Left, sample at 30kN compression, fracture present from specimen preparation damage mainly. Center, specimen under 100kN compression, fracture growth is symmetrical. Left, specimen under 150kN, asymmetry is shown on both arms of the fracture.

It is important to note that for the specimens in SC07, SC08, and, SC09, a polariscope was use to see the strains in the specimen through photo-elasticity, this will be further discussed later. The photoelasticity study yielded that at a lower load the strain field responsible for the fracture propagation is disturbed due to boundary effects, hence, the test of these scenarios was stopped once the load reached close to 120 kN to standardize the test completion to that value soon after the strain field is changed.

Once the specimens have been tested, the markings of the fracture propagation are measured starting at the fracture initiation point, ie. the vertex between the annealed surface and the center hole and extending towards both ends of the specimen. In the case of specimens presenting some damage, the recoded measurement of damage is subtracted from each of the fracture length measurements. These

measurements are recorded and the data collected from the loading frame for each specimen. Using this information, the fracture toughness of the interface and of the intact specimens are calculated using Griffith's principle

$$G = \frac{dU}{dA}$$

where $G$ is the fracture propagation driving force that can be calculated using the energy ($dU$) used to propagate the fracture and the area ($dA$) of the open fracture. The energy is calculated as the area between the loading and unloading curve as illustrated in Figure 2. This is achieved by using the trapezoidal rule for calculating the area under the loading curve for each specimen and subtracting the area under the unloading curve using the same rule for the thin specimens. For the thick specimens, the area under the unloading curve was estimated using an integration of the unloading curve function. The unloading curve of all the thin specimens are studied and an average is used to characterized this curve and apply it in the thick specimen case. The standard deviation of the curve is minimal as PMMA is a homogeneous material produced in laboratory conditions under the same procedure. The fracture area ($dA$) is assumed as a perfect rectangle and calculated by multiplying the fracture length by the thickness of the specimen in question. Once the driving force ($G$) is known, this value is used in fracture toughness equation for tensional mode 1 of in-plane stress (Moës et al., 1999)

$$G = \frac{K_I^2}{E}$$

where $K_I$ is the fracture toughness and $E$ is the elastic modulus, an intrinsic property of the PMMA. The fracture toughness can be calculated for any of the loading points recoded of fracture propagation, this richness of data is possible because of the controlled fracture propagation achieved using this proposed compressional test. Two approaches were used to analyze the fracture toughness of the specimen based on the point chosen to represent the fracture toughness: the ultimate load and the mid-point approach. Each specimen provides two fracture toughness for each approach, one for each arm of the fracture from the center hole.

As mentioned above, the photo-elasticity was only carried out in some of the scenarios studied and only a total of nine specimens, including three specimens of SC07, three specimens of SC08, and three of SC09. It was conducted during testing by taking a photo of the specimen at the corresponding load level and fracture extension marking. The polariscope was built on the MTS 322 frame by using two polaroid glasses and two ¼ lambda retardation plates. One polaroid and ¼ lambda lens was place between a light source and the specimen and another polaroid and ¼ lambda lens was placed between the specimen and the camera. The light source consisted of an LED warm white light lamp with a warm white thick paper

as diffuser. The polaroid glasses were measured to be at 90˚ orientation between them, with the first one, closest to the light source, being set at 0˚ and the second one, closest to the camera, being set at 90˚. The ¼ lambda plates were also set to be oriented at 90˚ between them, with the first one, closest to the light source, being set at 45˚ clockwise and the second one, closest to the camera, being set at 45˚ counter clockwise. This set up allowed for the visualization of the strain field within the specimen and the progression of the fracture growth. Figure 4 depicts a sequence of photos taken during testing of specimen SC09-06 from prior to loading to after fractured photos. In this series of photos, the isocromatic fringe can be seen increasing as the specimen is tested, starting with a low fringe number and easily seen isochromatic pattern to difficult to see the pattern and the fracture extending to the last fringe of the center load but stopping before interference with the fringes related to boundary conditions (Doyle & Phillips, 1989).

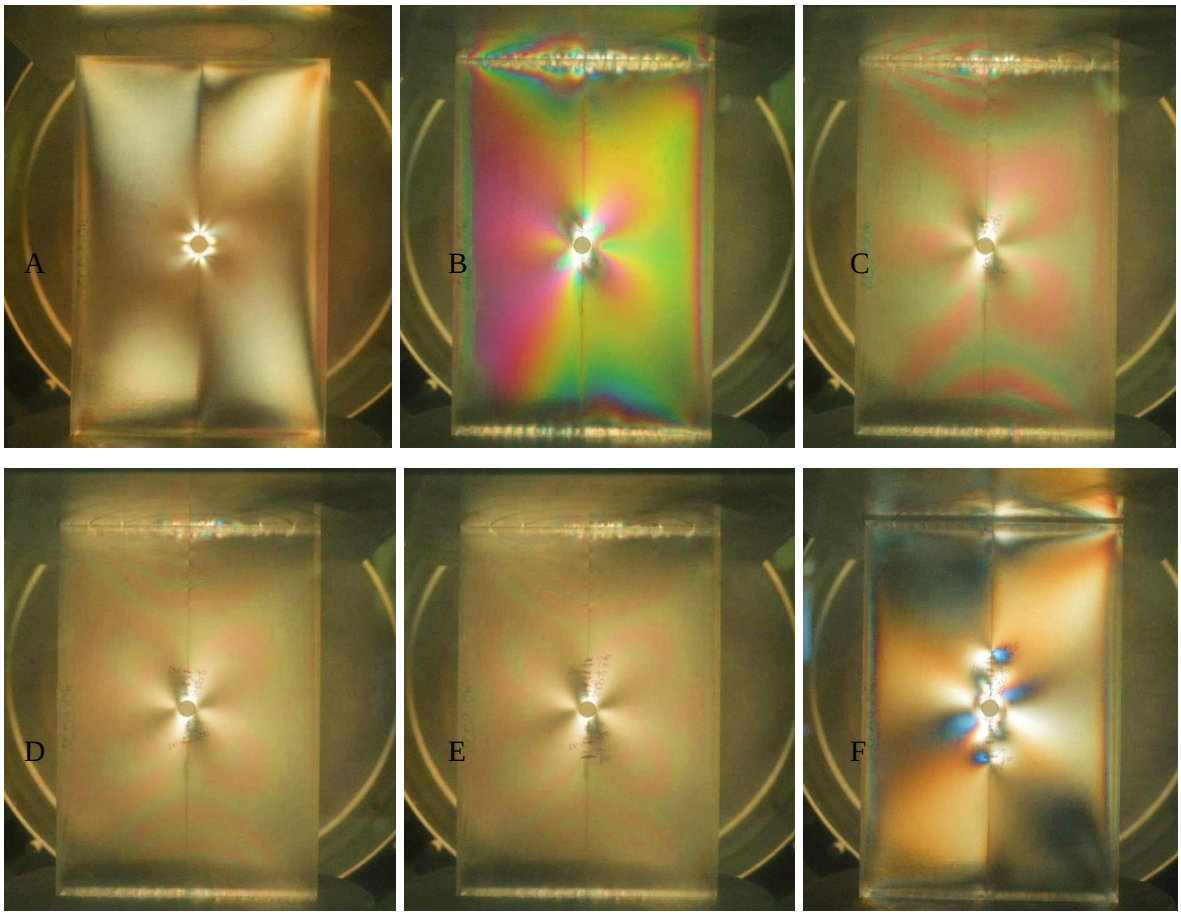


Figure 4: Enhanced visual results of photoelasticity study during testing of specimen SC09-06 where, photo A was taken prior to loading and depicts the residual stress of specimen preparation, mainly the drilling of the center hole. Photo B depicts the specimen just after commencing loading and it shows low isocromatic fringe order that subsequently increases in photos C, D, and E. Photo E was taken at the ultimate load and prior to unloading, in this photo the isochromatic fringes are difficult to see due to its high number and the fracture extends to the last fringe of the center strain but it stops prior to the interference with the fringes from the boundary condition.

## 2.3 Validation

The compact tension test, CT test for short, is a standard method for measuring fracture toughness for metallic materials under the opening tension mode I (ASTM INTERNATIONAL, 2001). The specimens studied using this standard test were performed as a calibration measure of the proposed uniaxial compression test. There was a total of six specimens tested using this procedure and they were prepared under the same conditions as those of SC09, hence they are referred to as SC09CT. These conditions are 8kg dead weights to provide 24kPa of healing stress, during 48 hours at 149 ºC or 300 ºF. The specimens were kept to the same external dimensions as those tested under the proposed procedure in this study, this means 152mm by 101mm. This geometric modification varying from the ASTM International (1997) standard was done to maintain consistency with the other scenarios but most importantly to extend the area of the tested interface. Nonetheless, the width to thickness ratio for these dimensions is 4 which is within the recommended ratio range according to ASTM International (2001). The length from the center line of the holes where the grips will pull to the end of the specimen is defined as $W$ and should be equivalent to 85mm due to the other geometries but it was measured to be 11.2cm, this value is used in the calculations of the fracture toughness. Per this $W$ value, the started notch was calculated and machined into each specimen. It is also important to note that the notched created was circular as specified by ASTM International (1997). The fatigue crack extension was developed from the damage from machining the notch and not from pretesting. The position of the holes for the grips were placed in accordance to the available grips and shown in Figure 5 left. Once the specimen preparation was finalized, the six specimens were tested using the MTS 322 frame in tension at the same strain rate as the uniaxial compression test of 0.1mm/min which fits within the ASTM specifications. Figure 5 right shows the specimen during testing.

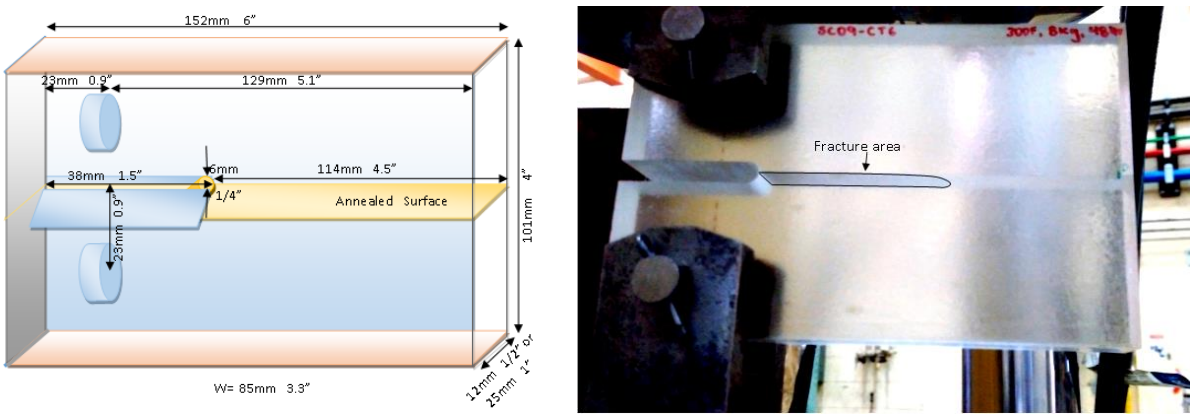


Figure 5: Left, schematic of modified CT testing specimen at the end of preparation. Right, SC09-CT6 specimen being tested. Fractured interface highlighted from the notch edge moving towards the annealed end.

Once the specimens were tested, the data collected and the length of the fracture ($a$) was measured and the displacement and loading data analyzed. A displacement versus load figure was created to establish the applied load ($P_Q$) that will be used to calculate the fracture toughness of the interface as shown in Figure 6. A secant line was applied to each plot and the applied load was established in accordance with ASTM International (1997). Based on this point and the measured data the fracture toughness ($K_Q$) was calculated by

$$K_Q = \left(\frac{P_Q}{BW^{1/2}}\right) \cdot f(A/W)$$

where $B$ is the specimen thickness of 25mm (1") and $W$ is the width of the specimen between the center line of the perforations and the end of specimen. This value is also used to determine all other dimensions of the specimen such as the height, in this case the $W$ was 112 mm (4.2") and $f(A/W)$ is given by

$$f(A/W) = \frac{-\frac{13.32a^2}{W^2} + \frac{14.72a^3}{W^3} - \frac{5.6a^4}{W^4}}{(1 - a/W)^{3/2}}$$

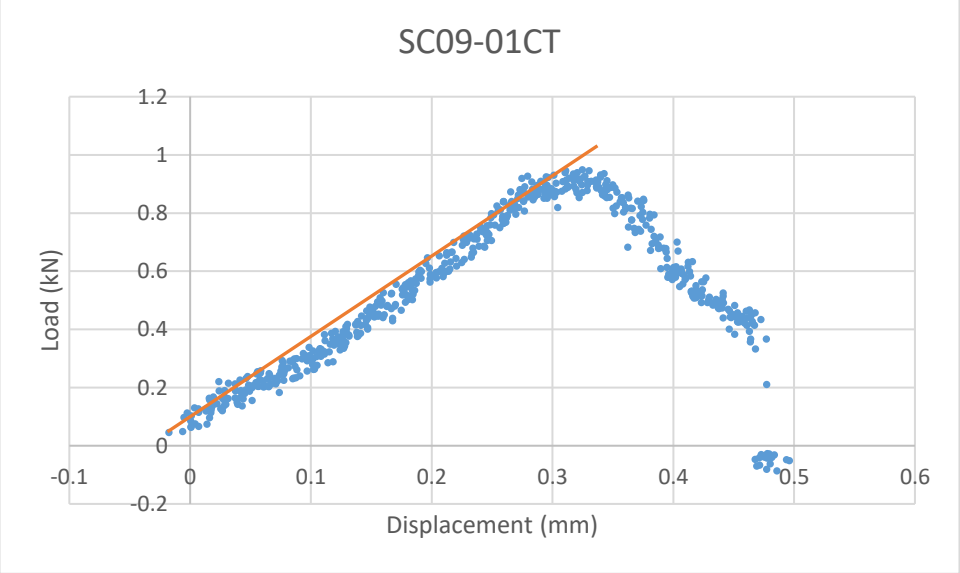


Figure 6: Typical Displacement versus Load plot that helps to establish the applied load used for calculating the interface's fracture toughness. The orange dot corresponds to that load while the orange line is the secant line to the data as instructed by ASTM International (1997)

Using this combined information, the fracture toughness of each specimen was calculated and the results are shown in Table 2, these results are compared at the end of the next section.

Table 2: Results of the six specimens tested under the standard CT testing and prepared according to ASTM International (1997). The specimens were annealed under the same conditions as those in scenario 9 with 48 hours and 24kPa at 149˚C

| | **Displ. (mm)** | **Load (kN)** | **Length (cm)** | **a/W** | **f(a/W)** | **Ki (MPa*m$^{1/2}$)** |
|---|---|---|---|---|---|---|
| SC09-01CT | 0.33 | 0.94 | 5.3 | 0.47 | 8.96 | 0.99 |
| SC09-02CT | 0.52 | 1.37 | 5.1 | 0.45 | 8.46 | 1.38 |
| SC09-03CT | 0.42 | 0.58 | 6.0 | 0.53 | 10.63 | 0.73 |
| SC09-04CT | 0.30 | 0.89 | 6.1 | 0.54 | 11.17 | 1.18 |
| SC09-05CT | 0.53 | 0.98 | 5.2 | 0.46 | 11.19 | 1.31 |
| SC09-06CT | 0.61 | 0.95 | 5.7 | 0.50 | 9.81 | 1.11 |
| **Average** | **0.45** | **0.95** | **5.5** | **0.49** | **10.0** | **1.12** |
| **std. dev.** | **0.12** | **0.25** | **0.42** | **0.038** | **1.15** | **0.234** |
| **cov** | **0.27** | **0.26** | **0.076** | **0.076** | **0.115** | **0.209** |

# 3 Results

Each specimen gives back two series of results; one series for each fracture arm which includes all the measured points. Two approaches were used to analyze the fracture toughness collected data, the ultimate load and the mid-point approach. The ultimate load approach consists on taking the last fracture toughness value at the maximum fracture length as the representative value for the arm of the fracture. Additionally, mid-point approach consists of taking the fracture toughness value to represent the overall fracture at the point where the fracture is 15mm long for the thin specimens and 20mm for the thick ones. Furthermore, it is important to note that this approach was not utilized with the data collected from the intact specimens because the intact specimens maximum fracture length was only 8mm for SC00-01 and 4mm for SC00-02, much less than the lengths studied through this approach. Both approaches give different fracture toughness values due to the change of the recoded values not being linear during the test procedure. Thus, each approach is more adequate for different scenarios. The mid-point approach is better for thin specimens as it truncates the data at a point prior to the influence of buckling. On the other hand, the ultimate point approach provides better, i.e. lower coefficient of variability, to the results of some thick specimens, namely scenarios SC04, SC05, and SC06. The ultimate point approach was improved during the testing of SC07, SC08, and SC09 by terminating the test at the maximum output load of 120kN creating a hybrid between the two approaches. This can be considered a combination between the mid-point approach and the ultimate point approach.

The intact specimens were fractured under uniaxial load in the same conditions as the annealed specimens. These intact specimens also shared the same external geometry as the annealed specimens and the center circular hole perforation. Similarly, the fracture in these specimens propagated from the same initiation point and followed the same vertical direction as the ones in the annealed specimens without a prescribed plane of weakness. The similarity in fracture geometry is the result from analogous stress fields in the annealed and intact specimens. The stress field runs vertically in the same direction as the uniaxial load; however, the center hole causes a disturbance in this field. Thus, the stress bypasses the center hole and it is concentrated around this hole. It creates a concentration and a singularity at the top and bottom of the center hole and this becomes the fracture tip and the fracture grows from there. In the intact specimen, the fracture toughness is much larger than that of annealed specimens, hence it takes more energy to develop a shorter fracture than in the annealed specimen. However, the specimen geometry and material properties of PMMA can only carry a finite load before yield. Thus, the fracture in the intact specimen is much smaller than the annealed specimen, and thus, the intact specimens can only be studied under the ultimate point approach as shown in Figure 7. For specimen SC00-01, the maximum fracture extension was 8mm at a maximum input load of 150 kN, corresponding to a fracture

toughness of 2.55 MPa*$m^{1/2}$. Consistently, the maximum fracture extension was 4mm at a maximum input load of 138kN with a fracture toughness of 3.07 MPa*$m^{1/2}$. The difference between these fracture toughness is based on carrying the first test to higher load inputs, this demonstrates again that the fracture toughness changes in a non-linear manner as the specimen is loaded. Hence, stressing the need for an establish maximum load to end the testing. Consistently, SC00-01 has a fracture toughness of 2.75 MPa*$m^{1/2}$ when the fracture's extension is 4 mm at 130 kN, comparable to that of SC00-02 at 138 kN. From the results from both specimens, the average fracture toughness for scenario 00 is 2.811 MPa*$m^{1/2}$ with an 11% coefficient of variability and a maximum fracture length of 5.8 mm at 144 kN. This fracture toughness is in average 100 times larger than the annealed specimens using the ultimate point approach.

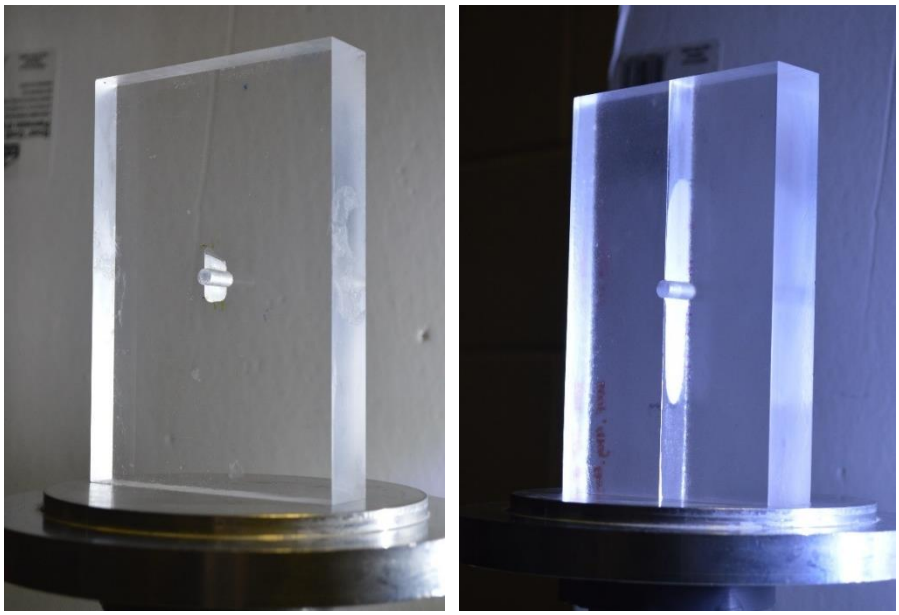

Figure 7: Intact and annealed specimen after fracture testing is completed. The maximum fracture length is visible for both, the intact and annealed specimen. The intact specimen presents a much smaller maximum length than the annealed due to the strong characteristics of PMMA while the annealed interface is much weaker.

## 3.1 Ultimate Point Approach

All the annealed specimens tested under uniaxial compression were studied under both the ultimate point test approach and the mid-point approach. First, the ultimate point approach will be discussed and compared to that of the intact specimens. The ultimate point approach consists of taking the last point in the data at the maximum input load as the representative value of the fracture toughness.

The study of SC01, SC02, and SC03, were thin specimens of thickness 12.7 mm (1/2″) and they were tested in the MTS 810 load frame. The fracture toughness, fracture extension and ultimate load values

were similar among these scenarios. SC01 had 7 specimens – 14 data points - and resulted in an average maximum fracture extension of 29.7 mm corresponding to 55.6 kN. This scenario has the lowest curing load of the three, at 6 kPa, and an average fracture toughness of 0.0145 MPa*$m^{1/2}$ with a coefficient of variability of 10%. SC02 had 6 specimens corresponding to 12 data points. This resulted in an average maximum fracture extension of 25.2 mm at 54.1 kN with a fracture toughness of 0.0160 MPa*$m^{1/2}$ and a coefficient of variability of 15%, this is 5% larger than that of scenario 1 and the highest one in the results of this approach. Similarly, SC03 – 12 data points – had a coefficient of variability of 14% for an average fracture toughness of 0.0139 MPa*$m^{1/2}$. This corresponds to 31.7 mm fracture length and 55.8 kN. This last scenario presents the highest curing load out of the three at 24 kN and thus, it was expected to have a slighter higher fracture toughness. However, the lower fracture toughness of this scenario in comparison to those of scenarios 1 and 2 can be explained by the longer length of the fracture. Additionally, extra specimens from scenario 2 were tested in MTS 322 resulting in values that validates the existence of no bias between tests performed on both machines.

SC04, SC05, and SC06, consist of 25.4 mm (1″) thick specimens that were tested in the MTS 322 unaxial load frame. Because of the thickness increase, the load input to drive the fracture was increased. The change in geometry, namely thickness, was completed to minimize the effect of buckling which was experienced during testing of the three first scenarios. The thermal healing conditions were kept the same as those in the first three scenarios, SC01 corresponds to SC04 at 6 kPa for their curing stress; SC02 corresponds to SC05 at 12 kPa; and, SC03 corresponds to SC06 at 24 kPa. All scenarios are composed of 6 specimens equivalent to 12 data points per scenario. SC04 presented an average maximum fracture extension of 29.3 mm corresponding to 143.7 kN. This scenario has an average fracture toughness of 0.0234 MPa*$m^{1/2}$ with a coefficient of variability of 11%. SC05 had an average fracture toughness of 0.0217 MPa*$m^{1/2}$ with a coefficient of variability of 15% and the average fracture length is 29.6 mm with an average maximum load is 136.0 kN. SC06 resulted in an average fracture toughness of 0.0212 MPa*$m^{1/2}$ with a coefficient of variability of 11%. The average fracture length was 29.3 mm and the average maximum load is 143.3 kN. The fracture toughness for all these tests are similar in value to each other, if slightly decreasing as the curing load increased. This slight variation could be due to some of the limitations encounter in this research which is further explained in the discussion part of this thesis found in chapter 4.

SC07, SC08, and SC09, consisted of 25.4 mm thick specimens and the testing was carried out in the MTS 322 uniaxial load frame, similarly to SC04, SC05, and SC06, but with a maximum input load of around 120kN. The preparation of the specimens consisted of subjecting the specimens at 24kPa, like the curing stress in SC03 and SC06 but varying the thermal bonding time. SC07 was subjected to 12 hours, double

that of SC06. The fracture toughness average for the 12 data points – 6 specimens - was 0.0214 MPa*m$^{1/2}$ with a coefficient of variability of 11%; this is a higher average than that of SC06. The average maximum length of the fracture is 19.8 mm and the average maximum load is 120.8 kN. SC08 was thermally bond for 24 hours, that is twice the time of SC07 and four times the time of SC06. The fracture toughness average was 0.0213 MPa*m$^{1/2}$ with a coefficient of variability of 12% for the 12 data points. These values are like those of the previous scenario. However, the maximum average load is 117.3 kN and the maximum fracture extension is 20.3 mm. For SC09, the specimens were thermally bonded for 48 hours. The average fracture toughness for the 12 data points is 0.0239 MPa*m$^{1/2}$ with a coefficient of variability of 13%; this coefficient of variability is the highest between the time variable scenarios. The maximum average load is 118.5 kN and the maximum fracture extension is 17.8 mm. The maximum fracture extension is low compared to the other scenarios. For a summary of all the different statistical data see Table 3

Table 3: Statistical results from the ultimate load approach for the intact and annealed specimens tested under uniaxial compression. For the specimen entry please refer to Appendix A.

| | Ki (MPa m½) | | | | |
|---|---|---|---|---|---|
| Scenario | Ave | StDv | Cov | Length (mm) | Load (kN) |
| 0 | 2.8111 | 0.3089 | 11% | 5.8 | 144.0 |
| 1 | 0.0145 | 0.0015 | 10% | 29.7 | 55.6 |
| 2 | 0.0160 | 0.0024 | 15% | 25.2 | 54.1 |
| 3 | 0.0139 | 0.0020 | 14% | 31.7 | 55.8 |
| 4 | 0.0234 | 0.0027 | 11% | 29.3 | 143.7 |
| 5 | 0.0217 | 0.0033 | 15% | 29.6 | 136.0 |
| 6 | 0.0212 | 0.0024 | 11% | 29.3 | 143.3 |
| 7 | 0.0214 | 0.0024 | 11% | 19.8 | 120.8 |
| 8 | 0.0213 | 0.0025 | 12% | 20.3 | 117.3 |
| 9 | 0.0239 | 0.0032 | 13% | 17.8 | 118.5 |

Using this ultimate load approach, SC01, SC02, and SC03 show a much smaller average fracture toughness than all the other scenarios tested in this study, especially when compared to the fracture toughness average of SC04, SC05, and SC06. This results from the difference in specimen thicknesses, being the first three scenarios half as thick as the latter three scenarios that were annealed under the same time and pressure conditions. Additionally, the discrepancy in these values can be the result of the ultimate approach analysis. These thin specimens presented buckling during high loads. The buckling

created secondary wing tensional fractures from the out-of-plane displacement. Hence, a mid-point approach was conducted.

## 3.2 Mid-Point Approach

This approach considers the half-point of the maximum extension of the fracture, this means 15 mm for the thin specimens and 20 mm for the thick specimens. The thick specimens were granted 5 mm longer for this approach as their thickness allows them to withstand a higher load prior to buckling.

By using the mid-point approach, the coefficient of variability of SC01, SC02, and SC03, for example the maximum reduction was by 7% from 15% to 8% for SC02. The values for these scenarios became higher when the data set was truncated to 15mm fracture length. For SC01 the average fracture toughness of 0.0191 MPa*$m^{1/2}$ with a coefficient of variability of 6%, and the average load that produced a 15mm fracture length is 52.0 kN. SC02 has an average fracture toughness of 0.0183 MPa*$m^{1/2}$ with a coefficient of variability of 8% and a corresponding load of 50.4 kN. This scenario has the largest improvement in this first three scenarios from 15% in the ultimate approach to 8%. SC03 presented the highest coefficient of variability among the thin specimens with 8%, an average fracture toughness of 0.0188 MPa*$m^{1/2}$, and a load of 51.8kN. The coefficient of variability of this scenario is significantly lower through this approach than the ultimate point approach decreasing from 14% to 8%

On the other hand, SC04, SC05, and SC06 resulted in much higher variability of fracture toughness values, thus, increasing the coefficient of variability by a substantial amount. The largest change was for SC04 with an increase of 17% for the coefficient of variability from 11% to 28%. These scenarios were evaluated at 20 mm fracture length as the specimens are 25 mm thick. The average fracture toughness for SC04 was 0.0216 MPa*$m^{1/2}$ with a coefficient of variability of 28% and a corresponding load of 121.5 kN. For SC05 the average fracture toughness was 0.0201 MPa*$m^{1/2}$ with a coefficient of variability of 29% and a corresponding load of 113.3 kN. Similarly, SC06 showed an average fracture toughness of 0.0191 MPa*$m^{1/2}$ with a coefficient of variability of 25%. The average load to create a 20mm fracture is 109.4 kN. This approach result in a large under estimation of the fracture toughness for SC04, SC05, and SC06.

SC07, SC08, and SC09 of this study were constructed using longer thermal bonding times and thick 25 mm specimens. For this approach the fracture length was considered 20 mm long, same as in SC04, SC05, and SC06. This mid-point approach yielded less variant results than the ultimate load approach as opposed to the trend set for SC04, SC05, and SC06. For SC07 the average fracture toughness was 0.0207 MPa*$m^{1/2}$ with a coefficient of variability of 8%. The average load to create a 20mm fracture is 126.0 kN. SC08 also had 9% coefficient of variability as scenario 7 but an average fracture toughness of 0.0201 MPa*$m^{1/2}$. The average load to create a 20mm fracture is 116.5 kN. This similar results to the first

scenario can be an underestimation due to the lower load input. Lastly, SC09 resulted in an average fracture toughness of 0.0217 MPa*$m^{1/2}$ with a coefficient of variability of 9% and an average load of 134.3 kN. The results of all specimens are summarized in Table 4.

Table 4: Statistical results from the mid-point approach for all annealed specimens tested under uniaxial compression. Note that scenario 0, intact specimens, were not included in this approach as their maximum fracture growth is half that of the thin specimen extension. For the specimen entry please refer to Appendix A.

| | Ki (MPa m½) | | | | |
|---|---|---|---|---|---|
| Scenario | Ave | StDv | Cov | Length (mm) | Load (kN) |
| 1 | 0.0191 | 0.0012 | 6% | 15 | 52.0 |
| 2 | 0.0183 | 0.0014 | 8% | | 50.4 |
| 3 | 0.0188 | 0.0016 | 8% | | 51.8 |
| 4 | 0.0216 | 0.0061 | 28% | 20 | 121.5 |
| 5 | 0.0201 | 0.0059 | 29% | | 113.3 |
| 6 | 0.0191 | 0.0048 | 25% | | 109.4 |
| 7 | 0.0207 | 0.0018 | 8% | | 126.0 |
| 8 | 0.0201 | 0.0019 | 9% | | 116.5 |
| 9 | 0.0217 | 0.0019 | 9% | | 134.3 |

The difference between both approaches can be reflected in Figure 8 for all the annealed specimens' scenarios. The ultimate point approach yields less variant results for SC04, SC05, and SC06. However, this approach yields under estimations of the fracture toughness for SC01, SC02, and SC03 of this study involving thin specimens. In SC07, SC08, and SC09 the ultimate load approach and mid-point approach provides similar values of the coefficient of variation. The mid-point approach produces smaller average values and a smaller coefficient of variability value for the SC07, SC08, and SC09. Similarly, the mid-point approach yields more coherent results and over estimations of the fracture toughness to s SC01, SC02, and SC03, when compared to the ultimate point approach. These values are more in line with those of SC04, SC05, and SC06, which were produce under the same thermal healing conditions as the first three scenarios. It is important to note the large difference between the fracture toughness value of the two approaches for SC06. The ultimate point approach provides similar values to those of the scenarios with an acceptable coefficient of variability, while the mid-point approach gives a low estimate of the fracture toughness and a very large coefficient of variability of 31%.

The results show that the last SC07, SC08, and SC09 resulted more coherent results. This is demonstrated on the similarity in coefficient of variability using the ultimate point approach and the mid-point approach. This can be the result as the implementation of a maximum load input during testing. There

are other points that were recognized and can be used to further improve this test which will be discussed in the next chapter of this thesis.

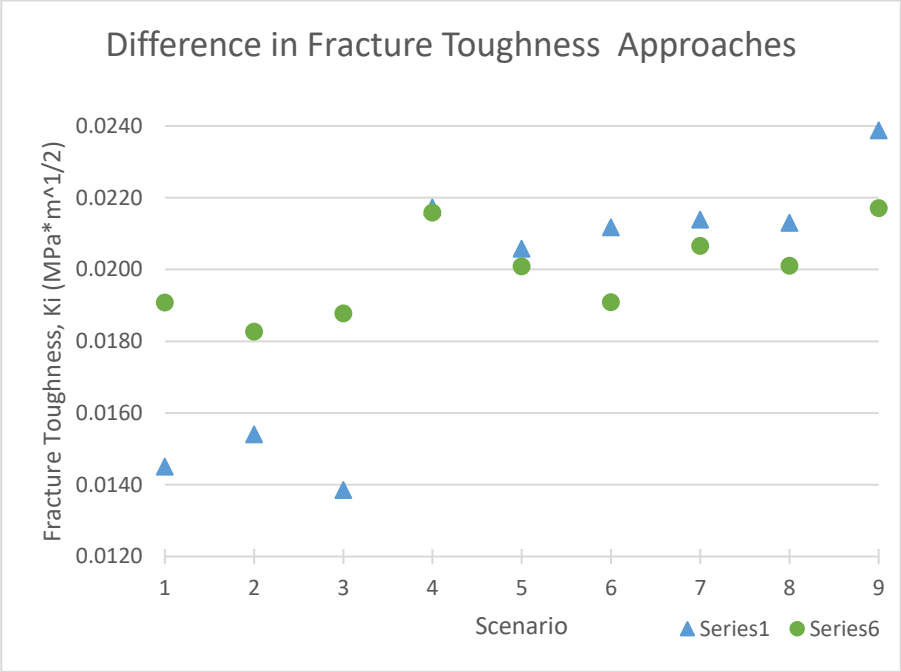


Figure 8: Comparison of statistical results among the two different approaches.

## 3.3 Validation

During the validation phase of this study, six (6) annealed specimens were tested using the standard CT test. These specimens were annealed under the same conditions as those of SC09, being thermally heated for 48 hours at 149˚C under 24kPa of stress. The average fracture toughness yielded by this testing is 1.1209 MPa*$m^{1/2}$ with a standard deviation of 0.2344 MPa*$m^{1/2}$ and a coefficient of variability of 21% and the average load of 0.95 kN and fracture length of 55.6cm. On the other hand, scenario 9 in the midpoint approach resulted in an average fracture toughness of 0.0217 MPa*$m^{1/2}$ with a standard deviation of 0.0019MPa*$m^{1/2}$ and a corresponding coefficient of variability of 9% and the average load of 134.3 kN for a 20mm fracture corresponding to each fracture arm. Results from SC09 using the ultimate load approach presented an average fracture toughness is 0.0239 MPa*$m^{1/2}$ for the 12 data points – 6 specimens with two fracture arms each - with a standard deviation of 0.0032 MPa*$m^{1/2}$ and coefficient of variability of 13%; this coefficient of variability is the highest between the time variable scenarios. The maximum average load is 118.5 kN and the maximum fracture extension is 17.8 mm.

The fracture toughness obtained from the CT testing is approximately 50 times higher value than that of the same scenario tested in the proposed compressive test. All fracture toughness results from SC09-CT are lower than the intact specimen material which has a fracture toughness of 2.811 MPa*$m^{1/2}$, making them valid. Furthermore, these high values could be taken as the true fracture toughness of the specimen due to them representing 40% of the intact fracture toughness as opposed to only 1%. However, Jud et al. (1981) studied PMMA specimens under CT testing and found that their intact fracture toughness for mode I is 1.1 MPa*$m^{1/2}$ meaning that the CT results show an almost intact fracture toughness for the SC09-CT specimens. A contributing factor of this result is given to the determination of the specimen width which the geometry of the specimen depends upon from 8.5 cm as it was used in the design phase of the other parameters of the specimen geometry to 11.2 cm as it was measured and tested. Additionally, the CT specimen results in a single fracture providing less statistical points as opposed to the proposed compressive test which provides two fracture per specimen, the upper and the lower arm. The coefficient of variability within the CT test is higher than that of the compression test SC09 by at least 8% when compared to the ultimate load approach and 12% when compared in the mid-point approach. The difference in fracture toughness among the scenarios studied under the proposed test is small but the differences between fracture toughness resulted from CT testing is indeterminate since only one scenario was tested. Major difficulties were also encountered when performing the CT test, such as the measurement of the fracture length. In many cases the fracture length was taken after a sudden energy released was heard, which indicated a rapid extension of the fracture. Only once was the fracture propagated in an stable manner but measurement could not be taken due to its high propagation velocity. The total amount of CT testing time did not surpass 15 minutes which is very short when compared to the uniaxial compression that took 45 minutes of loading for the thin specimens and up to 90 minutes for the thick specimens. Hence, although the CT would provide a good fracture toughness result, it is important to test other scenarios and see how the fracture toughness compares and to establish if there is a relationship between both tests.

The CT tests experienced some complications such as the difficulty of an unobstructed visual field to see the fracture propagation. The visual field presented two obstacles, first, the interference of the frame between the angled light and the specimen; and second, a much faster fracture propagation rate than that of proposed compression test. Another complication was the geometry of the specimen following ASTM standards. This only allowed for a short annealed interface area creating a high ratio of boundary interference to the total annealed area. Therefore, a small deviation was taken from the prescribed geometry to elongate the annealed interface. Additionally, fatigue testing to initiate the fracture was not carried out due to the high risk of failure from the specimen preparation.

# 4 Discussion

The great advantage of the proposed testing procedure – uniaxial compression load - is the ability to see the propagating fracture at slow strain and to achieve a controlled development. Some of the limitations that were encountered in SC01, SC02, and SC03 were addressed during the refinement of this testing while there are other limitations that can still be improved. The most prominent issue of these scenarios was buckling on the specimen that resulted in secondary tensional fracture opening from the out-of-plane displacement.

To address the buckling issue that arose from this test a couple of changes were implement after the testing of SC01, SC02, and SC03. For example, all scenarios thereafter were completed using thicker specimens to help reduced the critical load at which buckling starts. Another implementation was done during testing SC04, SC05, and SC06, such as, the maximum load during testing did not exceed 125 kN but was kept at about 120 kN. This resulted in similar coefficient of variability across the three different scenarios tested under this condition. However, a better way to predict the maximum load and the end of the test would be using Euler's critical load, this value is based on the geometry of the specimen tested. This is the maximum value at which the specimen is not subjected to buckling. This critical value ($P^{cr}$) is calculated using

$$P^{cr} = \frac{\pi^2 \, E \, I}{L_e^2}$$

where $L_e$ is the effective length of the specimen. This length depends on the end condition of the specimen being tested in this case fixed-fixed. $L_e$in this case is $\frac{L}{2}$ where $L$ is the length of the specimen. $E$ is the bulk modulus of the material, in this case PMMA 2.5 GPa. $I$ is the moment of inertia based on the geometry of the specimen and given by

$$I = \frac{b \, h^3}{12}$$

where $b$ is the base which is 50 mm (2″) for each piece being tested and $h$ is the height of the cross-sectional area of the column. Two cases were studied, the thin specimen with thickness 12 mm (½″) and the thick specimen of 25 mm (1″) thickness. This yielded two inertias and two critical pressures. Thus, this resulted in two different Euler's critical values of 36.8kN for the thin specimens and 294.8kN for the thick specimens. The sample calculations can be seen at the end of Appendix A.

During testing, the thin specimens were subjected to an average of 55kN which far surpasses the Euler's critical value. On the other hand, the thick specimens had a maximum average load of approximately 150

kN which is lower than the critical value. Hence, the thick specimens did not suffer from buckling as the thin specimens did.

Some recognized errors were due from the estimation of the fracture geometry as opposed to the actual fracture geometry. Some specimens showed existence of fractures prior to commencing the test that extended up to 2mm from the initiation point at the vertex between the annealed surface and the center hole. This results from the drilling of the whole on the otherwise well annealed surface. This error was corrected for in the calculation phase of the study where the measured damage was subtracted from the length of the fracture. Additionally, errors were included from the assumed shape of the fracture and this was not accounted for. For simplicity, the fracture was idealized as a rectangular shape that extends from the hole along the annealed fracture. However, this simplistic shape is not the case. The fracture shape is half a circle at the beginning that grows in diameter as the fracture extends away from the center hole; this circle changes to an ellipse when its diameter reaches the thickness of the sample. The opening front becomes an arch and the crack tip is the highest point of the arch. The area behind the opening front of the fracture is rectangular with the base being the thickness of the specimen. The arch keeps sharpening and the distance increases between the ends of the arch at the full thickness and the crack tip, this is known as tunnelling. The exact fracture shape and measurements varies from each specimen. Accurate measurements of the fracture tip were difficult to obtained during fracture propagation because the measurement were taken manually from visual inspection and the from a distance for safety reasons. A better way to acquire the measurement would be to get the measurements from an stationary visual point as the camera with a measuring grid for calibration.

Another limitation of this study is the thermal bonding restriction, such as maximum temperature before complete melting, maximum applied pressure, and minimum healing time. The temperature is the variable that has the least range due to PMMA melting point being close to the applied temperature, hence this variable was not included in the study. The stress during thermal bonding is applied by dead weights. To increase the applied stress significantly during the thermal bonding a different way to create the pressure is needed. This new way would have to fit within the dimensions of the oven creating the need for a pressure chamber. The last variable is the time flexibility which is the easiest variable to adjust as the cooking time can be elongated to the desired length.

## 4.1 NDT Testing of Annealed Specimens

This section summarizes the work completed in collaboration with Sabah Fartosy, Dr. Giovanni Cascante, Dr. Maurice Dusseault, and, Dr. Dipanja Basu, the statement of contribution along with a copy of the

verbatim material to be submitted to the Journal of Geoenvironmental Engineering can be seen in Appendix C.

A series of Non-Destructive Testing (NDT) were carried out in 17 annealed specimens at three different stages. The stages at which the specimens were tested are: (1) after the annealed surface was achieved or intact condition; (2) during the specimen preparation after the short ends were milled and the center hole was emplaced; and (3) after the controlled fracture was completed. Four additional specimens were tested during the stable fracture propagation test. These are two solid specimens and two of the time variables annealed specimens.

The NDT testing was carried out using the Ultrasonic Pulse Velocity (UPV) direct transmission method measuring the wave velocity and attenuation. Two piezoelectric transducers were coupled using grease to the sides of the specimens normal to the interface. A square wave was send from the transmitter across the specimen to the receiver. This method was intended to recognize the existence of a thin crack along the interface. This was achieved through the analysis of the data where the signal attenuation dramatically decreased., up to 60%, in the tests carried out after the fracture was present. On the other hand, the wave velocity did not present a drastic decrease but only a slight one with a maximum reduction of only 4%.

From the four specimens subjected to the UPV test during fracture propagation further analysis were performed. For example, the calculation of the PMMA material Young's modulus is carried out in this article for the two solid specimens and in different areas of the curve. This yielded a static Young's modulus ranging 0.93 GPa to 1.87GPa. While the dynamic Young's modulus was calculated to be 4.66GPa. Additionally, the spectrum of the wave is compared to the fracture growth for all four specimens. The wave attenuation is well illustrated as the fracture growths at the end of Appendix C.

# 5 Application of Bonding Methodology for Hydraulic Fracturing

A major research interest is to better understand the interaction between the newly developed fracture and the pre-existing planes of weakness. The hydraulic fracture experiment intends to demonstrate that the new hydraulic fracture does not only increase the permeability of the volume directly affected by the injection and adjacent to the well, but creates a much larger stimulated volume from the reopening of the natural fractures through shear displacements and wedging effects. Therefore, these pre-existing planes of weakness are study throughout this research and a synthetic analogue fractured media is created. This analogue is characterized using fracture mechanics and used as fracture media for studying its interaction with the new hydraulic fracture. In this appendix, a proposed experimental methodology is described that allow us to study the hydraulic fracturing process to be studied in real time in a transparent rock analogue containing weak planes, polymethylmethacrylate (PMMA). This includes the design of the compression frame where experiments would be run; the design of the injection systems involve for the recreation of the hydraulic fracture, such as, the equipment used and fracturing fluid; the procedure for collection of results and the experiment set up and experimental procedure.

The proposed experimental set up consists of a uniaxial frame with a transparent upper compressive layer that allows to monitor the specimen as it is fracturing. A similar set up has been presented in the works of Andrew Bunger (Bunger, 2006; Jeffrey & Bunger, 2007). Some authors have recently started to performed small scale hydraulic fracturing experiments under varying conditions. However, most of the work has been focused on stress zones and other parameter such as the different viscosities of fracturing fluid (Bunger, et al., 2005; Ishida, et al., 2004; Zoback et al., 1977), and less attention has been given to the fracture network (Blanton, 1982; Jeffrey et al., 2009; Mitra & Ghosh, 2009) but none of these address the interaction between the hydraulic fracture and a cohesive fracture media.

## 5.1 Background

### 5.1.1 Conceptual Explanation of Hydraulic Fracturing

Hydraulic fracturing is the technique which induces fractures within the earth's crust at desired locations. The process starts by drilling a borehole down to the desired formation to be stimulated. At this point, measurements of the in situ earth's stresses are taken, such as the maximum and minimum stresses and their orientations. In situ stresses are the result of the weight of the overburden material and the tectonic and geological history of said location (Nolen-hoeksema, 2013). Depending upon the method that is to

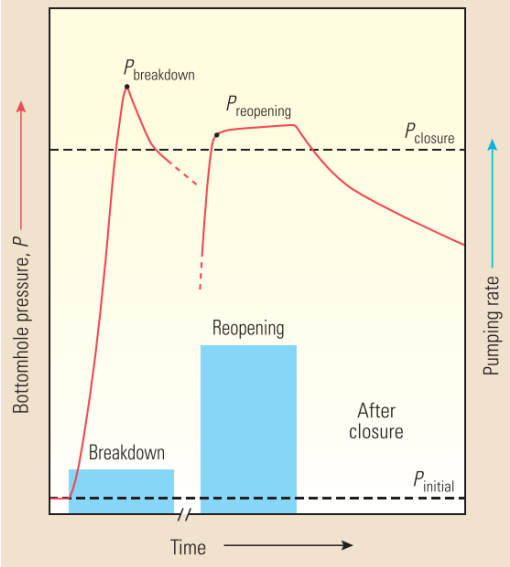


Figure 9: Typical hydraulic fracturing pressure curve showing the breakdown pressure, the reopening pressure and the closure pressure (Nolen-hoeksema, 2013)

be used to create the fracture, the well will be cased, cemented and perforated for a perforations job or simply cased for ball and drop. Then, fracturing fluid is injected into the rock mass and pressure builds up within the well until the break down pressure ($P_{BD}$) is achieved. The break down pressure is measure by a series of gauges. The subsequent pressure changes are recorded and plotted into a typical pressure curve from a hydraulic fracturing job is illustrated in Figure 9. Hydraulic fracturing occurs when the fracturing fluid reaches a pressure that is equal to the minimum in situ stress and the new fracture develops orthogonal to the maximum in situ stress (Hubbert & Willis, 1972).

The sudden decrease in measured pressure indicates the establishment of the new fracture. For the reopening case, the pressure does not build up to that of the break down pressure as the true cohesion of the rock mass is lost. Fracturing fluid is constantly injected to allow the new fracture to grow which manifests as a flattening of the curve in Figure 9 after the reopening pressure in the graph. After a desired volume is injected, the pump is turned off and the pressure is allowed to dissipate stopping further fracture growth as shown in the inflection point and subsequent pressure decrease The new fracture remains open thanks to the injection of a proppant mixed in the fracturing fluid, shear displacements between the walls of the fracture, or a combination of both (Nolen-hoeksema, 2013). It is common for the same well to be treated several times along its length from the toe to the heel in the case of multiple stage hydraulic fracturing.

The fracturing fluid has evolved since the first hydraulic fracturing injections. The first fractures were developed using naphthenic-acid-and-palm-oil thickened gasoline. Gelled kerosene replaced the thickened gasoline, which was later replaced by some combination of refined and crude oils. This mixture of fluids was preferred to the previous injection fluids because of their lower viscosity by comparison (Montgomery et al., 2010). At this point, sand was used as a proppant to keep the walls of the new fracture open. Thus, the fluid viscosity was increased resulting in higher injection rates in order to push the proppant along the fracture length (Nolen-hoeksema, 2013). In 1953, the first water-based treatment was conducted with the help of various additives such as gels and other chemicals. These additives made water-based fracturing fluid suitable in different types of formations. Over the years, different gelling agents and stabilizers have been produced to reduce shearing of the casing and to achieve the desired

viscosity using less additives (Montgomery et al., 2010). Similarly, different types of proppants are produced and used per the properties of the rock mass being treated. High concentrations of sand are commonly used now as proppant to maximize the volume that remains open in the new fracture after completing the treatment.

### 5.1.2 Literature review of Experimental Hydraulic Fracturing

For many years, laboratory experimental work of hydraulic fracturing was not widely researched. Most of the published studies are contemporaneous to the development of this technology; however, experimental work has resurfaced again in recent years. These new experiments use a combination of unconsolidated sediments, rock samples and rock analogues to study the desired variable.

One of the first laboratory scale experimental studies carried out is Blanton (1982) who used rectangular prisms of shale rock samples and hydrostone (artificially created stone) specimens. All specimens were rectangular prisms with a square base of 11.5" (0.29m) for the shales and 12" (0.30) for the hydrostones. They were subjected to true triaxial compression and hydraulically fractured in specially constructed chamber. Some of the hydrostones had systematically variant cohesive pre-existing fracture created during specimen preparation. The specimens were fractured and the hydraulic pressures were recorded and later compared to the fractured specimens. The interactions between the new fracture and the pre-existing fracture were observed as well as the role of different levels of stress. Due to the nature of the specimen material and the steel chamber, the fracture growth is not visible during the experiment.

Papadopoulos, et al. (1983) addressed this issue by constructing two compressional frames, one for testing cement paste specimens and another for testing PMMA specimens. One of these frames was a uniaxial reaction apparatus with a transparent top layer composed of PMMA in which cylindrical specimens would be tested. This frame design and a modernized version of it proposed by Bunger (2006) are the inspiration for the apparatus design in this study. Both studies tested specimens composed of PMMA. Papadopoulos et al. (1983) tested specimens with a cohesionless discontinuity composed of "two polished and well-mated surface", which allows the fracture path to be seen. High viscosity fracturing fluid was used during the tests but the injection rate was not specified. On the other hand, Bunger (2006) used a solid rectangular prism confined to present a physical barrier with flat jacks but these were not operated. On another article by Jeffrey and Bunger (2007) using the same frame and PMMA specimens tested the specimens under different lateral stresses for two adjacent PMMA blocks creating a stress jump. The interface between these two blocks serves as initiation point for the hydraulic fracture. The fracturing fluid used for this experiment was an aqueous solution of glycerine or glucose and food dye.

A positive displacement step motor pump was used to inject the fluid in the specimen and the flow was regulated by a needle valve.

Zeng and Roegiers (2002) conducted a hydraulic fracturing laboratory experiment to study the relationship between injection rate and pressure. They tested three specimens of Jackford sandstone using three different flow rates of 1.00 $cm^3$/min, 0.10 $cm^3$/min and 0.01 $cm^3$/min. This was achieved by using a syringe pump controlled by a computer program. The different injection pressures resulted in three different breakdown pressures ranging from 19.8MPa for the highest flow rate to 22.9MPa for the lowest rate, and 22.0MPa corresponds to the injection rate of 0.10 $cm^3$/min. Information about the fracturing fluid composition and properties were not provided. Similarly, Rubin (1983) studied a laboratory scale hydraulic fracture in PMMA using a high viscosity fluid of 200 Silicone with a viscosity of 97,700 centipoise (cp), similar to the fracturing fluid use in this experiment. A pre-fracturing phase was completed using a hand pump to reduce the fluid compressibility effect while a motor pump was used during the main fracture stage at an injection rate of 73.2$mm^3$/s.

The interaction between hydraulic fracturing and pre-existing fractures is an important phenomenon that controls the result of a fracturing job. Some experimental tests have been conducted to increase our understanding of this matter. Most experiments have been performed in opaque media such as Zoback et al. (1977), Blanton (1982), or more recently Cheng et al.(2014), while only a very few have studied this phenomenon in transparent material. Xing et al. (2016) presented an experimental study in transparent polyurethane with two horizontal and one vertical cohessionless interface using a total of six blocks of material. Additionally, the center layer, proxy for the reservoir, has a lower Young's modulus than that of the bounding upper and lower layers. This setting is achieved by pushing together the blocks under vertical stress and different horizontal stresses within the same specimen. The resultant fracture geometry under the different parameters were studied in the present study cohesive blocks of PMMA are used in a cross-bedding manner as a specimen to test for the interaction between weakly bonded fractures and the new hydraulic fracture.

## 5.2 Experimental Preparation

Laboratory scale physical emulation of hydraulic fracturing needs a comprehensive setting for the experiment to achieve the desire outcome. The objective is to produce a reliable methodology and see the hydraulic fracturing path growing in real time under some stress. Therefore, it is required to have a compressional frame that allows visual access to the samples at least from two planes for a 3D study. A hydraulic system that provides the necessary force to stress the sample to the chosen compressional level

was chosen, calibrated and put together. A fluid injection system was also put together that provides the necessary pressures for the sample to break and the hydraulic fracture to initiate and growth within the specimen interacting with the artificial planes of weakness.

### 5.2.1 Apparatus Design

The compressional frame was designed with the consideration of having sample sizes ranging between 150×150×150 mm (6" per side) to 500×500×500 mm (20" per side) under uniaxial compression, and zero horizontal stresses creating a deviatoric stress. The compressional frame can be subdivided into two parts, the apparatus and the hydraulic system that provides the compressional forces. Additionally, it was projected that with further design and a fixed sample size, the frame could be adapted to biaxial—and possibly true triaxial—loading while still having access to two planes.

The uniaxial compression frame apparatus is made of a combination of steel parts and plates and two polymethylacrylite (PMMA) plates, a transparent material. Steel was chosen as the preferable material for its high strength, while PMMA was a more suitable choice for its flexibility when compared to borosilicate glass. The frame is a reaction frame where the top plate and bottom plate are kept in place and while the hydraulic system pushes apart within this ensemble; more specifically onto the bottom reaction plate and the distribution plate. The distribution plate transfers this force to the sample and the top plate.

The frame is composed of a steel plate of dimensions 609×609×25 mm (24"×24 "×1 ") that holds the frame together with four M20 rods of 1m (39.4 ") in length and a top plate as shown in Figure 10. The rods are located at each corner of the plate and held in place with 4 sets screws from the sides. These rods connect with the corners of the top PMMA plate of dimensions 609×609×102 mm (24"×24"×4"). This top plate is the critical component of the assemble, thus a steel frame around it was added for its protection and increasing its rigidity. This protective frame is made from 76×101 mm (3"×4") steel angle of 12mm (1/2") thick and rubber is used to prevent any point load between the top plate and its protective frame. The top plate also has a 12.7mm (1/2") hole at the center that acts as borehole for the fluid system pipe.

Within the reaction frame, the hydraulic system is placed to provide the axial force to pressurize the sample. This is composed of a flat jack with an area of 0.168$m^2$ (260 sq. in.) and its manual pump for a maximum stress output of 13.79MPa (2,000psi) along with a calibrated load cell of maximum 25,000 lbf and a load frame connection. On top of this connection a steel load distribution plate is placed of dimensions 558×558×25 mm (22"×22"×1") chamfered at the corners to fit among the four steel rods.

There are 14 machined grooves every 25.4mm (1") on this plate that house flexible RGB LED strip lights. Another PMMA plate of dimensions 558×558×50 mm (22"×22"×2") is placed on top of the distribution plate to protect the lights and allow for a uniform light background. This PMMA plate is also chamfered at the corners to fit among the four steel rods that hold the assemble. The steel distribution plate, bottom PMMA plate, and the lights are free to move in the vertical direction as provided by the flat jack input force to compress the sample against the top PMMA plate.

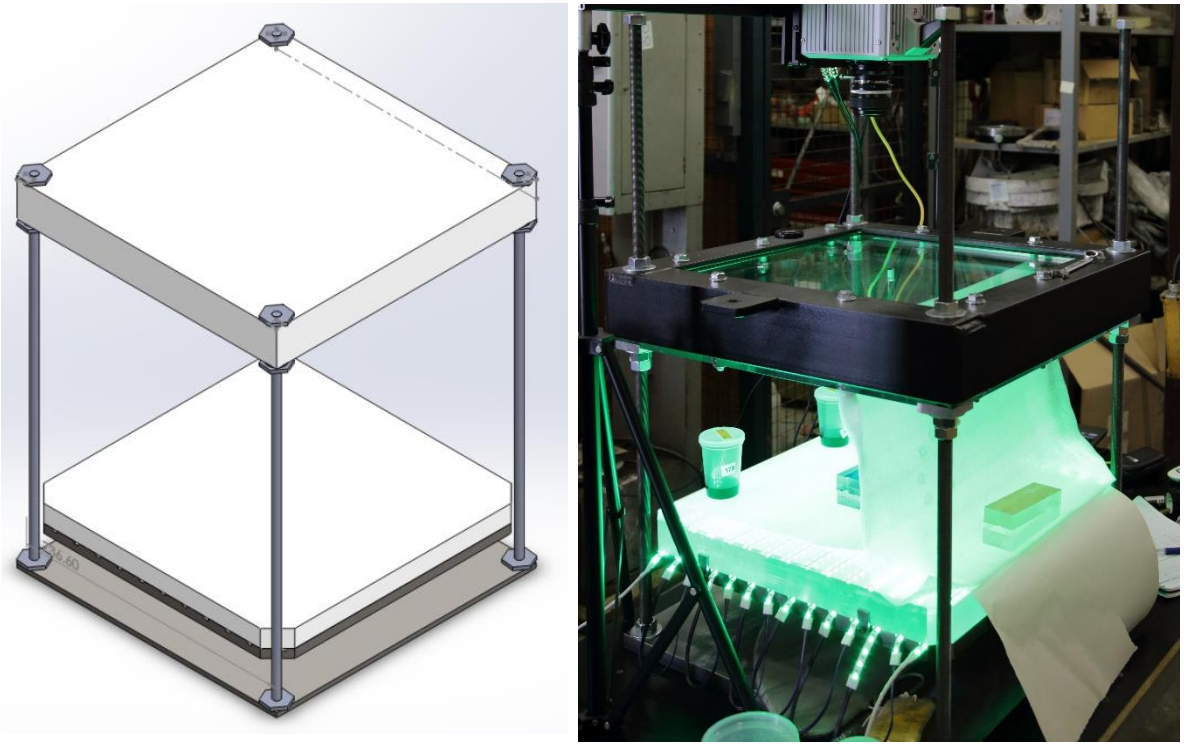

Figure 10: Uniaxial frame schematic after design is completed on the left and the constructed during calibration.

The lights along with the controller and power generator assembled to provide very bright light beams to record the interaction between the injection fluid and the specimen. The visual recording will be taken by two high-speed cameras, one overhead and a supplementary one on the side and two DSLRs at the same positions. The high-speed cameras have a maximum recording time of one second but they have higher frame rates allowing for some details to be seen such as the fluid lag at the fracturing front, while the DSLR will film the complete experiment.

#### 5.2.1.1 Top Layer Criteria

The top PMMA plate will be subjected to high loads of stress that are transferred from the specimen made from the same material. Hence, special attention was given to this plate as it is the weakest point on the frame. Although the bottom PMMA plate is thinner than the top plate, the bottom plate is reinforced in its totality with the steel load distribution plate. Hence, the loading limitations of the top plate were carefully studied.

The top layer of the assemble was studied as a 2D beam fixed at both ends as it would provide a conservative estimate for the maximum input load allowed. The fixed ends condition is developed from the steel frame surrounding the top plate and providing it rigidity as illustrated in Figure 11. The dimensions of the plate was 609mm for its length and width and 101mm for its thickness.

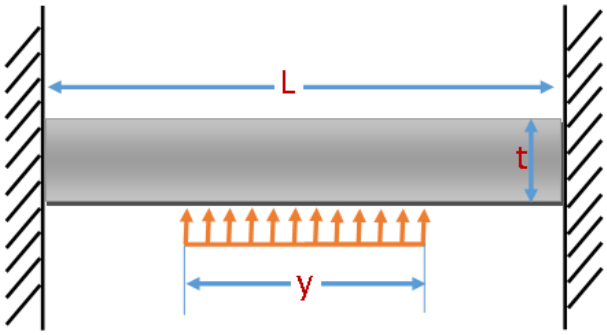


Figure 11: Schematic diagram of top layer plate fixed on both ends that was used to calculate the maximum input load for the frame, where the applied pressure comes from the bottom of the plate from the compressed specimen

The top plate was studied under two loading conditions corresponding to the maximum and minimum measurements of the sample size range. These were 150mm and 500mm. The larger sample resulted in higher stresses so this was used as ultimate load parameter. With the given loading length, the maximum load was calculated to be 592kN or 1184.22 kPa.

### 5.2.2 Fluid Injection System

#### 5.2.2.1 Fracturing Fluid

The fracturing fluid is composed of 99.5% pure vegetable glycerine and blue wilton dye in gel form. The dye is difficult to mix due to its high viscosity so it was diluted with glycerine at 1:1 ratio. From this dilution, 0.75mL was added to 40mL of glycerine resulting in a concentration of 1.8% by volume of dye from the total volume of the mixture. From Stock's law it was calculated that the fracturing fluid has a viscosity of 1000cp at 23˚C-24˚C which is the range of temperature experienced at the laboratory.

### 5.2.2.2 Pipe and Pump Set Up

The fluid injection system is composed of a combination of a hand pump connected to the reservoir with the specimen using steel tubing, pressure transducers and valves. The steel tubing has an external diameter of 3.2 mm (1/8") and 60w allowing glycerin to be pumped into the specimen to initiate and propagate the hydraulic fracturing. This pipe network was constructed using a T connection to communicate the pump with a reservoir and the pump to the specimen as illustrated in Figure 12. On each arm of the piping network there is one valve to allow to pressurize the fluid within the pump chamber prior to injecting into the specimen. The pump is a pressure generator model 62-6-10 with a volumetric capacity of 30 $cm^3$ and a maximum output pressure of 68.9 MPa (10,000 psi) (High Pressure Equipment, 1997). A calibrated pressure transducer is located closed to the pump and within the two valves to provide feedback on the pressure chamber. A needle valve is used in the arm between the pump and the specimen to control the flow rate injected into the specimen.

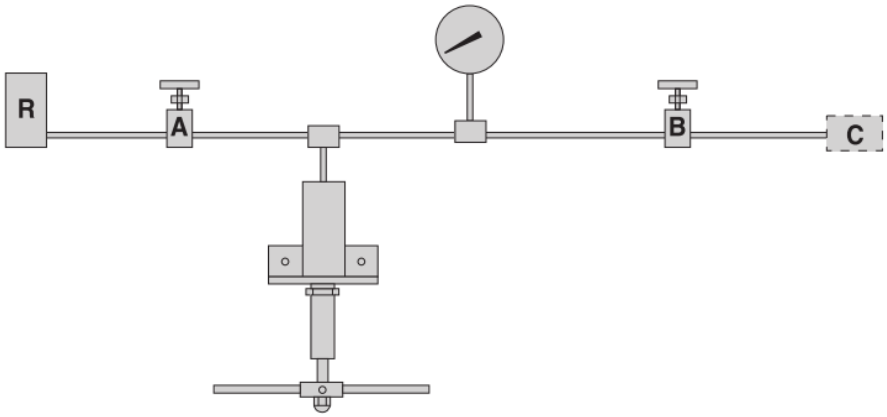


Figure 12: Schematic of fluid injection system depicting the piping connections, R represents the glycerine reservoir, A and B are valves that isolates the pump during pressurization - B is the needle that controls flow rate -, and C is the specimen.

## 5.2.3 Calibration

Prior to commencing testing, the frame needs to be calibrated for visual accuracy. This calibration is for the measurement captured by the camera from the interaction between the light and the coloured injection fluid. This calibration was conducted to ensure the maximum range of grey colours to represent the fracture aperture during test. The results of the calibration consisted in a selection of dye concentration, RGB colour, and selection of light diffuser, to provide a set grey scale that can be related to the fracture

aperture. The light colours considered for this study were blue, green, red, white, and yellow. The dye to glycerine ratio considered for this experiment varied from 1:1 to 1:1000 as illustrated in Figure 13. The best ratio and light combination was the green light with a ratio of 1:108 dye to glycerine and a plastic white diffuser.

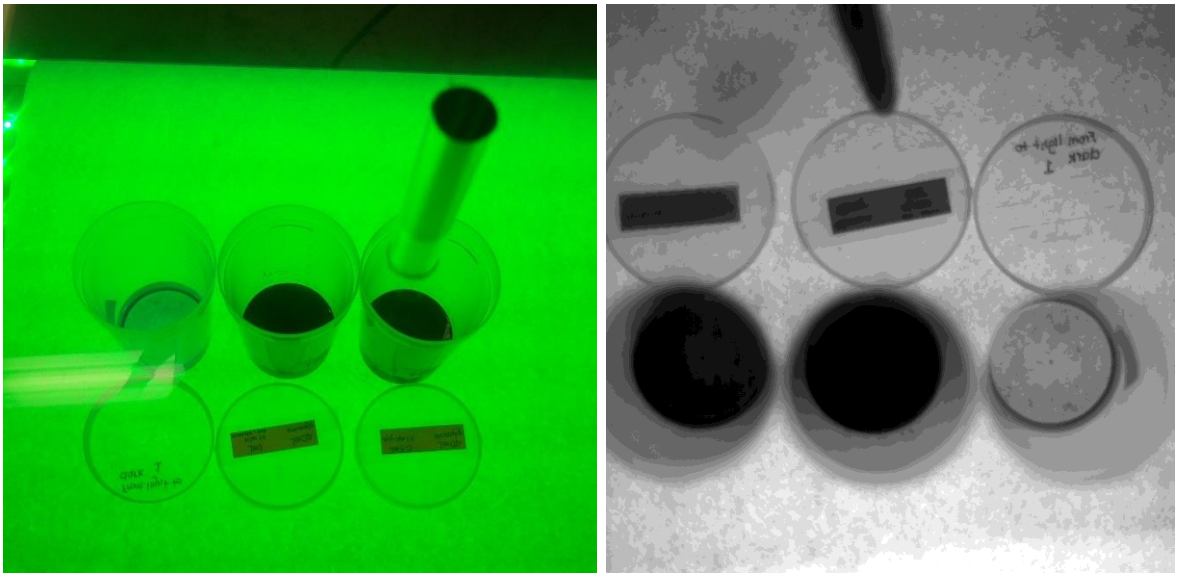

Figure 13: Different ratios of dye to glycerine when using green backlight, left is the colour photo taken with a DSLR camera while on the right it is the black and white photo taken with a high-speed camera. Both these photos were taken with a paper diffuser; this creates an issue in the grey scale with dark spots as it can be appreciated on the black and white photo and more prominently in the light container. The tube above the containers is the injection tube machined into the top layer of the frame.

Wedges were produced with the objective of creating a comprehensive set of grey scale visual aid to determine the fracture aperture. A total of five calibration wedges were produced varying in degrees of 10º, 5º, 3º, 2º, and 1º. Each wedge was filled with the fracturing fluid of the 1:108 dye to glycerine ratio. Two high-speed cameras were used for this calibration, one from the top looking through the PMMA layer into the frame and one from the side for a 3D study. The side camera is supplementary to the overhead camera. Hence, shots from the side camera were not used as there is no backlight, however, a diffuser is used as background. Figure 14 shows a 1º wedge filled with the injection fluid to assess the fracture aperture using the visual field.

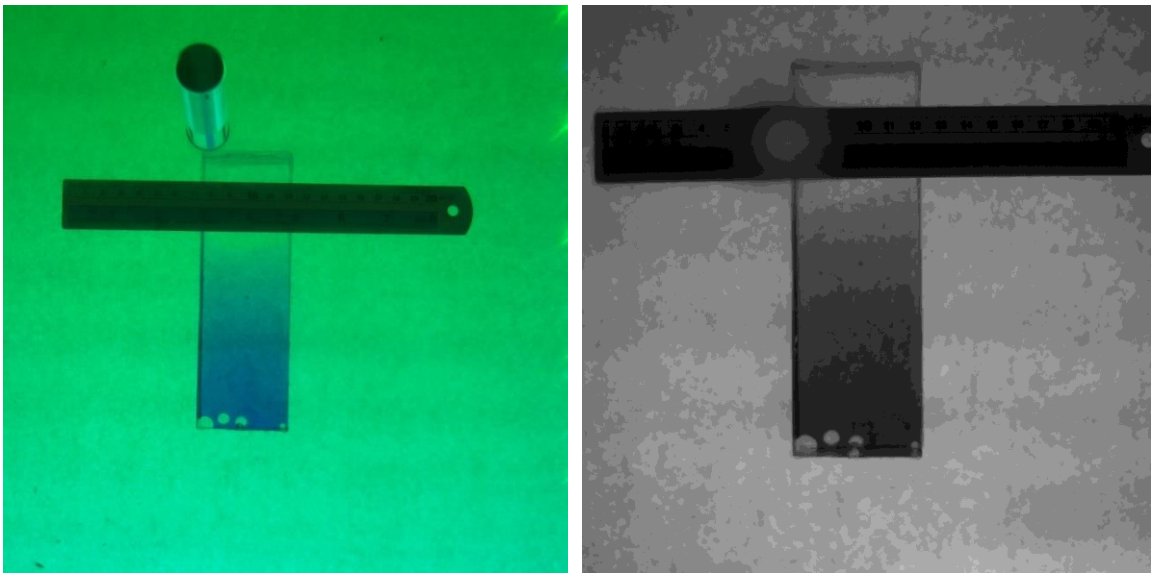

Figure 14: Calibration wedge used to set grey scale that represents fracture aperture while using the selected dye ratio and green backlight. The left photo is using a DSLR camera while the right one is using the high-speed camera.

## 5.3 Specimen

The specimens to be tested in this frame were made of PMMA of 152mm cubes creating a joint set of orthogonal crossbedding. Six 25mm thick layer were annealled to form 152mm by 152mm plates bearing a discontinuity at 50mm from one end of the specimen that is parallel to the edge and normal to the face. Three specimens were fabricated, one being cohesionless that was intended as a benchmark for the study of the other two specimens. The non-cohesive specimen permitted the camera triggering mechanism to be defined. It also allowed to improve the methodology and testing the injection system. prior to testing the two cohesive specimens. The discontinuity for the two cohesive specimens were rotated 90˚ and 180 ˚ from the previous layer for each specimen respectively. The specimen was constructed using the same annealing methodology previously discussed. First, each layer was annealed. Then, the sides of each layer were milled to align to the sides of the cube and to fit into a steel square mold. A 3.2 mm hole was created from the center point on the top of the specimen until the center of the cube, only the three first layers. This serves as borehole and the center of the cube becomes the initiation point for the fracture. Each layer was subjected to an inspection at this point to check the integrity of the annealed interface after the milling process was completed. Each layer was. Then, each layer was cleaned and shined using an acrylic polishing solution, aero gloss chemical, to restore the surface and provide a better visual field ensuring maximum visibility throughout the layers. Once the pieces were cleaned up, they were put in the oven to annealed at 149˚C (300˚F) for 48 hours. Additionally, a polycarbonate box was made from 12.7mm sheets to hold the pieces of the non-cohesive specimen together during testing.

## 5.4 Experimental Procedure

Once calibration and specimen preparation has been completed, testing can commence. The following steps describe the complete testing methodology to achieve an experimental emulation of hydraulic fracturing.

1. Fracturing fluid with the right dye to glycerin ratio placed into the reservoir.
2. Specimen placed into safety box, put into frame, and uniaxial pressure is applied.
3. Pipes connected and glycerin fills pipes prior to pressurization.
4. Uniaxial pressure applied to the desired load using the feedback from the load cell.
5. Needle valve is closed and drawing of hydraulic fluid into pump chamber begins.
6. Once the desired volume of injection fluid is draw into pump, valve is closed.
7. Pressurization begins by turning the pump handle clockwise while reading the transducer to the desired pressure.
8. Lights, DSLR camera, and high-speed cameras are turned on and start to record.
9. Needle valve is opened slightly and injection begins.
10. Recording of high-speed camera is constantly updated as cache only serves to record for a short period.
11. Data collection from cameras, transducers, and load cell is ongoing.
12. Once specimen has been fractured and the injection fluid is finished, test is deemed completed.
13. Specimen removal including piping removal and clean up follows.
14. Data retrieval from cameras, transducers, and load cell is downloaded into a computer.
15. Organization of visual results is conducted.

The visual recordings are converted from videos to stack of images using an imaging software such as ImageJ. Using the grey scale set in the calibration portion, the fracture aperture can be determined as well as the voids that were created from shearing events.

# 6 Conclusions and recommendations

The present study proposes an innovative way to characterize the cohesion of an analogue fracture within a homogeneous medium at the macroscale. The advantage of this testing method is the controlled fracture growth within the compression regime at slow strain rates. The collected data consisted of the displacement and load input to fracture the specimen and the fracture geometry. These measurements are taken at different load input levels. Based on this collected information, the fracture toughness was calculated using Griffith's principles for mode I fracture tension in plane stress. The results show that using this method provides reliable results among specimens. A maximum load input should be determined prior to testing and it is calculated based on the specimen geometry and Euler's critical pressure value to avoid complications due to buckling. Two different approaches were used to analyze the obtained results; these are the ultimate and the mid-point approach. These approaches were adequate for different scenarios in this study. The first three scenarios consisted of changing cooking stress in 12 mm thick specimens; SC04, SC05, and SC06 consisted of the same cooking stresses but in specimens of 25 mm thick; SC07, SC08, and SC09 consisted of the same thickness geometry as those in SC04, SC05, and SC06 and the high cooking stress but different healing times. While SC07, SC08, and SC09 were constrained to a maximum load input during testing improving the results. Thus, these scenarios provided good coefficient of variability in both analyzing methods, while the thin specimens provided better results in the mid-point approach and SC04, SC05, and SC06 performed better in the ultimate point approach. For example, SC01, SC02, and SC03 resulted in low fracture toughness values in both approaches with the range of 0.0139 MPa*$m^{1/2}$ to 0.0191 MPa*$m^{1/2}$; however, the coefficient of variability was reduced when using the mid-point approach from 15% to 8% for SC02. This improvement is attributed to truncating the raw data prior to the effects of buckling. On the other hand, SC04, SC05, and SC06 resulted in fracture toughness between 0.0234 MPa*$m^{1/2}$ to 0.0191 MPa*$m^{1/2}$ with the lower values existing from the mid-point approach. Similarly, the coefficient of variability in these scenarios dramatically increased from 11% in the ultimate point approach for SC04 to 28% when using the mid-point approach. For SC07, SC08, and SC09, the fracture toughness values ranged between 0.0201 MPa*$m^{1/2}$ to 0.0239 MPa*$m^{1/2}$; having higher values when using the ultimate load approach. Nevertheless, the coefficient of variability decreased from 13% in the ultimate load approach to 9% in the mid-point approach for SC09. SC07, SC08, and SC09 were subjected to a prescribed maximum load input which helped provide more coherent results using both approaches.

Six specimens from SC09-CT were tested using the standard compact tension test. It yielded an average fracture toughness of 1.121 MPa*$m^{1/2}$ with a standard deviation of 0.2344 MPa*$m^{1/2}$; and a coefficient of variability of 21%. These values are a much better approximation of the fracture toughness. This value

is in similar range to that of the intact specimen – scenario 0 – with 2.811 MPa*$m^{1/2}$. However, only in one specimen exhibited stable fracture propagation and not catastrophic failure for this specimen, which was experienced in all other five specimens. The fracture propagation velocity is rapid and no sequential measurement was possible along a fracture. Some recommendations are to further study higher levels of cooking stress and to find a better way to achieve an accurate estimation of the fractured area. Additionally, more CT tests should be run for other of the scenarios considered in this study to compare the results obtained through both testing procedures and establishing a possible relationship between both, the proposed compression test and the CT tests.

Special attention is given to the interaction between the hydraulic fracture and the pre-existing planes of weakness. This study would be carried out using a costume made frame that was design with the ability to host cube specimens ranging from 15cm to 50cm on the edge. An injection system was put together that can deliver pressures up to 68.9 MPa (10,000 psi). A data collection system was created using visual feed and measurements from a pressure transducer and a load cell.

Natural fracture media plays a deciding role in the total volume of rock mass stimulated. This is due to the wedging effect and shear dilation of the rock mass. This phenomenon can be studied by using the proposed specimen created using the annealing methodology that created the cohesion at the annealed interface. Different joint set geometry should be incorporated in future studies such as the different angles and more than cross-cutting geometries, which were created. Additionally, the presented methodology for hydraulic fracturing combined with the specimen preparation methodology to create rock mass analogues can be applied to study other factors that influence the hydraulic fracture in the field such as the properties of injection fluid and the injection rate.

# References


Aggelis, D., Shiotani, T., & Polyzos, D. (2009). Characterization of surface crack depth and repair evaluation using rayleigh waves. *Cement and Concrete Composites, 31*(1), 77-83.

Aliabdo, A. A. E., & Elmoaty, Abd Elmoaty Mohamed Abd. (2012). Reliability of using nondestructive tests to estimate compressive strength of building stones and bricks. *Alexandria Engineering Journal, 51*(3), 193-203.

American Concrete Institute. (2013). Report on nondestructive test methods for evaluation of concrete in structures. No. ACI 228.2R-13). Michigan: Farmington Hills.

Arruda, E. M., Boyce, M. C., & Jayachandran, R. (1995). Effects of strain rate, temperature and thermomechanical coupling on the finite strain deformation of glassy polymers. *Mechanics of Materials*, *19*(2–3), 193–212. http://doi.org/10.1016/0167-6636(94)00034-E

Ashby, M. F., Shercliff, H., & Cebon, D. (2007). *Materials Engineering, Science, Processing and Design* (2nd ed.). London: Elsevier Ltd.

ASTM C 597-02. (2003). Pulse Velocity Through Concrete. *United States: American Society for Testing Materials*, 4(2), 3-6. http://doi.org/10.1520/C0597-09

ASTM INTERNATIONAL. (1997). Standard Test Method for Plane-Strain Fracture Toughness of Metallic Materials 1. *Annual Book of ASTM Standards*, *90*(Reapproved), 1–31. http://doi.org/10.1520/E0399-09E02.2

ASTM INTERNATIONAL. (2001). E 1820-01: Standard Test Method for Measurement of Fracture Toughness. *Annual Book of ASTM Standards*, (Designation: E 1820-01), 46. Retrieved from http://scholar.google.com/scholar?hl=en&btnG=Search&q=intitle:Standard+Test+Method+for+Measurement+of+Fracture+Toughness#0

ASTM INTERNATIONAL. (2010). Standard Test Method for Flexural Properties of Unreinforced and Reinforced Plastics and Electrical Insulating Materials by Four-Point Bending 1. *Annual Book of ASTM Standards*, 1–8. http://doi.org/10.1520/D6272-10.1

ASTM INTERNATIONAL. (2016). Standard Test Methods for Flexural Properties of Unreinforced and Reinforced Plastics and Electrical Insulating Materials. D790. *Annual Book of ASTM Standards*, 1–12. http://doi.org/10.1520/D0790-15E02.

Ayatollahi, M. R., Torabi, a. R., & Firoozabadi, M. (2015). Theoretical and experimental investigation of brittle fracture in V-notched PMMA specimens under compressive loading. *Engineering Fracture Mechanics*, *135*, 187–205. http://doi.org/10.1016/j.engfracmech.2015.01.005

Barton, N. (2014). Non-linear behaviour for naturally fractured carbonates and frac-stimulated gas-shales, *32*(September), 51–66.

Blanton, T. (1982). An Experimental Study of Interaction Between Hydraulically Induced and Pre-Existing Fractures. *Proceedings of SPE Unconventional Gas Recovery Symposium*, 559–571. http://doi.org/10.2118/10847-MS

Bonnet, E., Bour, O., Odling, N. E., Davy, P., Main, I., Cowie, P., & Berkowitz, B. (2001). Scaling of fracture systems in geological media. *Reviews of Geophysics*, *39*(3), 347–383. http://doi.org/10.1029/1999RG000074

Bunger, A. P. (2006). A photometry method for measuring the opening of fluid-filled fractures. *Measurement Science and Technology*, *17*(12), 3237–3244. http://doi.org/10.1088/0957-0233/17/12/006

Bunger, A. P., Jeffrey, R. G., & Detournay, E. (2004). Toughness-dominated Near-surface Hydraulic Fracture Experiments.

Bunger, A. P., Jeffrey, R. G., & Detournay, E. (2005). Experimental investigation of crack opening asymptotics for fluid-driven fracture. *Strength, Fracture and Complexity*, *3*(2), 139–147. Retrieved from http://www.icf11.com/proceeding/EXTENDED/3773.pdf

Cerrillo, C., Jiménez, A., Rufo, M., Paniagua, J., & Pachón, F. (2014). New contributions to granite characterization by ultrasonic testing. *Ultrasonics, 54*(1), 156-167.

Chai, H., Momoki, S., Kobayashi, Y., Aggelis, D., & Shiotani, T. (2011). Tomographic reconstruction for concrete using attenuation of ultrasound. *NDT & E International, 44*(2), 206-215.

Chaix, J., Garnier, V., & Corneloup, G. (2003). Concrete damage evolution analysis by backscattered ultrasonic waves. *NDT & E International*, *36*(7), 461-469.

Chen, J., Deng, X., Luo, Y., He, L., Liu, Q., & Qiao, X. (2015). Investigation of microstructural damage in shotcrete under a freeze–thaw environment. *Construction and Building Materials, 83*, 275-282.

Cheng, W., Jin, Y., Chen, Y., Zhang, Y., Diao, C., & Wang, Y. (2014). Experimental Investigation about Influence of Natural Fracture on Hydraulic Fracture Propagation under Different Fracturing Parameters, (October), 1712–1718.

Çobanoğlu, İ., & Çelik, S. B. (2008). Estimation of uniaxial compressive strength from point load strength, schmidt hardness and P-wave velocity. *Bulletin of Engineering Geology and the Environment, 67*(4), 491-498.

Del Rıo, L., Jimenez, A., Lopez, F., Rosa, F., Rufo, M., & Paniagua, J. (2004). Characterization and hardening of concrete with ultrasonic testing. *Ultrasonics, 42*(1), 527-530.

Doyle, J. F., & Phillips, J. W. (1989). Manual on Experimental Stress Analysis Fifth Edition Society for Experimental Mechanics. *Society for Experimental*. Retrieved from http://scholar.google.com/scholar?hl=en&btnG=Search&q=intitle:Manual+on+Experimental+Stress+Analysis#0

Duan, A., Jin, W., & Qian, J. (2011). Effect of freeze–thaw cycles on the stress–strain curves of unconfined and confined concrete. *Materials and Structures, 44*(7), 1309-1324.

Dusseault, M.B. (2015). Geomechanics in Shale Gas Development. A Keynote Lecture. *Proc. VII South American Congress on Rock Mechanics,* Buenos Aires, Argentina, Nov 15-18, 27 p

Ensminger, D., & Bond, L. J. (2011). *Ultrasonics: Fundamentals, technologies, and applications* CRC Press.

Gaydecki, P., Burdekin, F., Damaj, W., & John, D. (1992). The propagation and attenuation of medium-frequency ultrasonic waves in concrete: A signal analytical approach. *Measurement Science and Technology, 3*(1), 126.

Gdoutos, E. E. (1993). *Fracture Mechanics: An Introduction*. Boston: Kluwer Academic Publishers.

Gerstle, W. (2010). Progress in developing a standard fracture toughness test for concrete. *Structures Congress 2010,* 1915-1926.

Gil, I., Nagel, N., Sanchez-Nagel, M., & Damjanac, B. (2011). The Effect of Operational Parameters on Hydraulic Fracture Propagation in Naturally Fractured Reservoirs – Getting Control of the Fracture Optimization Process. *45th US Rock Mechanics / Geomechanics Symposium Held in San Francisco, CA, June 26–29, 2011.*, (2010).

Gomez Rodriguez, D. M.., Dusseault, M. B., & Gracie, R. (2016). Cohesion and Fracturing in a Transparent Jointed Rock Analogue. *50th US Rock Mechanics / Geomechanics Symposium*.

Grinzato, E., Marinetti, S., Bison, P., Concas, M., & Fais, S. (2004). Comparison of ultrasonic velocity and IR thermography for the characterisation of stones. *Infrared Physics & Technology, 46*(1), 63-68.

Haeri, H., Shahriar, K., Marji, M. F., & Moarefvand, P. (2013). A coupled numerical-experimental study of the breakage process of brittle substances. *Arabian Journal of Geosciences*, 1–17. http://doi.org/10.1007/s12517-013-1165-1

Haeri, H., Shahriar, K., Marji, M. F., & Moarefvand, P. (2014). Cracks coalescence mechanism and cracks propagation paths in rock-like specimens containing pre-existing random cracks under compression. *Journal of Central South University*, *21*(6), 2404–2414. http://doi.org/10.1007/s11771-014-2194-y

Hellier, C. (2001). Handbook of nondestructive evaluation.

Hertlein, B. H. (2013). Stress wave testing of concrete: A 25-year review and a peek into the future. *Construction and Building Materials, 38*, 1240-1245.

High Pressure Equipment. (1997). Pumping Systems, Intensifiers, Gas Boosters and High Pressure Generators.

Hobbs, B., & Kebir, M. T. (2007). Non-destructive testing techniques for the forensic engineering investigation of reinforced concrete buildings. *Forensic Science International, 167*(2), 167-172.

Hooton, R., Hanson, J., & Ingraffea, A. (1997). Standards for Fracture Toughness Testing of Rock and Manufactured Ceramics: What Can We Learn for Concrete? *Cement, Concrete and Aggregates*. http://doi.org/10.1520/CCA10322J

Hossain, M. M., Rahman, M. K., Rahman, S. S., New, U., & Wales, S. (2002). A Shear Dilation Stimulation Model for Production Enhancement From Naturally Fractured Reservoirs. *SPE 78355*, (January), 1–4.

Hubbert, M., & Willis, D. (1972). Mechanics of hydraulic fracturing. *Underground Waste Management and Environmental Implications*, 239–257. http://doi.org/10.1016/S0376-7361(07)53011-6

Inglis, C. E. (1913). Stresses in a plate due to the presnce of cracks and sharp corners. *Trans. Inst. Naval Arch.*, *55*, 219–239.

Ishida, T., Chen, Q., Mizuta, Y., & Roegiers, J.-C. (2004). Influence of Fluid Viscosity on the Hydraulic Fracturing Mechanism. *Journal of Energy Resources Technology*, *126*(3), 190. http://doi.org/10.1115/1.1791651

Jeffrey, R. G., & Bunger, A. P. (2007). A Detailed Comparison of Experimental and Numerical Data on Hydraulic Fracture Height Growth Through Stress Contrasts. In *SPE Hydraulic Fracturing Technology*. http://doi.org/SPE 106030

Jeffrey, R. G., Bunger, A. P., Petroleum, C., Lecampion, B., Zhang, X., Chen, Z. R., … Associates, G. (2009). SPE 124919 Measuring Hydraulic Fracture Growth in Naturally Fractured Rock, 1–19.

Jiefan, H., Ganglin, C., Yonghong, Z., & Ren, W. (1990). An Experimental Study of the Strain Field Development Prior to Failure of a Marble Plate Under Compression. *Tectonophysics*, *175*, 269–284.

Jud, K., Kausch, H. H., & Williams, J. G. (1981). Fracture mechanics studies of crack healing and welding of polymers. *Journal of Materials Science*, *16*(1), 204–210. http://doi.org/10.1007/BF00552073

Kahraman, S. (2001). Evaluation of simple methods for assessing the uniaxial compressive strength of rock. *International Journal of Rock Mechanics and Mining Sciences*, *38*(7), 981-994.

King, G. E., & Corporation, A. (2012). SPE 152596 Hydraulic Fracturing 101 : What Every Representative , Environmentalist , Regulator , Reporter , Investor , University Researcher , Neighbor and Engineer Should Know About Estimating Frac Risk and Improving Frac Performance in Unconventional Ga, 1–80.

Kirlangic, A. S. (2013). Condition assessment of cemented materials using ultrasonic surface waves.

Krautkrämer, J., & Krautkrämer, H. (2013). *Ultrasonic testing of materials* Springer Science & Business Media.

Lee, H., & Jeon, S. (2011). An experimental and numerical study of fracture coalescence in pre-cracked specimens under uniaxial compression. *International Journal of Solids and Structures*, *48*(6), 979–999. http://doi.org/10.1016/j.ijsolstr.2010.12.001

Ludovico-Marques, M., Chastre, C., & Vasconcelos, G. (2012). Modelling the compressive mechanical behaviour of granite and sandstone historical building stones. *Construction and Building Materials, 28*(1), 372-381.

Malek, J., & Kaouther, M. (2014). Destructive and non-destructive testing of concrete structures. *Jordan Journal of Civil Engineering, Volume No8.PP432-441., Year2014,*

Material Testing Systems. (2006). MTS 810 & 858 Material Testing Systems.

Material Testing Systems. (2009). Series MTS 322 Load Frame. http://doi.org/10.1007/s00299-011-1150-7

Mikulić, D., Pauše, Ž., & Ukrainčik, V. (1992). Determination of concrete quality in a structure by combination of destructive and non-destructive methods. *Materials and Structures, 25*(2), 65-69.

Mitra, S., & Ghosh, K. (2009). Two-dimensional simulation of controls of fracture parameters on fracture connectivity. *AAPG Bulletin*. http://doi.org/10.1306/07270909041

Moës, N., Dolbow, J., & Belytschko, T. (1999). A finite element method for crack growth without remeshing. *Int. J. Numer. Meth. Engng*, *46*(1), 131–150. http://doi.org/10.1002/(SICI)1097-0207(19990910)46:1<131::AID-NME726>3.0.CO;2-J

Montgomery, C. T., Smith, M. B., Technologies, N. S. I., Fracturing, H., Cooke, C. E., Dollarhide, F. E., … Poollen, H. K. Van. (2010). Hydraulic Fracturing: History of an Enduring Technology. *Journal of Petroleum Technology*, (December), 26–41. Retrieved from http://www.spe.org/jpt/print/archives/2010/12/10Hydraulic.pdf

Motoki, A., & Sichel, S. E. (2008). Hydraulic fracturing as a possible mechanism of dyke-sill transitions and horizontal discordant intrusions in trachytic tabular bodies of Arraial do Cabo, State of Rio de Janeiro, Brazil. *Geofisica Internacional*, *47*(1), 13–25.

Naik, Tarun R., V. Mohan Malhotra, and John S. Popovics. (2004). The ultrasonic pulse velocity method. *In Handbook of Nondestructive Testing of Concrete (Malhotra, V.M. and Carino, N.J.Editors)Boca Raton, Florida: CRC Press,*

Nolen-hoeksema, R. (2013). Elements of Hydraulic Fracturing. *Oilfield Review*, (2), 51–52.

Papadopoulos, J. M., Narendran, V. M., & Cleary, M. P. (1983). Laboratory Simulations of Hydraulic Fracturing. In *SPE/DOE Symposium on Low Permeability* (pp. 161–168). http://doi.org/SPE/DOE 11618

Papadopulos, S. S., Bredehoeft, J. D., & Cooper, H. H. (1973). On the analysis of "slug test" data. *Water Resources Research*, *9*(4), 1087. http://doi.org/10.1029/WR009i004p01087

Park, C. H., & Bobet, a. (2010). Crack initiation, propagation and coalescence from frictional flaws in uniaxial compression. *Engineering Fracture Mechanics*, *77*(14), 2727–2748. http://doi.org/10.1016/j.engfracmech.2010.06.027

Rubin, M. B. (1983). Experimental Study of Hydraulic Fracturing in an Impermeable Material. *JOURNAL OF ENERGY RESOURCES TECHNOLOGY.*, *105*(June), 116–124.

Sahouryeh, E., Dyskin, a. V., & Germanovich, L. N. (2002). Crack growth under biaxial compression. *Engineering Fracture Mechanics*, *69*(18), 2187–2198. http://doi.org/10.1016/S0013-7944(02)00015-2

Santamarina, J. C., & Fratta, D. (1998). *Introduction to discrete signals and inverse problems in civil engineering*

Shiotani, T., & Aggelis, D. G. (2009). Wave propagation in cementitious material containing artificial distributed damage. *Materials and Structures*, *42*(3), 377-384.

Tang, C. a., Lin, P., Wong, R. H. C., & Chau, K. T. (2001). Analysis of crack coalescence in rock-like materials containing three flaws—Part II: numerical approach. *International Journal of Rock Mechanics and Mining Sciences*, *38*(7), 925–939. http://doi.org/10.1016/S1365-1609(01)00065-X

Tang, H., Zhu, Z., Zhu, M., & Lin, H. (2015). Mechanical Behavior of 3D Crack Growth in Transparent Rock-Like Material Containing Preexisting Flaws under Compression. *Advances in Materials Science and Engineering*, *2015*, 10. Retrieved from http://dx.doi.org/10.1155/2015/193721

Tattersall, H. G., & Tappin, G. (1966). The work of fracture and its measurement in metals, ceramics and other materials. *Journal of Materials Science*, *1*(3), 296-301.

Trtnik, G., Kavčič, F., & Turk, G. (2009). Prediction of concrete strength using ultrasonic pulse velocity and artificial neural networks. *Ultrasonics*, *49*(1), 53-60.

Ulusay, R. (2015). The ISRM suggested Methods for Rock Characterization, Testing and Monitoring: 2007-2014. DOI 10.1007/978-3-319-07712-3, SPRINGER, 290 pp.

Vasconcelos, G., Lourenço, P., Alves, C., & Pamplona, J. (2008). Ultrasonic evaluation of the physical and mechanical properties of granites. *Ultrasonics*, *48*(5), 453-466.

Washabaugh, P. D., & Knauss, W. G. (1995). The effect of aligned defects on the propagation speed of a dynamic crack in PMMA. *International Journal of Solids and Structures*, *32*(17–18), 2481–2896. http://doi.org/10.1016/0020-7683(94)00278-5

Xing, P., Bunger, A. P., Yoshioka, K., Adachi, J., & El-Fayoumi, A. (2016). Experimental study of hydraulic fracture containment in layered reservoirs. *50th US Rock Mechanics / Geomechanics Symposium*.

Yang, S. Q. (2011). Crack coalescence behavior of brittle sandstone samples containing two coplanar fissures in the process of deformation failure. *Engineering Fracture Mechanics*, *78*(17), 3059–3081. http://doi.org/10.1016/j.engfracmech.2011.09.002

Yasar, E., & Erdogan, Y. (2004). Correlating sound velocity with the density, compressive strength and young's modulus of carbonate rocks. *International Journal of Rock Mechanics and Mining Sciences, 41*(5), 871-875.

Yim, H. J., Kwak, H., & Kim, J. H. (2012). Wave attenuation measurement technique for nondestructive evaluation of concrete. *Nondestructive Testing and Evaluation, 27*(1), 81-94.

Zeng, Z., & Roegiers, J. (2002). Experimental Observation of Injection Rate Influence on the Hydraulic Fracturing Behavior of a Tight Gas Sandstone. In *SPE/ISRM Rock Mechanics Conference*. http://doi.org/SPE / ISRM 78172

Zoback, M. D., Rummel, F., Jung, R., & Raleigh, C. B. (1977). Laboratory hydraulic fracturing experiments in intact and pre-fractured rock. *International Journal of Rock Mechanics and Mining Sciences & Geomechanics Abstracts*, *14*(2), 49–58. http://doi.org/10.1016/0148-9062(77)90196-6

# Appendix A: Supporting Material of Research

**METHODOLOGY : Cooking Frame Design**

Specimens were annealed under different conditions of time and stresses. These stresses are applied perpendicular to the interface. Thus, a special frame sandwiches the cooking specimen on the thickness face was designed. Figure 1 below shows a steel plate, a component of the jig used to create 6" wide slabs, a similar shorter one is used to create the 101mm specimens.

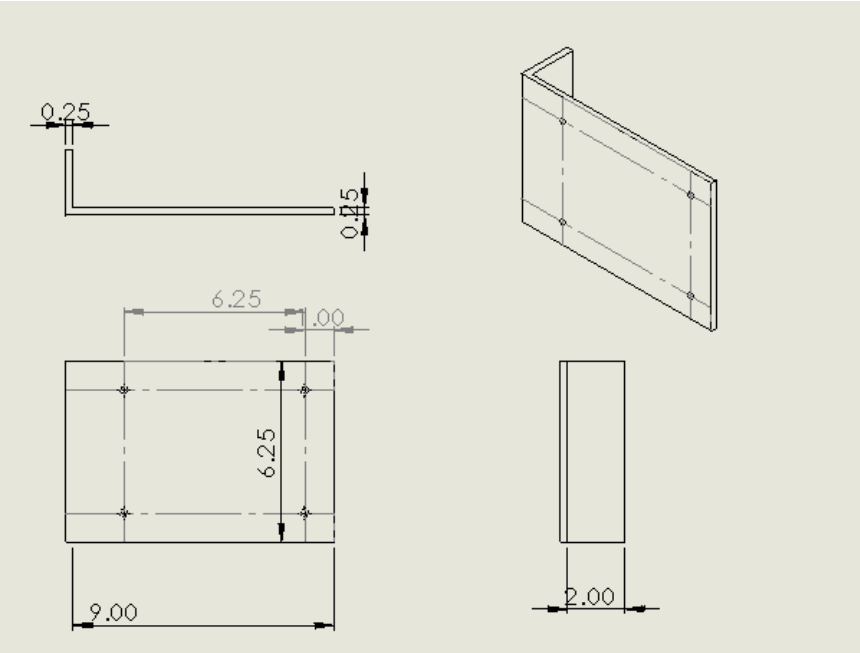


Figure 1: Schematic of steel plate used to create jig used for annealing of specimens of 152mm wide PMMA specimens. Two of these plates, four screws, and four nuts, are needed to create a single jig. The four holes that hold the screws are located 152mm apart to aligned the pieces together.

**Testing: Photo Sequence**

To characterize the fracture toughness of the annealed interface in a stable propagation test, the rectangular plate specimen was loaded uniaxially parallel to the annealed surface. The fracture intiation point was designed as a circular opening at the center of the rectangular plate that cross-cuts the annealed surface. The specimens were tested using a rigid uniaxial frame in compression operated in dynamic load and fixed displacement. The frame was programmed to moved at 0.1mm/min or at 1mm per every 10 mins. The following series of figures are an extract of three specimens during testing and their corresponding fracture toughness calculations. The first series displays an intact specimen, SC00-01, from figure 2 to figure 7. The second photo series displays SC03-06, a thin specimen of 12mm thick during testing between figures 8 and 13 and table 1 for specimen calculations. The last series of photos displays SC04-01, a thick specimen of 24mm being compressed in figures 14 to 22 and table 2 for specimen calculations.

**Solid specimen (SC00-01) photo series**

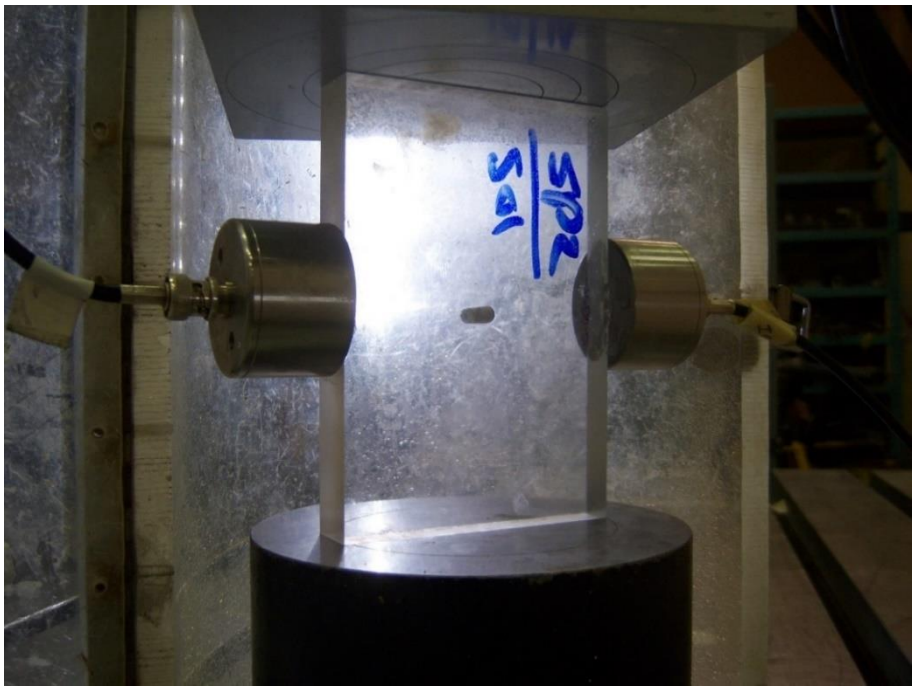


Figure 2: Intact specimen at beginning of the test with no compressive load. This specimen was used for the Ultrasonic Pulse Velocity (UPV) study presented in Appendix C. Thus, the specimen was subjected to non-destructive testing during the compressive test by sending a signal from the piezoelectric transducer glued to one end of the specimen and received by the other piezoelectric transducer located across the specimen.

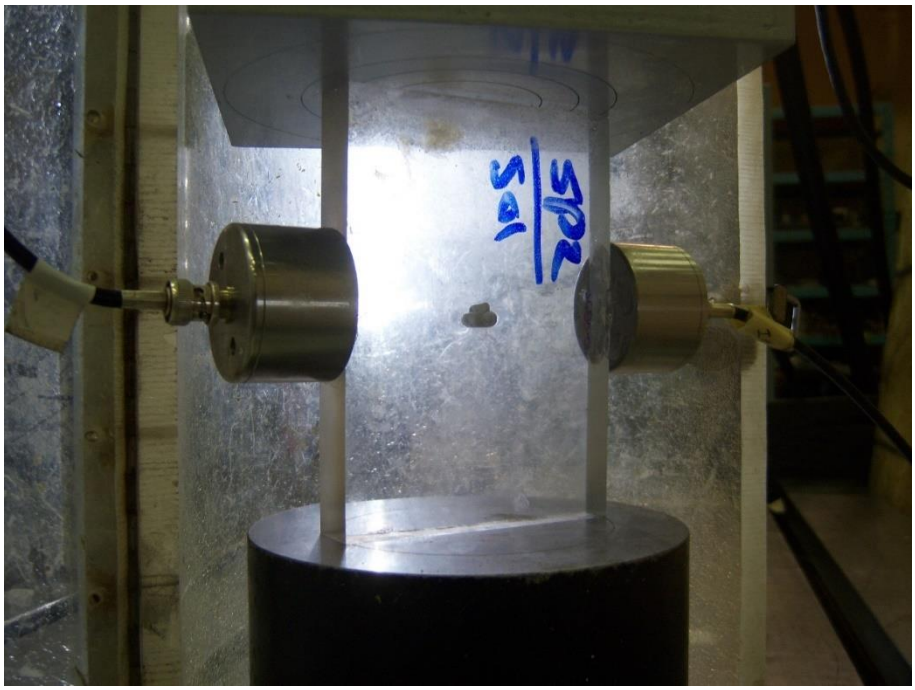


Figure 3: Fracture propagation initiated in upper arm at 110kN and 3.06mm of compressive load and displacement respectively. The upper fracture length is only 2mm on the upper arm while the lower arm has not started to propagate.

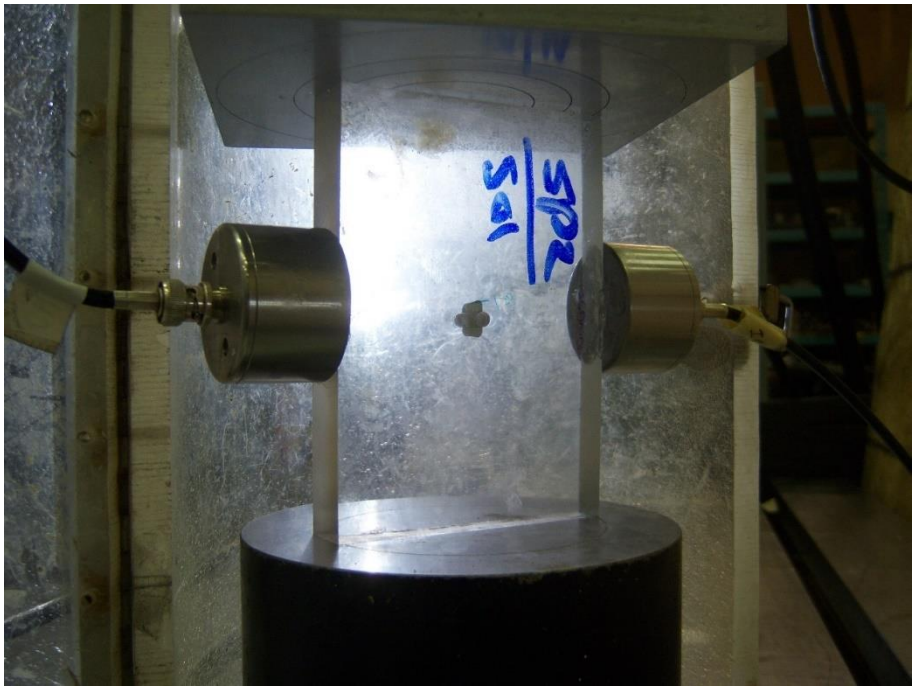

Figure 4: Photo taken at 120kN and 3.81mm compressive displacement respectively. The upper arm fracture propagated 1mm to 3mm. The lower arm fracture initiated and propagated to 4mm.

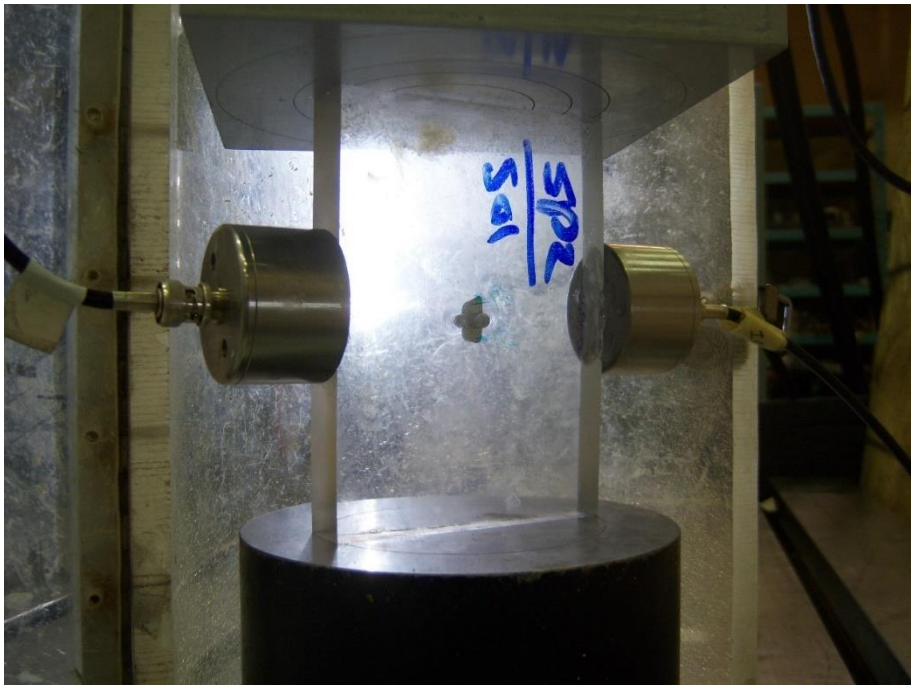

Figure 5: Photo taken at 130kN and 4.25mm compressive displacement respectively. The upper arm fracture propagated on the front face of the specimen more than at the rear face. This creates a small wave on the fracture front of the upper arm. The measured fracture length was 4mm at the maximum point of the fracture point. Nevertheless, the lower arm fracture front remains smooth and flat with 5mm propagation.

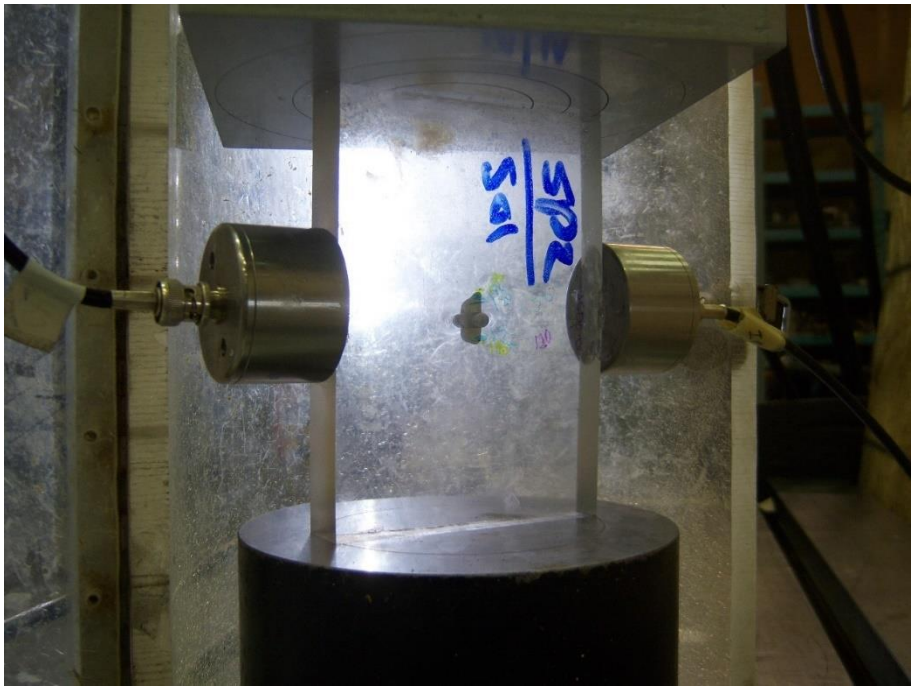

Figure 6: Photo taken at 140kN and 4.76mm compressive displacement respectively. The upper arm fracture propagated to 6mm and the lower arm fracture propagated to 6mm. The fracture length is equal in both arms.

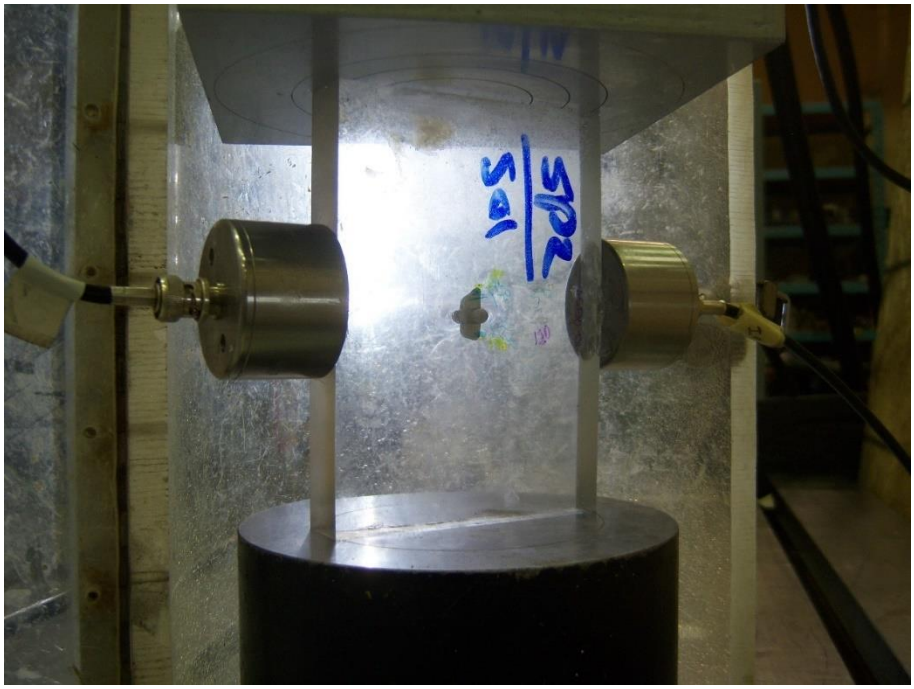

Figure 7: Photo taken at 150kN and 5.36mm compressive displacement respectively. The upper arm fracture propagated to 8mm and the lower arm fracture propagated to 7mm. This is the ultimate load point as it is the maximum load the specimen was subjected to; thus, the fracture maximum extension are the measurements at this point.

**Thin specimen (SC03-06) photo series:** Specimen has the same geometry as scenarios 1, 2, and 3.

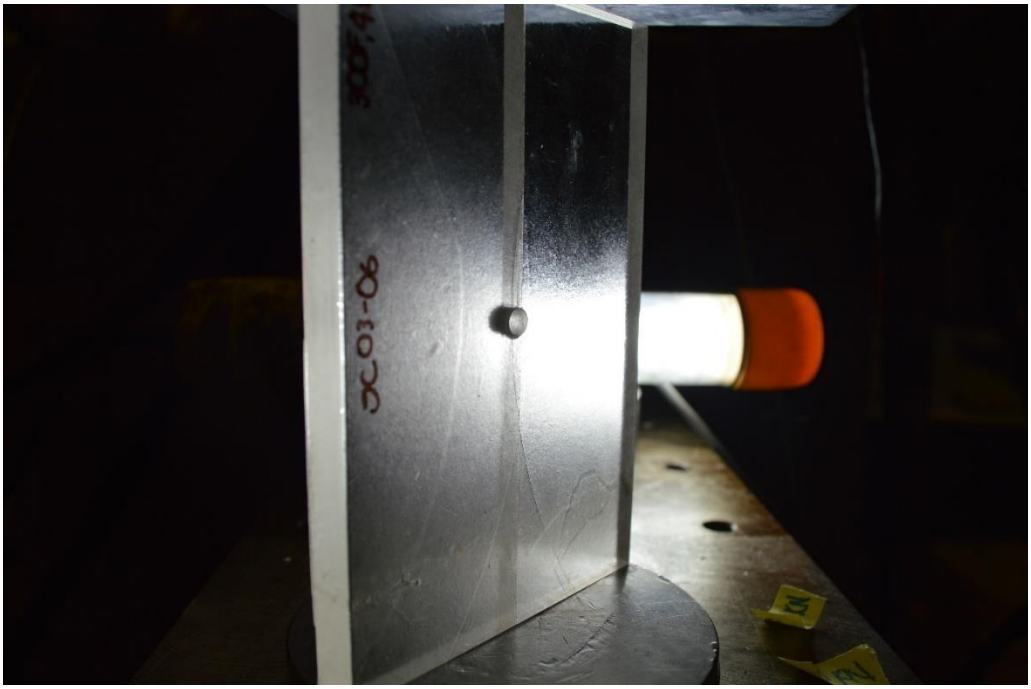


Figure 8: Thin specimen at beginning of the test with no compressive load.

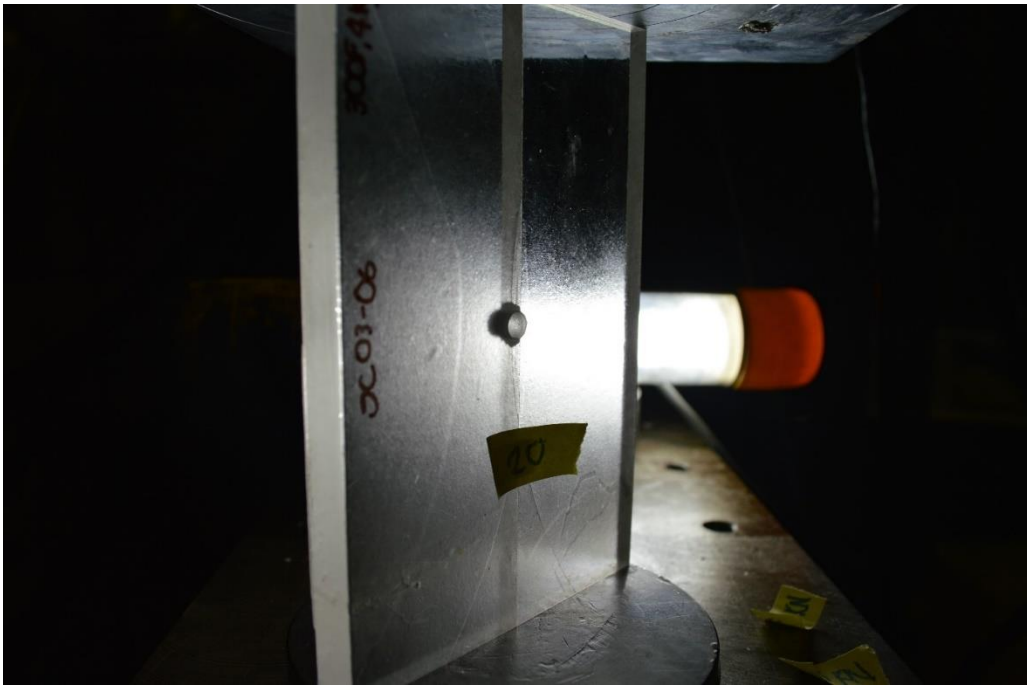


Figure 9: Fracture propagation initiated in upper arm and lower arms at 20kN and 1.32mm of compressive load and displacement respectively. The upper fracture length is 2mm on the upper arm while the lower arm is only 1mm.

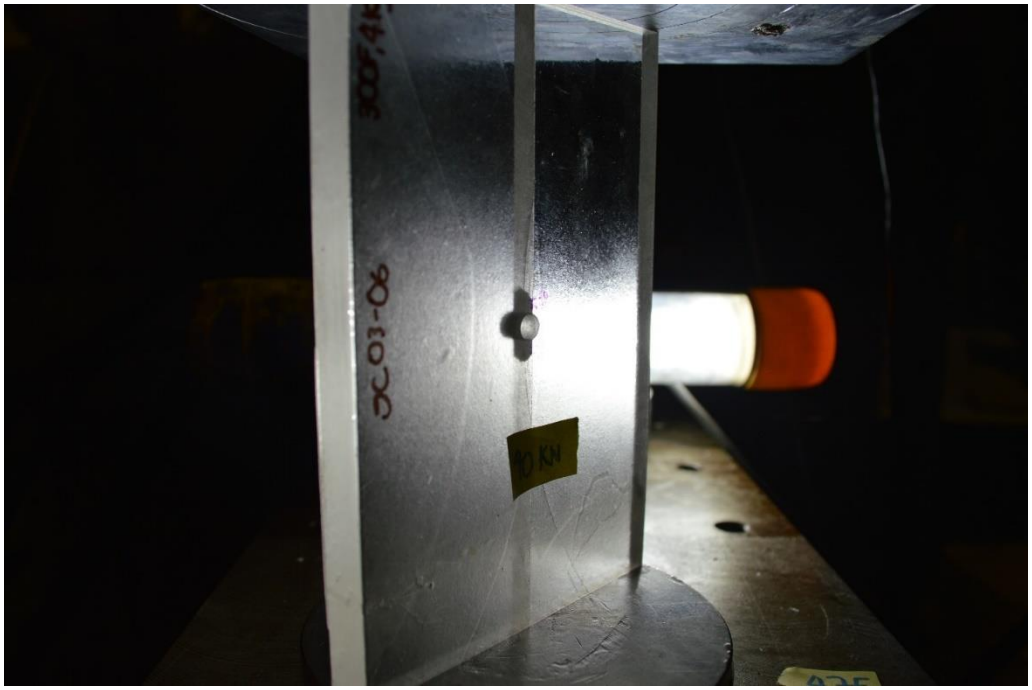


Figure 10: Photo taken at 40kN and 2.45mm compressive displacement respectively. The upper arm fracture propagated to 6mm and the lower arm fracture propagated to 5mm. The upper arm of the fracture is starting to show signs of tunneling as extension of the fracture is longer on the rear face of the specimen but the oval is still present.

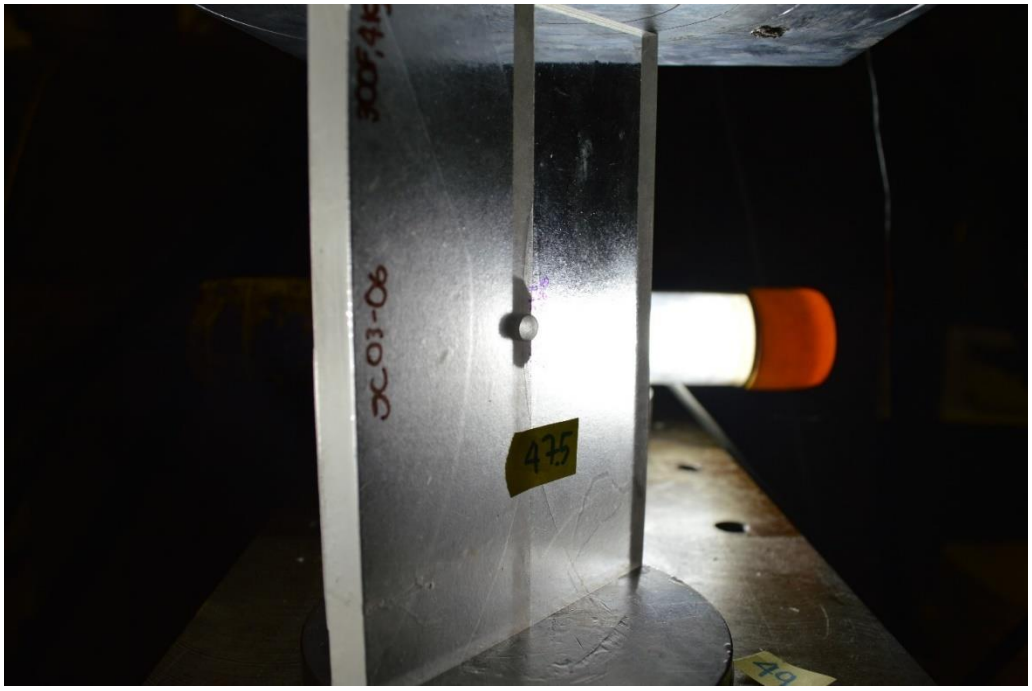


Figure 11: Photo taken at 47.5kN and 2.95mm compressive displacement respectively. The upper arm fracture propagated to 10mm and the lower arm fracture propagated to 6mm. The upper arm of the fractures are now showing a more defined fracture front with some tunneling. The extension of the fracture on the rear face of the specimen is longer and only half arch remains.

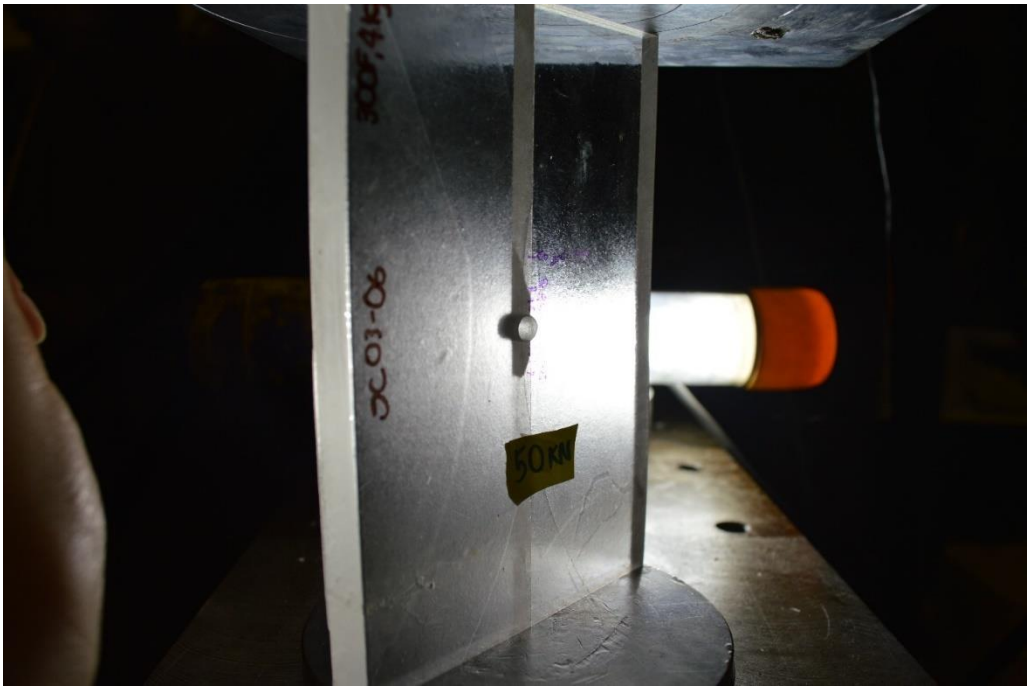


Figure 12: Photo taken at 50kN and 3.13mm compressive displacement respectively. The upper arm fracture propagated to 13mm and the lower arm fracture propagated to 12mm. The upper arm of the fracture are showing tunneling at the fracture front with a clear extension of the fracture on the rear face of the specimen and now some tunneling is visible on the lower arm.

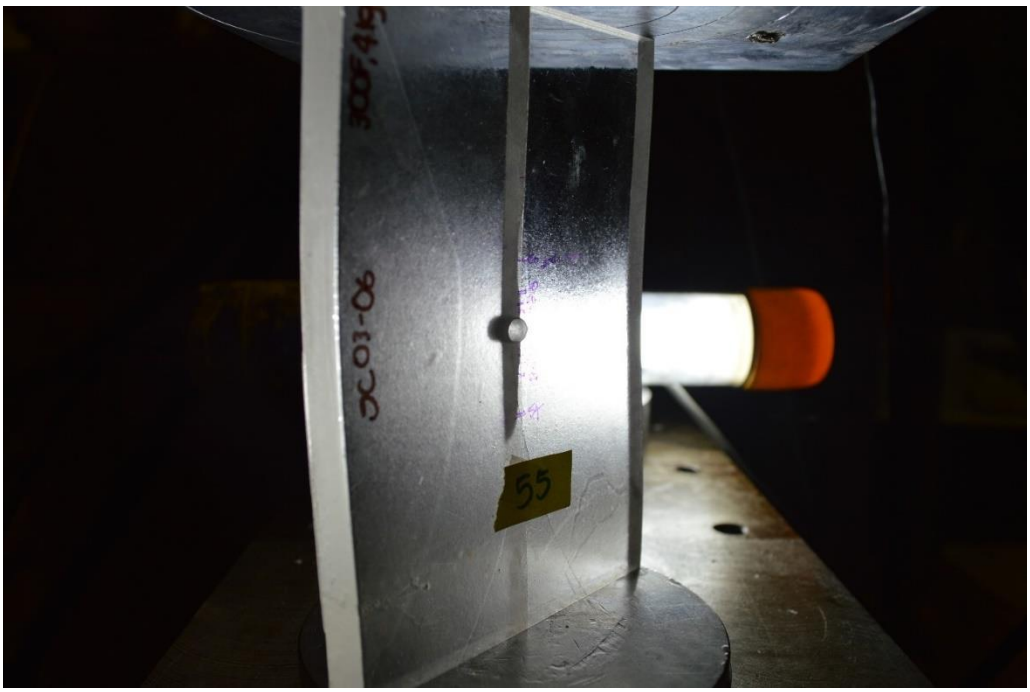


Figure 13: Photo taken at 54.9kN and 3.69mm compressive displacement respectively. The upper arm fracture propagated to 37mm and the lower arm fracture propagated to 23mm. The upper arm has run out of the illuminated section. The lower arm shows tunneling with the more extensive side of the fracture being on the rear face of the specimen. This is the ultimate loading point as it is the maximum load the specimen was subjected to.

Table 1: Specimen SC03-06 results typical of thin specimens. The results come from calculations performed on the raw data from the compression frame along with geometry of the specimen. The fracture length is taken from the marks taken at the load measurements where the above photos were taken.

UPPER

| Load (kN) | Length (mm) | dA (mm^2) | dU (J) | G | Ki (MPa*m^1/2) |
|---|---|---|---|---|---|
| 20 | 2 | 22 | 5.633711 | 0.256078 | 0.025302 |
| 30 | 4 | 44 | 11.19966 | 0.254538 | 0.025226 |
| 40 | 6 | 66 | 16.80735 | 0.254657 | 0.025232 |
| 50 | 13 | 143 | 22.46503 | 0.157098 | 0.019818 |
| 54 | 32 | 352 | 24.97993 | 0.070966 | 0.01332 |
| 55 | 37 | 407 | 25.98731 | 0.063851 | 0.012634 |
| 52.85714 | 15 | 165 | 24.19346 | 0.146627 | 0.019146 |

LOWER.

| Load (kN) | Length (mm) | dA (mm^2) | dU (J) | G | Ki (MPa*m^1/2) |
|---|---|---|---|---|---|
| 20 | 1 | 11 | 5.633711 | 0.512156 | 0.035783 |
| 30 | 3 | 33 | 11.19966 | 0.339384 | 0.029128 |
| 40 | 5 | 55 | 16.80735 | 0.305588 | 0.02764 |
| 50 | 7 | 77 | 22.46503 | 0.291754 | 0.027007 |
| 54 | 12 | 132 | 24.97993 | 0.189242 | 0.021751 |
| 55 | 23 | 253 | 25.98731 | 0.102717 | 0.016025 |
| 56.4 | 15 | 165 | 25.98731 | 0.157499 | 0.019843 |

**Thick specimen (SC04-01) photo series:** Specimen has the same geometry as scenarios 4, 5, 6, 7, 8, and 9.

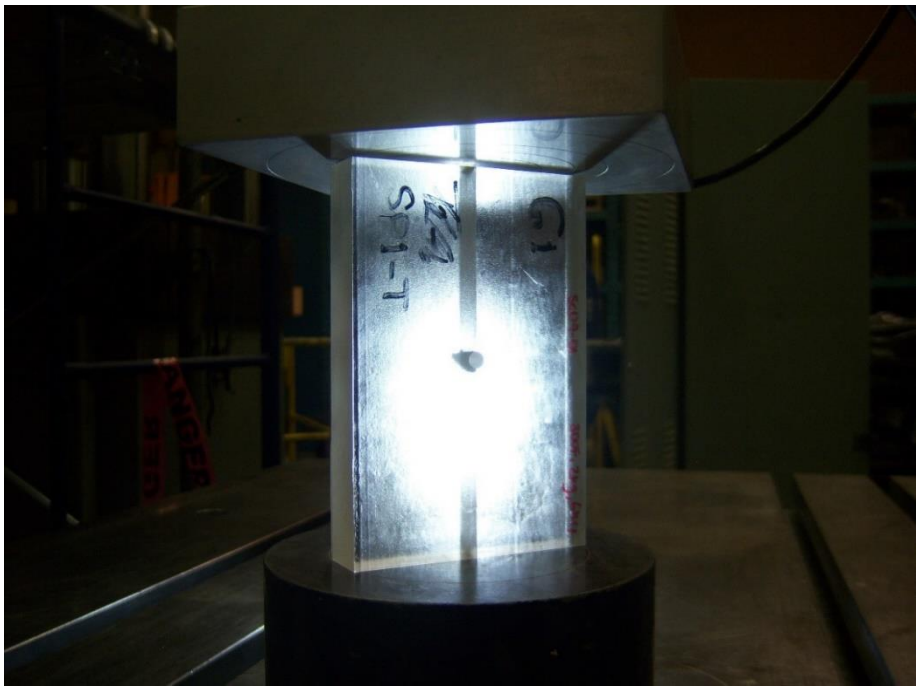

Figure 14: Thick specimen at beginning of the test with no compressive load. Below the center hole there is visible damage measuring 1mm. This 1mm will be subtracted from the total measurements at the time of input into the calculation. The measurements described in the following photos have been reduced by 1mm of damage and they are the input values.

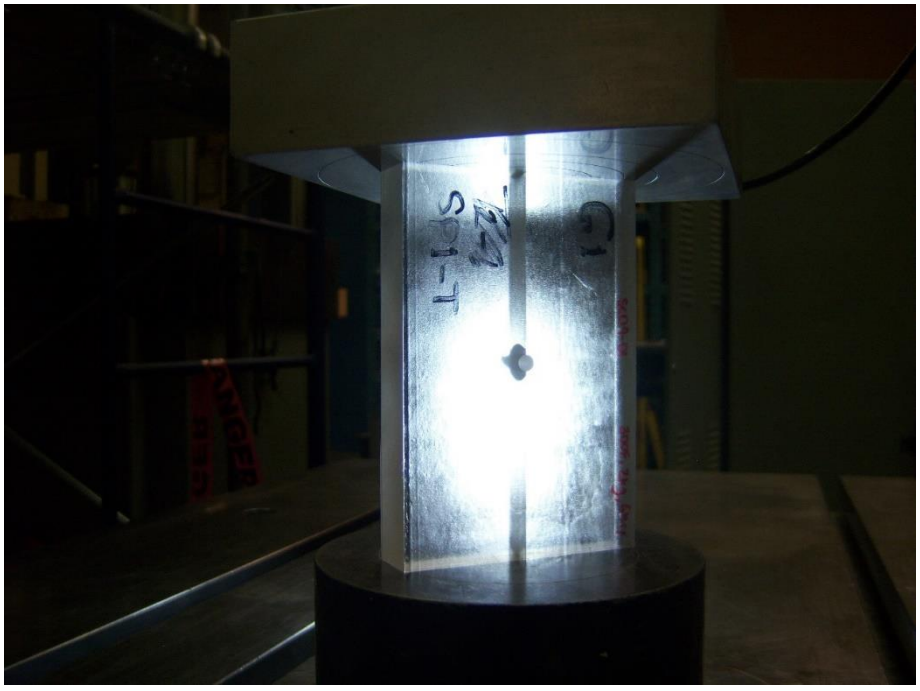

Figure 15: Fracture propagation had initiated in upper arm and lower arms, photo shows propagation at 50kN and 0.89mm of compressive load and displacement respectively. The fracture length is 3mm on both arms at this point.

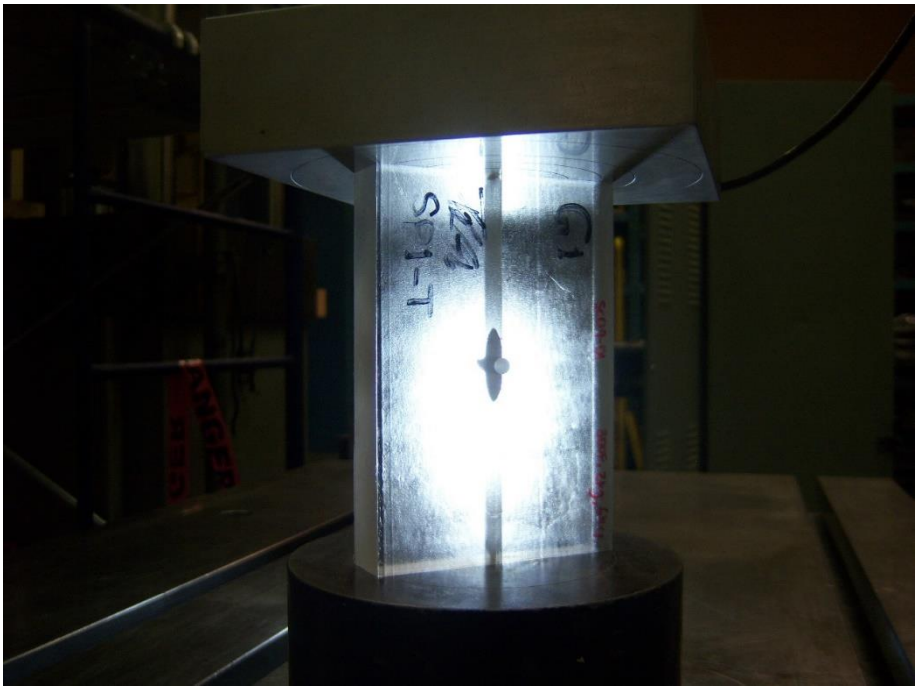

Figure 16: Photo taken at 100kN and 2.74mm compressive displacement respectively. The upper arm fracture propagated to 10mm and the lower arm fracture propagated to 9mm. Both arms are symmetrical in oval shape.

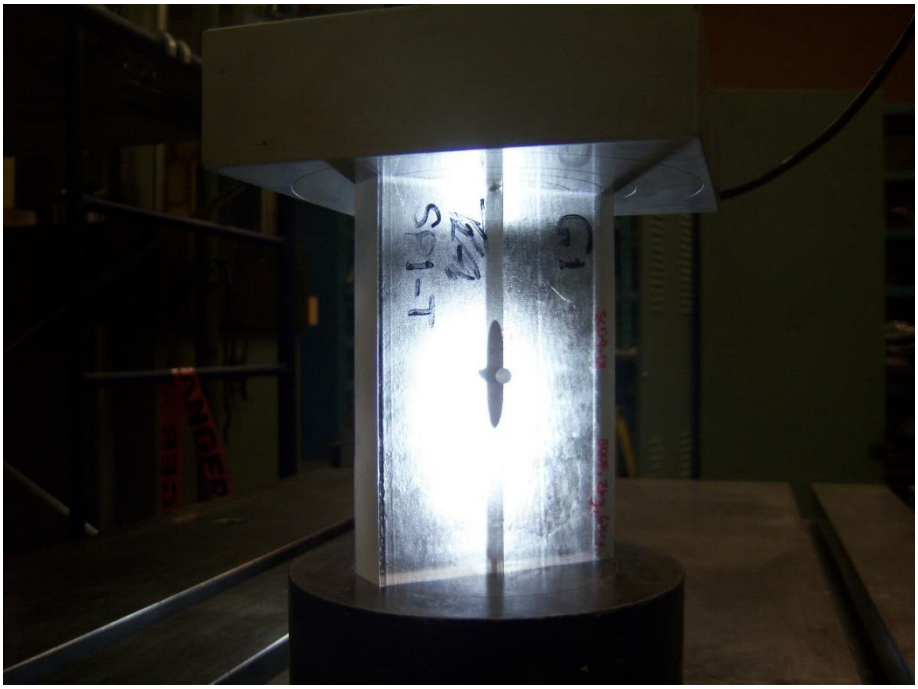

Figure 17: Photo taken at 115kN and 3.25mm compressive displacement respectively. The upper arm fracture propagated to 14mm and the lower arm fracture propagated to 12mm. Both arms are symmetrical oval shape.

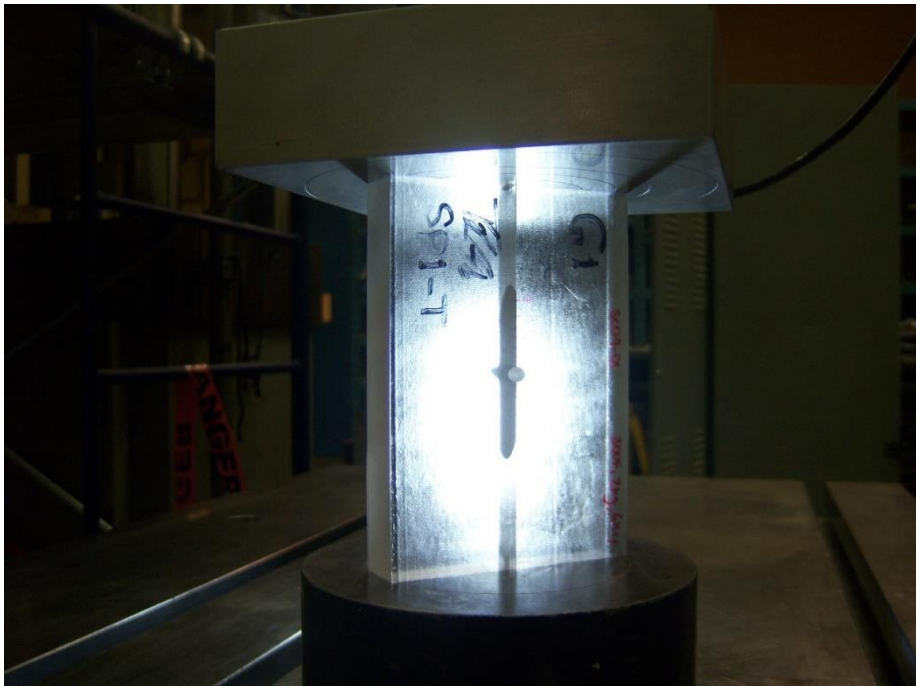

Figure 18: Photo taken at 130kN and 3.88mm compressive displacement respectively. The upper arm fracture propagated to 18mm and the lower arm fracture propagated to 16mm. Both arms have started to show signs of tunneling and the shape of the arms show mirror symmetry about the center hole. The upper arm is moving towards the front face while the lower arm moves towards the rear face.

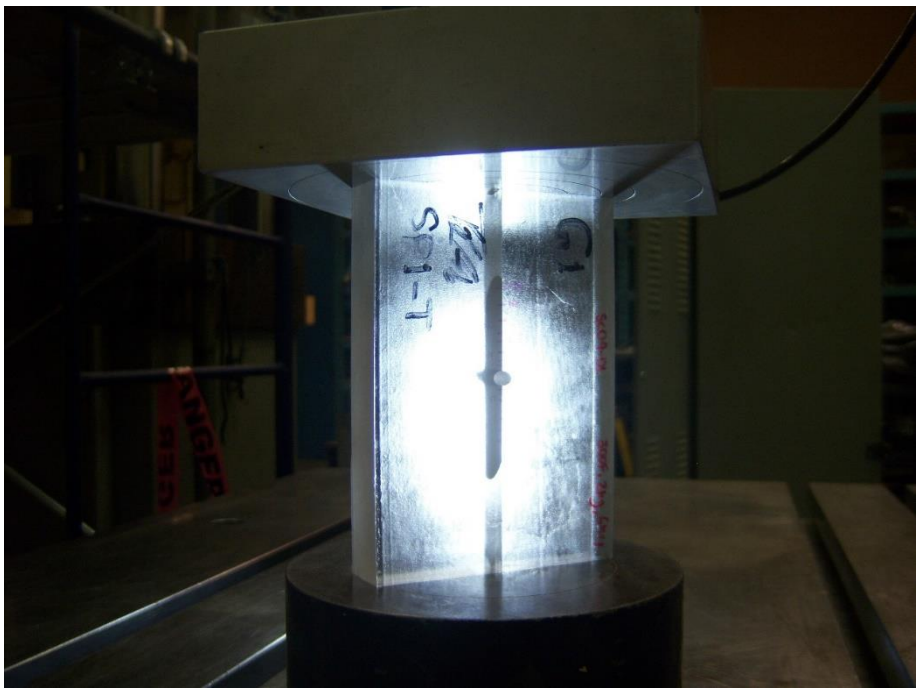

Figure 19: Photo taken at 150kN and 4.95mm compressive displacement respectively. The upper arm fracture propagated to 31mm and the lower arm fracture propagated to 28mm. Both arms show some tunneling at the fracture front and they have mirror symmetry about the center hole.

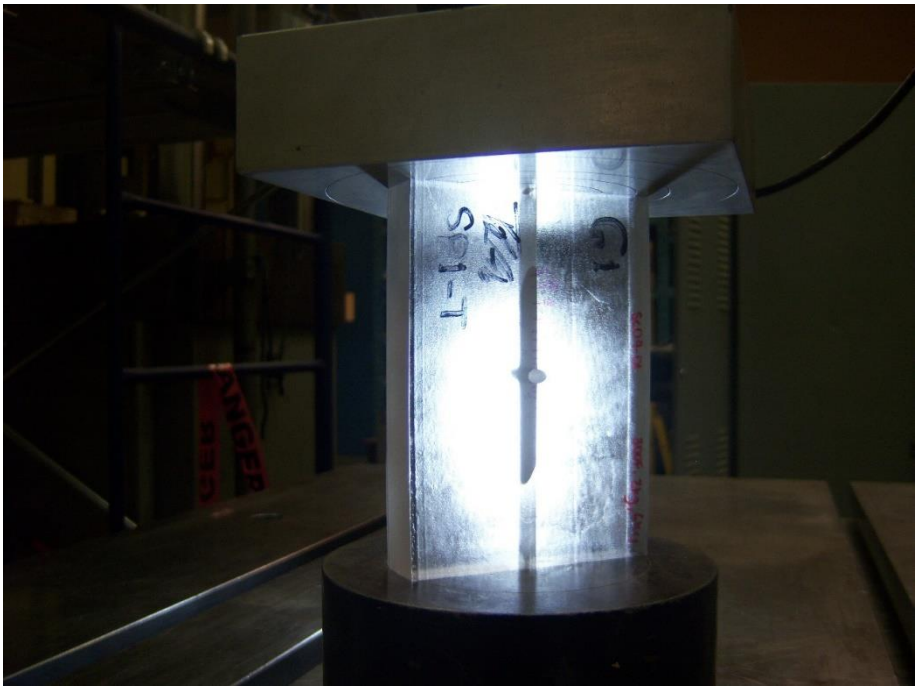

Figure 20: Photo taken at 175kN and 6.82mm compressive displacement respectively. The upper arm fracture propagated to 40 mm and the lower arm fracture propagated to 37mm. Both arms show tunneling and their shape show mirror symmetry about the center hole. The upper arm has moved towards the front face while the lower arm has moved towards the rear face.

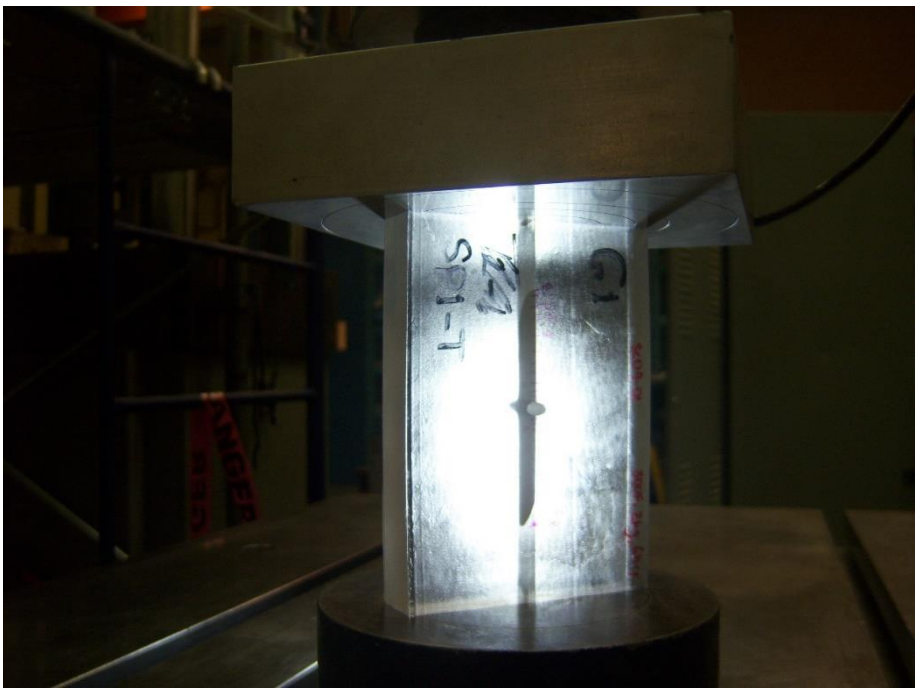

Figure 21: Photo taken at 180kN and 7.34mm compressive displacement respectively. Both arms are showing some tunneling at both ends with a 42mm extension for the both arms of the fracture. This is the ultimate load point as it is the maximum load the specimen was subjected to; thus, the fracture maximum extension is the measurements at this point.

Figure 22: Left, front face of rectangular specimen at 180kN uniaxial compression force. The center hole has deformed from a drilled circle to an oval from the large load it sustains. At the vertex of the center hole and the interface, some small gap is visible, this is considered the fracture aperture. On the right, there is a close view of the fracture geometry. The measurement for all specimens is taken at the maximum extension of the fracture and not an average.

Table 2: Specimen SC04-01 results typical of thin specimens. The results come from calculations performed on the raw data from the compression frame along with geometry of the specimen. The fracture length is taken from the marks taken at the load measurements where the above photos were taken.

UPPER

| Load (kN) | Length (mm) | dA (mm^2) | dU (J) | G | Ki (MPa*m^1/2) |
|---|---|---|---|---|---|
| 30 | 1 | 22 | 5.260458 | 0.239112 | 0.02445 |
| 50 | 3 | 66 | 14.43698 | 0.218742 | 0.023385 |
| 70 | 6 | 132 | 28.52157 | 0.216073 | 0.023242 |
| 100 | 10 | 220 | 58.00959 | 0.26368 | 0.025675 |
| 115 | 14 | 308 | 78.1341 | 0.253682 | 0.025183 |
| 130 | 18 | 396 | 102.6519 | 0.259222 | 0.025457 |
| 140 | 24 | 528 | 122.3808 | 0.231782 | 0.024072 |
| 150 | 31 | 682 | 145.2622 | 0.212994 | 0.023076 |
| 167 | 36 | 792 | 190.2651 | 0.240234 | 0.024507 |
| 175 | 40 | 880 | 215.2103 | 0.244557 | 0.024726 |
| 180 | 42 | 924 | 232.2102 | 0.25131 | 0.025065 |
| 118.75 | 15 | 330 | 83.54729 | 0.253174 | 0.025158 |

LOWER

| Load (kN) | Length (mm) | dA (mm^2) | dU (J) | G | Ki (MPa*m^1/2) |
|---|---|---|---|---|---|
| 30 | 2 | 44 | 5.260458 | 0.119556 | 0.017288 |
| 50 | 3 | 66 | 14.43698 | 0.218742 | 0.023385 |
| 70 | 5 | 110 | 28.52157 | 0.259287 | 0.02546 |
| 100 | 9 | 198 | 58.00959 | 0.292978 | 0.027064 |
| 115 | 12 | 264 | 78.1341 | 0.295962 | 0.027201 |
| 130 | 16 | 352 | 102.6519 | 0.291625 | 0.027001 |
| 140 | 20 | 440 | 122.3808 | 0.278138 | 0.026369 |
| 150 | 28 | 616 | 145.2622 | 0.235815 | 0.02428 |
| 167 | 33 | 726 | 190.2651 | 0.262073 | 0.025597 |
| 175 | 37 | 814 | 215.2103 | 0.264386 | 0.025709 |
| 180 | 42 | 924 | 232.2102 | 0.25131 | 0.025065 |
| 127.5 | 15 | 330 | 98.04018 | 0.297091 | 0.027253 |

**Results**

Two approaches were used to analyze the results from the proposed compressive test: The ultimate point approach and the mid-point approach.

**Ultimate load approach** is analysing the results based on the maximum load point. Table 3 summarizes the data from all specimens tested using the compressive proposed test and its corresponding figure 23.

Table 3: Summary of ultimate load points for all specimen tested under compression

| | Ki (MPa m½) | | | | |
|---|---|---|---|---|---|
| Scenario | Ave | StDv | Cov | Length (mm) | Load (kN) |
| 0 | 2.8111 | 0.3089 | 11% | 5.8 | 144.0 |
| 1 | 0.0145 | 0.0015 | 10% | 29.7 | 55.6 |
| 2 | 0.0160 | 0.0024 | 15% | 25.2 | 54.1 |
| 3 | 0.0139 | 0.0020 | 14% | 31.7 | 55.8 |
| 4 | 0.0234 | 0.0027 | 11% | 29.3 | 143.7 |
| 5 | 0.0217 | 0.0033 | 15% | 29.6 | 136.0 |
| 6 | 0.0212 | 0.0024 | 11% | 29.3 | 143.3 |
| 7 | 0.0214 | 0.0024 | 11% | 19.8 | 120.8 |
| 8 | 0.0213 | 0.0025 | 12% | 20.3 | 117.3 |
| 9 | 0.0239 | 0.0032 | 13% | 17.8 | 118.5 |

Figure 23: Range of results from ultimate load point approach for each scenario tested under the compression proposed test.

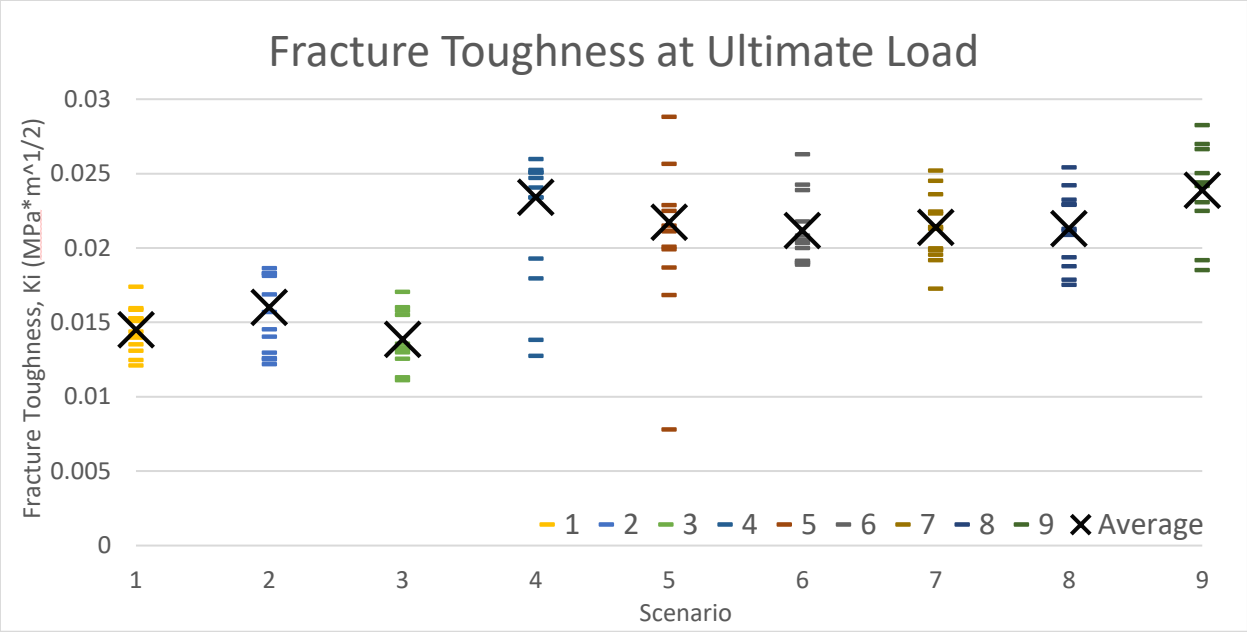


The tables hereafter consist of the ultimate point data from each arm of each specimen. Table 4 summarizes the intact solid specimen. Tables 5, 6 and 7, summarizes the SC01, SC02, and SC03, respectively. Tables 8, 9 and 10, summarizes the data corresponding to SC04, SC05, and SC06.Finally, tables 11, 12, and 13 summarize SC07, SC08, and SC09.

Table 4: Summary of ultimate load points for solid specimen of 24 mm (1") tested under compression. This provided a benchmark for the intact PMMA fracture toughness.

| | | **Load (kN)** | **Length (mm)** | **dA (mm^2)** | **dU (J)** | **G** | **Ki (MPa*m^1/2)** |
|---|---|---|---|---|---|---|---|
| SC00-01 | up | 150.0 | 8 | 176 | 427.8883 | 2.431183 | 2.465352 |
| | low | 150.0 | 7 | 154 | 427.8883 | 2.778495 | 2.635572 |
| SC00-02 | up | 138.0 | 4 | 88 | 332.2804 | 3.775914 | 3.072423 |
| | low | 138.0 | 4 | 88 | 331.9835 | 3.77254 | 3.07105 |
| | **Average** | **144.0** | **5.8** | **126.5** | **380.0** | **3.2** | **2.8** |
| | **std. dev.** | **6.928203** | **2.061553** | **45.35416** | **55.28505** | **0.689876** | **0.308878** |
| | **cov** | **0.048113** | **0.358531** | **0.358531** | **0.145483** | **0.216294** | **0.109878** |

Table 5: Summary of ultimate load points for thin 12 mm (1/2") specimen tested under compression. Scenario 1 consists of 7 specimens annealed for 6 hours under 1kg or 6kPa at 149˚C (300˚F).

| | | Load (kN) | Length (mm) | dA (mm^2) | dU (J) | G | Ki (MPa*m^1/2) |
|---|---|---|---|---|---|---|---|
| SC01-01 | up | 52 | 34 | 374 | 25.67328 | 0.068645 | 0.0131 |
| | low | 52 | 25 | 275 | 25.67328 | 0.093357 | 0.015277 |
| SC01-02 | up | | | | | | |
| | low | 58 | 30 | 300 | 27.33396 | 0.091113 | 0.015092 |
| SC01-03 | up | 58.5 | 36 | 360 | 29.82119 | 0.082837 | 0.014391 |
| | low | 58.5 | 32 | 320 | 29.82119 | 0.093191 | 0.015264 |
| SC01-04 | up | 56.4 | 30 | 360 | 28.13686 | 0.078158 | 0.013978 |
| | low | 56.4 | 23 | 276 | 28.13686 | 0.101945 | 0.015964 |
| SC01-05 | up | 53.9 | 35 | 420 | 26.12549 | 0.062204 | 0.01247 |
| | low | 53.9 | 18 | 216 | 26.12549 | 0.120951 | 0.017389 |
| SC01-06 | up | 54.3 | 38 | 456 | 26.7319 | 0.058623 | 0.012106 |
| | low | 54.3 | 28 | 336 | 26.7319 | 0.079559 | 0.014103 |
| SC01-07 | up | 57.1 | 33 | 396 | 28.93613 | 0.073071 | 0.013516 |
| | low | 57.1 | 24 | 288 | 28.93613 | 0.100473 | 0.015849 |
| | **Average** | **55.5692** | **29.6923** | **336.692** | **27.5526** | **0.08493** | **0.0145** |
| | **std. dev.** | **2.29905** | **5.85071** | **66.5975** | **1.5093** | **0.01756** | **0.0015** |
| | **cov** | **0.04137** | **0.19704** | **0.1978** | **0.05478** | **0.20673** | **0.10358** |

Table 6: Summary of ultimate load points for thin 12 mm (1/2") specimen tested under compression. Scenario 2 consists of 6 specimens annealed for 6 hours under 2kg or 12kPa at 149˚C (300˚F).

| | | Load (kN) | Length (mm) | dA (mm^2) | dU (J) | G | Ki (MPa*m^1/2) |
|---|---|---|---|---|---|---|---|
| SC02-01 | up | 40 | 13 | 130 | 17.3575 | 0.133519 | 0.01827 |
| | low | 55 | 26 | 260 | 29.67314 | 0.114127 | 0.016891 |
| SC02-02 | up | 55.8 | 32 | 352 | 20.95805 | 0.05954 | 0.0122 |
| | low | 55.8 | 30 | 330 | 20.95805 | 0.063509 | 0.012601 |
| SC02-03 | up | 56 | 28 | 336 | 28.39927 | 0.084522 | 0.014536 |
| | low | 56 | 24 | 288 | 28.39927 | 0.098609 | 0.015701 |
| SC02-04 | up | 55 | 34 | 408 | 27.41658 | 0.067197 | 0.012961 |
| | low | 55 | 17 | 204 | 27.41658 | 0.134395 | 0.01833 |
| SC02-05 | up | 55 | 34 | 374 | 23.42506 | 0.062634 | 0.012513 |
| | low | 55 | 27 | 297 | 23.42506 | 0.078872 | 0.014042 |
| SC02-06 | up | 55 | 19 | 209 | 27.50433 | 0.1316 | 0.018138 |
| | low | 55 | 18 | 198 | 27.50433 | 0.138911 | 0.018635 |
| | **Average** | **54.05** | **25.1667** | **282.167** | **25.2031** | **0.09729** | **0.016** |
| | **std. dev.** | **4.44614** | **7.03024** | **83.5451** | **3.86969** | **0.03171** | **0.00237** |
| | **cov** | **0.08226** | **0.27935** | **0.29608** | **0.15354** | **0.32592** | **0.14781** |

Table 7: Summary of ultimate load points for thin 12 mm (1/2") specimen tested under compression. Scenario 1 consists of 6 specimens annealed for 6 hours under 4kg or 24kPa at 149˚C (300˚F).

| | | Load (kN) | Length (mm) | dA (mm^2) | dU (J) | G | Ki (MPa*m^1/2) |
|---|---|---|---|---|---|---|---|
| SC03-01 | up | 54.5 | 42 | 462 | 22.87353 | 0.04951 | 0.011125 |
| | low | 54.5 | 33 | 363 | 22.87353 | 0.063012 | 0.012551 |
| SC03-02 | up | 51 | 40 | 480 | 24.5656 | 0.051178 | 0.011311 |
| | low | | | | | | |
| SC03-03 | up | 53 | 34 | 374 | 25.93252 | 0.069338 | 0.013166 |
| | low | 53 | 32 | 352 | 25.93252 | 0.073672 | 0.013571 |
| SC03-04 | up | 53 | 33 | 363 | 25.6032 | 0.070532 | 0.013279 |
| | low | 53 | 20 | 220 | 25.6032 | 0.116378 | 0.017057 |
| SC03-05 | up | 66 | 29 | 348 | 33.45711 | 0.096141 | 0.015503 |
| | low | 66 | 28 | 336 | 33.45711 | 0.099575 | 0.015778 |
| SC03-06 | up | 55 | 35 | 385 | 25.98731 | 0.0675 | 0.01299 |
| | low | 55 | 23 | 253 | 25.98731 | 0.102717 | 0.016025 |
| | **Average** | **55.8182** | **31.7273** | **357.818** | **26.5703** | **0.07814** | **0.01385** |
| | **std. dev.** | **5.16852** | **6.54356** | **75.7784** | **3.5996** | **0.02212** | **0.00197** |
| | **cov** | **0.0926** | **0.20624** | **0.21178** | **0.13547** | **0.2831** | **0.1419** |

Table 8: Summary of ultimate load points for thick 24 mm (1") specimen tested under compression. Scenario 4 consists of 6 specimens annealed for 6 hours under 2kg or 6kPa at 149˚C (300˚F).

| | | Load (kN) | Length (mm) | dA (mm^2) | dU (J) | G | Ki (MPa*m^1/2) |
|---|---|---|---|---|---|---|---|
| SC04-01 | up | 180 | 42 | 924 | 232.21018 | 0.2513097 | 0.0250654 |
| | low | 180 | 42 | 924 | 232.21018 | 0.2513097 | 0.0250654 |
| SC04-02 | up | 120 | 34 | 782 | 50.943064 | 0.0651446 | 0.0127617 |
| | low | 120 | 29 | 667 | 50.943064 | 0.0763764 | 0.0138181 |
| SC04-03 | up | 150 | 24 | 528 | 142.57043 | 0.2700198 | 0.0259817 |
| | low | 150 | 28 | 616 | 142.57043 | 0.2314455 | 0.0240544 |
| SC04-04 | up | 149 | 23 | 529 | 134.82003 | 0.2548583 | 0.0252417 |
| | low | 149 | 24 | 552 | 134.82003 | 0.2442392 | 0.0247103 |
| SC04-05 | up | 143 | 25 | 550 | 120.41629 | 0.2189387 | 0.0233954 |
| | low | 143 | 25 | 550 | 120.41629 | 0.2189387 | 0.0233954 |
| SC04-06 | up | 120 | 30 | 660 | 85.196377 | 0.1290854 | 0.0179642 |
| | low | 120 | 26 | 572 | 85.196377 | 0.1489447 | 0.0192967 |
| | **Average** | **143.6667** | **29.33333** | **654.5** | **127.6927** | **0.196718** | **0.023417** |
| | **std. dev.** | **21.35983** | **6.678777** | **145.8801** | **58.69093** | **0.072498** | **0.002669** |
| | **cov** | **0.148676** | **0.227686** | **0.222888** | **0.459626** | **0.368539** | **0.113994** |

Table 9: Summary of ultimate load points for thick 24 mm (1") specimen tested under compression. Scenario 5 consists of 6 specimens annealed for 6 hours under 4kg or 12kPa at 149˚C (300˚F).

| | | **Load (kN)** | **Length (mm)** | **dA (mm^2)** | **dU (J)** | **G** | **Ki (MPa*m^1/2)** |
|---|---|---|---|---|---|---|---|
| SC05-01 | up | 140 | 34 | 782 | 109.35534 | 0.1398406 | 0.0186976 |
| | low | 140 | 30 | 690 | 109.35534 | 0.158486 | 0.0199051 |
| SC05-02 | up | 120 | 34 | 748 | 84.73698 | 0.1132847 | 0.0168289 |
| | low | 50 | 27 | 594 | 14.48445 | 0.0243846 | 0.0078078 |
| SC05-03 | up | 150 | 30 | 660 | 138.12929 | 0.2092868 | 0.0228739 |
| | low | 150 | 31 | 682 | 138.12929 | 0.2025356 | 0.022502 |
| SC05-04 | up | 140 | 32 | 736 | 118.89867 | 0.1615471 | 0.0200965 |
| | low | 140 | 29 | 667 | 118.89867 | 0.1782589 | 0.0211104 |
| SC05-05 | up | 150 | 33 | 726 | 130.11666 | 0.179224 | 0.0211674 |
| | low | 150 | 32 | 704 | 130.11666 | 0.1848248 | 0.0214956 |
| SC05-06 | up | 151 | 24 | 528 | 138.91146 | 0.2630899 | 0.0256461 |
| | low | 151 | 19 | 418 | 138.91146 | 0.3323241 | 0.0288238 |
| | **Average** | **136** | **29.58333** | **661.25** | **114.1704** | **0.178924** | **0.021741** |
| | **std. dev.** | **28.52431** | **4.420167** | **102.8919** | **35.38819** | **0.075419** | **0.003279** |
| | **cov** | **0.209738** | **0.149414** | **0.155602** | **0.309959** | **0.421515** | **0.150832** |

Table 10: Summary of ultimate load points for thick 24 mm (1") specimen tested under compression. Scenario 6 consists of 6 specimens annealed for 6 hours under 8kg or 24kPa at 149˚C (300˚F).

| | | **Load (kN)** | **Length (mm)** | **dA (mm^2)** | **dU (J)** | **G** | **Ki (MPa*m^1/2)** |
|---|---|---|---|---|---|---|---|
| SC06-01 | up | 130 | 30 | 690 | 98.49431 | 0.1427454 | 0.0188908 |
| | low | 149 | 30 | 690 | 99.555884 | 0.1442839 | 0.0189924 |
| SC06-02 | up | 140 | 35 | 770 | 112.90027 | 0.1466237 | 0.0191457 |
| | low | 140 | 31 | 682 | 112.90027 | 0.1655429 | 0.0203435 |
| SC06-03 | up | 150 | 23 | 552 | 126.11923 | 0.2284769 | 0.0238996 |
| | low | 150 | 19 | 456 | 126.11923 | 0.2765773 | 0.0262953 |
| SC06-04 | up | 130 | 32 | 704 | 102.12794 | 0.1450681 | 0.0190439 |
| | low | 130 | 29 | 638 | 102.12794 | 0.1600751 | 0.0200047 |
| SC06-05 | up | 150 | 31 | 713 | 135.33071 | 0.1898046 | 0.0217833 |
| | low | 150 | 25 | 575 | 135.33071 | 0.2353578 | 0.0242568 |
| SC06-06 | up | 150 | 34 | 782 | 131.82496 | 0.1685741 | 0.0205289 |
| | low | 150 | 33 | 759 | 131.82496 | 0.1736824 | 0.0208376 |
| | **Average** | **143.25** | **29.33333** | **667.5833** | **117.888** | **0.181401** | **0.021169** |
| | **std. dev.** | **8.81244** | **4.735424** | **97.28726** | **14.7438** | **0.043263** | **0.002426** |
| | **cov** | **0.061518** | **0.161435** | **0.145731** | **0.125066** | **0.238493** | **0.114605** |

Table 11: Summary of ultimate load points for thick 24 mm (1") specimen tested under compression. Scenario 7 consists of 6 specimens annealed for 12 hours under 8kg or 24kPa at 149˚C (300˚F).

| | | Load (kN) | Length (mm) | dA (mm^2) | dU (J) | G | Ki (MPa*m^1/2) |
|---|---|---|---|---|---|---|---|
| SC07-01 | up | 105 | 20 | 440 | 52.41902 | 0.119134 | 0.017258 |
| | low | 120 | 16 | 352 | 70.16701 | 0.199338 | 0.022324 |
| SC07-02 | up | 125 | 27 | 594 | 87.50387 | 0.147313 | 0.019191 |
| | low | 125 | 26 | 572 | 87.50387 | 0.152979 | 0.019556 |
| SC07-03 | up | 120 | 20 | 460 | 72.54587 | 0.157708 | 0.019856 |
| | low | 140 | 20 | 460 | 102.5282 | 0.222887 | 0.023605 |
| SC07-04 | up | 120 | 18 | 396 | 79.80544 | 0.201529 | 0.022446 |
| | low | 120 | 20 | 440 | 79.80544 | 0.181376 | 0.021294 |
| SC07-05 | up | 120 | 23 | 506 | 80.76385 | 0.159612 | 0.019976 |
| | low | 120 | 20 | 440 | 80.76385 | 0.183554 | 0.021422 |
| SC07-06 | up | 120 | 15 | 330 | 79.27385 | 0.240224 | 0.024506 |
| | low | 115 | 13 | 286 | 72.66985 | 0.25409 | 0.025204 |
| | **Average** | **120.8333** | **19.83333** | **439.6667** | **78.81251** | **0.184979** | **0.021386** |
| | **std. dev.** | **7.929615** | **4.130449** | **91.34882** | **11.95324** | **0.040369** | **0.002351** |
| | **cov** | **0.065624** | **0.208258** | **0.207768** | **0.151667** | **0.218234** | **0.109918** |

Table 12: Summary of ultimate load points for thick 24 mm (1") specimen tested under compression. Scenario 8 consists of 6 specimens annealed for 12 hours under 8kg or 24kPa at 149˚C (300˚F).

| | | Load (kN) | Length (mm) | dA (mm^2) | dU (J) | G | Ki (MPa*m^1/2) |
|---|---|---|---|---|---|---|---|
| SC08-01 | up | 120 | 25 | 550 | 82.58876 | 0.150161 | 0.019375 |
| | low | 120 | 16 | 352 | 82.58876 | 0.234627 | 0.024219 |
| SC08-02 | up | 110 | 21 | 441 | 76.91451 | 0.174409 | 0.020881 |
| | low | 110 | 26 | 546 | 76.91451 | 0.140869 | 0.018766 |
| SC08-03 | up | 110 | 14 | 308 | 66.57866 | 0.216164 | 0.023247 |
| | low | 107 | 11 | 242 | 62.57721 | 0.258583 | 0.025426 |
| SC08-04 | up | 120 | 27 | 621 | 76.3039 | 0.122873 | 0.017527 |
| | low | 120 | 26 | 598 | 76.3039 | 0.127598 | 0.01786 |
| SC08-05 | up | 125 | 22 | 484 | 87.72459 | 0.181249 | 0.021287 |
| | low | 125 | 19 | 418 | 87.72459 | 0.209867 | 0.022906 |
| SC08-06 | up | 120 | 20 | 440 | 78.81393 | 0.179123 | 0.021161 |
| | low | 120 | 17 | 374 | 78.81393 | 0.210732 | 0.022953 |
| | **Average** | **117.25** | **20.33333** | **447.8333** | **77.8206** | **0.183855** | **0.021301** |
| | **std. dev.** | **6.239537** | **5.158106** | **117.3471** | **7.438275** | **0.043265** | **0.002541** |
| | **cov** | **0.053216** | **0.253677** | **0.262033** | **0.095582** | **0.23532** | **0.119297** |

Table 13: Summary of ultimate load points for thick 24 mm (1") specimen tested under compression. Scenario 9 consists of 6 specimens annealed for 24 hours under 8kg or 24kPa at 149˚C (300˚F).

| | | Load (kN) | Length (mm) | dA (mm^2) | dU (J) | G | Ki (MPa*m^1/2) |
|---|---|---|---|---|---|---|---|
| SC09-01 | up | 120 | 29 | 667 | 91.50564 | 0.13719 | 0.01852 |
| | low | 120 | 27 | 621 | 91.50564 | 0.147352 | 0.019193 |
| SC09-02 | up | 120 | 17 | 357 | 89.52674 | 0.250775 | 0.025039 |
| | low | 120 | 15 | 315 | 89.52674 | 0.284212 | 0.026656 |
| SC09-03 | up | 120 | 11 | 242 | 77.2754 | 0.31932 | 0.028254 |
| | low | 115 | 11 | 242 | 70.52088 | 0.291409 | 0.026991 |
| SC09-04 | up | 140 | 42 | 882 | 24.14273 | 0.027373 | 0.008272 |
| | low | 140 | 35 | 735 | 24.14273 | 0.032847 | 0.009062 |
| SC09-05 | up | 120 | 20 | 420 | 84.94803 | 0.202257 | 0.022487 |
| | low | 120 | 19 | 399 | 84.94803 | 0.212902 | 0.023071 |
| SC09-06 | up | 120 | 16 | 352 | 82.28136 | 0.233754 | 0.024174 |
| | low | 110 | 13 | 286 | 68.14043 | 0.238253 | 0.024406 |
| **Average** | | **118.5** | **17.8** | **390.1** | **83.01789** | **0.231742** | **0.023879** |
| **std. dev.** | | **3.374743** | **6.178817** | **146.7624** | **8.480682** | **0.059328** | **0.003189** |
| **cov** | | **0.028479** | **0.347125** | **0.376217** | **0.102155** | **0.256006** | **0.133543** |

**Mid-point approach** is analysing the results based on the fracture length extension point of 15mm for the thin specimens and 20mm for the thick ones. Table 14 summarizes data from all annealed specimens tested using the compressive proposed test for the mid-point approach and figure 24 corresponds to this table.

Table 14: Summary of mid-point approach for all annealed specimen tested under compression

| | Ki (MPa m½) | | | | |
|---|---|---|---|---|---|
| Scenario | Ave | StDv | Cov | Length (mm) | Load (kN) |
| 1 | 0.0191 | 0.0012 | 6% | 15 | 52.0 |
| 2 | 0.0183 | 0.0014 | 8% | | 50.4 |
| 3 | 0.0188 | 0.0016 | 8% | | 51.8 |
| 4 | 0.0216 | 0.0061 | 28% | 20 | 121.5 |
| 5 | 0.0201 | 0.0059 | 29% | | 113.3 |
| 6 | 0.0191 | 0.0048 | 25% | | 109.4 |
| 7 | 0.0207 | 0.0018 | 8% | | 126.0 |
| 8 | 0.0201 | 0.0019 | 9% | | 116.5 |
| 9 | 0.0217 | 0.0019 | 9% | | 134.3 |

Figure 24: Range of results from mid-point approach for each with annealed scenario tested under the compression proposed test.

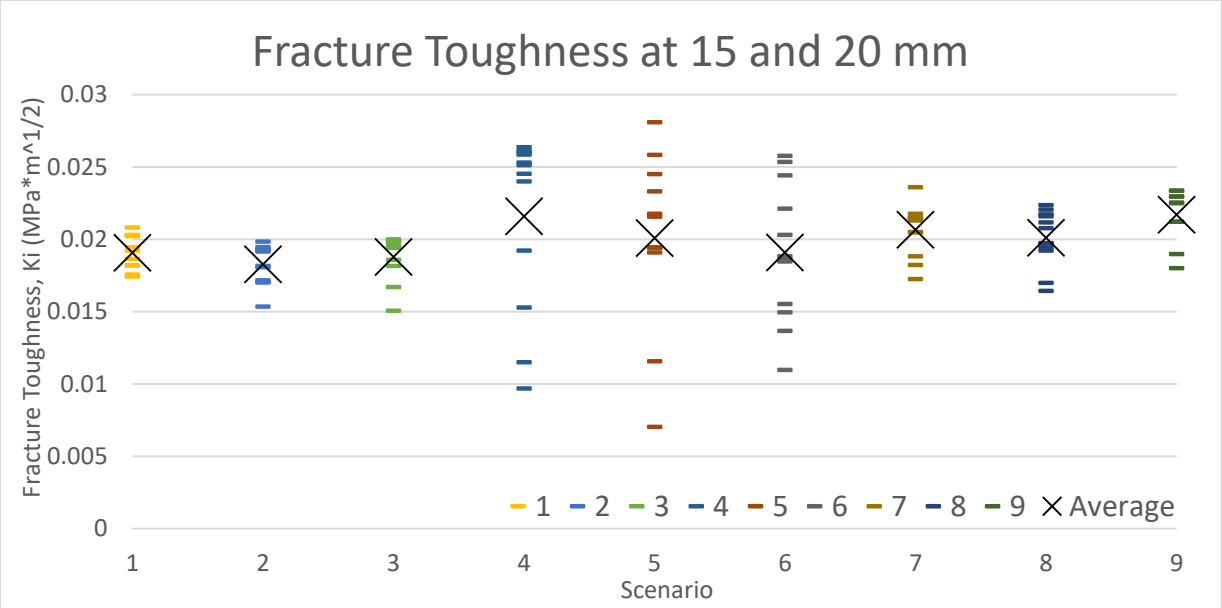


The tables hereafter summarize each scenario studied using the mid-point approach. Data from each arm of each specimen is shown in the following tables. Tables 15, 16 and 17, summarizes SC01, SC02, and SC03, respectively. Tables 18, 19 and 20, summarizes the data corresponding to SC04, SC05, and SC06. Finally, tables 21, 22, and 23 summarize SC07, SC08, and SC09.

Table 15: Summary of mid-point approach for thin 12 mm (1/2") specimen tested under compression. Scenario 1 consists of 7 specimens annealed for 6 hours under 1kg or 6kPa at 149˚C (300˚F).

| | | Load (kN) | Length (mm) | dA (mm^2) | dU (J) | G | Ki (MPa*m^1/2) |
|---|---|---|---|---|---|---|---|
| **SC01-01** | up | 44.333333 | 15 | 165 | 20.038585 | 0.121446 | 0.0174245 |
| | low | 44.5 | 15 | 165 | 20.138106 | 0.1220491 | 0.0174678 |
| **SC01-02** | up | | | | | | |
| | low | 54 | 15 | 150 | 24.688629 | 0.1645909 | 0.0202849 |
| **SC01-03** | up | 52 | 15 | 150 | 24.586204 | 0.163908 | 0.0202428 |
| | low | 54.25 | 15 | 150 | 26.020874 | 0.1734725 | 0.020825 |
| **SC01-04** | up | 54.333333 | 15 | 180 | 29.670586 | 0.1648366 | 0.0203 |
| | low | 55.5 | 15 | 180 | 27.20533 | 0.1511407 | 0.0194384 |
| **SC01-05** | up | 48.8 | 15 | 180 | 22.197447 | 0.1233191 | 0.0175584 |
| | low | 53 | 15 | 180 | 25.045715 | 0.1391429 | 0.0186509 |
| **SC01-06** | up | 51.428571 | 15 | 180 | 23.777753 | 0.1320986 | 0.0181727 |
| | low | 51.5 | 15 | 180 | 23.845296 | 0.1324739 | 0.0181985 |
| **SC01-07** | up | 58 | 15 | 180 | 29.435955 | 0.1635331 | 0.0202196 |
| | low | 54.46 | 15 | 180 | 26.58529 | 0.1476961 | 0.0192156 |
| | **average** | **52.0081** | **15** | **170.7692** | **24.86429** | **0.146131** | **0.019077** |
| | **std. dev.** | **4.037862** | **0** | **13.04578** | **3.012155** | **0.018767** | **0.001232** |
| | **cov** | **0.077639** | **0** | **0.076394** | **0.121144** | **0.128428** | **0.064596** |

Table 16: Summary of mid-point approach for thin 12 mm (1/2") specimen tested under compression. Scenario 2 consists of 6 specimens annealed for 6 hours under 2kg or 12kPa at 149˚C (300˚F).

| | | Load (kN) | Length (mm) | dA (mm^2) | dU (J) | G | Ki (MPa*m^1/2) |
|---|---|---|---|---|---|---|---|
| **SC02-01** | up | 43.333333 | 15 | 150 | 19.796972 | 0.1319798 | 0.0181645 |
| | low | 46.25 | 15 | 150 | 22.027913 | 0.1468528 | 0.0191607 |
| **SC02-02** | up | 52.8 | 15 | 165 | 19.15899 | 0.1161151 | 0.0170378 |
| | low | 53.5 | 15 | 165 | 19.451942 | 0.1178906 | 0.0171676 |
| **SC02-03** | up | 55 | 15 | 180 | 26.738243 | 0.1485458 | 0.0192708 |
| | low | 55.625 | 15 | 180 | 27.261678 | 0.1514538 | 0.0194585 |
| **SC02-04** | up | 45.625 | 15 | 180 | 20.866073 | 0.1159226 | 0.0170237 |
| | low | 54.333333 | 15 | 180 | 26.898771 | 0.1494376 | 0.0193286 |
| **SC02-05** | up | 42 | 15 | 165 | 15.568089 | 0.0943521 | 0.0153584 |
| | low | 52.333333 | 15 | 165 | 21.579657 | 0.1307858 | 0.0180822 |
| **SC02-06** | up | 51 | 15 | 165 | 24.605069 | 0.1491216 | 0.0193081 |
| | low | 53 | 15 | 165 | 26.00531 | 0.1576079 | 0.0198499 |
| | **average** | **50.4** | **15** | **167.5** | **22.49656** | **0.134172** | **0.018268** |
| | **std. dev.** | **4.773796** | **0** | **10.76611** | **3.768943** | **0.019535** | **0.001372** |
| | **cov** | **0.094718** | **0** | **0.064275** | **0.167534** | **0.145599** | **0.075117** |

Table 17: Summary of mid-point approach for thin 12 mm (1/2") specimen tested under compression. Scenario 3 consists of 6 specimens annealed for 6 hours under 3kg or 24 kPa at 149˚C (300˚F).

| | | Load (kN) | Length (mm) | dA (mm^2) | dU (J) | G | Ki (MPa*m^1/2) |
|---|---|---|---|---|---|---|---|
| **SC03-01** | up | 52.5 | 15 | 165 | 21.759855 | 0.1318779 | 0.0181575 |
| | low | 45.7 | 15 | 165 | 18.422779 | 0.1116532 | 0.0167073 |
| **SC03-02** | up | 38.333333 | 15 | 180 | 16.326267 | 0.0907015 | 0.0150583 |
| | low | | | | | | |
| **SC03-03** | up | 53 | 15 | 165 | 25.93252 | 0.1571668 | 0.0198221 |
| | low | 53.2 | 15 | 165 | 26.131799 | 0.1583745 | 0.0198981 |
| **SC03-04** | up | 49 | 15 | 165 | 22.791276 | 0.1381289 | 0.0185829 |
| | low | 52 | 15 | 165 | 24.825087 | 0.1504551 | 0.0193943 |
| **SC03-05** | up | 56.666667 | 15 | 180 | 27.334157 | 0.1518564 | 0.0194844 |
| | low | 59 | 15 | 180 | 28.816495 | 0.1600916 | 0.0200057 |
| **SC03-06** | up | 54.285714 | 15 | 165 | 25.180888 | 0.1526114 | 0.0195328 |
| | low | 56.4 | 15 | 165 | 25.987309 | 0.1574988 | 0.0198431 |
| | **average** | **51.82597** | **15** | **169.0909** | **23.95531** | **0.141856** | **0.018771** |
| | **std. dev.** | **5.772234** | **0** | **7.00649** | **3.808779** | **0.022398** | **0.001581** |
| | **cov** | **0.111377** | **0** | **0.041436** | **0.158995** | **0.157891** | **0.0842** |

Table 18: Summary of mid-point for thick 24 mm (1") specimen tested under compression. Scenario 4 consists of 6 specimens annealed for 6 hours under 2kg or 6kPa at 149˚C (300˚F).

| | | Load (kN) | Length (mm) | dA (mm^2) | dU (J) | G | Ki (MPa*m^1/2) |
|---|---|---|---|---|---|---|---|
| **SC04-01** | up | 137.5 | 20 | 440 | 117.75284 | 0.2676201 | 0.025866 |
| | low | 140 | 20 | 440 | 122.38079 | 0.2781382 | 0.0263694 |
| **SC04-02** | up | 75 | 20 | 460 | 17.274405 | 0.0375531 | 0.0096893 |
| | low | 87.5 | 20 | 460 | 24.306456 | 0.0528401 | 0.0114935 |
| **SC04-03** | up | 140 | 20 | 440 | 119.65969 | 0.2719538 | 0.0260746 |
| | low | 140 | 20 | 440 | 119.65969 | 0.2719538 | 0.0260746 |
| **SC04-04** | up | 140 | 20 | 460 | 116.11827 | 0.252431 | 0.0251213 |
| | low | 137 | 20 | 460 | 110.76585 | 0.2407953 | 0.0245355 |
| **SC04-05** | up | 139.25 | 20 | 440 | 112.72517 | 0.2561936 | 0.0253078 |
| | low | 133.33333 | 20 | 440 | 101.34713 | 0.2303344 | 0.0239966 |
| **SC04-06** | up | 83.333333 | 20 | 440 | 41.127484 | 0.0934716 | 0.0152866 |
| | low | 105 | 20 | 440 | 65.013909 | 0.1477589 | 0.0192197 |
| | **average** | **121.4931** | **20** | **446.6667** | **89.01097** | **0.200087** | **0.021586** |
| | **std. dev.** | **25.88003** | **0** | **9.847319** | **40.38727** | **0.091277** | **0.006113** |
| | **cov** | **0.213017** | **0** | **0.022046** | **0.453734** | **0.456186** | **0.28318** |

Table 19: Summary of mid-point for thick 24 mm (1") specimen tested under compression. Scenario 5 consists of 6 specimens annealed for 6 hours under 4kg or 12kPa at 149˚C (300˚F).

| | | Load (kN) | Length (mm) | dA (mm^2) | dU (J) | G | Ki (MPa*m^1/2) |
|---|---|---|---|---|---|---|---|
| **SC05-01** | up | 113.33333 | 20 | 460 | 67.118362 | 0.1459095 | 0.019099 |
| | low | 115 | 20 | 460 | 69.412105 | 0.1508959 | 0.0194227 |
| **SC05-02** | up | 63.333333 | 20 | 440 | 23.573278 | 0.0535756 | 0.0115732 |
| | low | 39.5 | 20 | 440 | 8.7087006 | 0.0197925 | 0.0070343 |
| **SC05-03** | up | 134 | 20 | 440 | 105.76668 | 0.2403788 | 0.0245142 |
| | low | 128.33333 | 20 | 440 | 95.610727 | 0.2172971 | 0.0233076 |
| **SC05-04** | up | 110 | 20 | 460 | 69.400554 | 0.1508708 | 0.019421 |
| | low | 110 | 20 | 460 | 69.400554 | 0.1508708 | 0.019421 |
| **SC05-05** | up | 124 | 20 | 440 | 81.919517 | 0.1861807 | 0.0215743 |
| | low | 125 | 20 | 440 | 83.388134 | 0.1895185 | 0.0217669 |
| **SC05-06** | up | 140 | 20 | 440 | 117.44146 | 0.2669124 | 0.0258318 |
| | low | 157 | 20 | 440 | 138.91146 | 0.3157079 | 0.0280939 |
| | **average** | **113.2917** | **20** | **446.6667** | **77.55429** | **0.173993** | **0.020088** |
| | **std. dev.** | **32.32819** | **0** | **9.847319** | **36.29749** | **0.083153** | **0.005856** |
| | **cov** | **0.285354** | **0** | **0.022046** | **0.468027** | **0.477911** | **0.291537** |

Table 20: Summary of mid-point for thick 24 mm (1") specimen tested under compression. Scenario 6 consists of 6 specimens annealed for 6 hours under 8kg or 24 kPa at 149˚C (300˚F).

| | | Load (kN) | Length (mm) | dA (mm^2) | dU (J) | G | Ki (MPa*m^1/2) |
|---|---|---|---|---|---|---|---|
| **SC06-01** | up | 86.666667 | 20 | 460 | 41.198135 | 0.0895612 | 0.0149634 |
| | low | 90 | 20 | 460 | 44.41945 | 0.096564 | 0.0155374 |
| **SC06-02** | up | 115 | 20 | 440 | 72.583468 | 0.1649624 | 0.0203078 |
| | low | 106.42857 | 20 | 440 | 61.059689 | 0.138772 | 0.0186261 |
| **SC06-03** | up | 148.5 | 20 | 480 | 123.48768 | 0.257266 | 0.0253607 |
| | low | 150.5 | 20 | 480 | 127.42599 | 0.2654708 | 0.0257619 |
| **SC06-04** | up | 60 | 20 | 440 | 21.203673 | 0.0481902 | 0.0109761 |
| | low | 75 | 20 | 440 | 32.884931 | 0.0747385 | 0.0136692 |
| **SC06-05** | up | 126 | 20 | 460 | 90.047531 | 0.1957555 | 0.0221221 |
| | low | 137.5 | 20 | 460 | 109.76856 | 0.2386273 | 0.0244247 |
| **SC06-06** | up | 107.5 | 20 | 460 | 62.792517 | 0.1365055 | 0.0184733 |
| | low | 110 | 20 | 460 | 65.256216 | 0.1418613 | 0.0188322 |
| | **average** | **109.4246** | **20** | **456.6667** | **71.01065** | **0.154023** | **0.019088** |
| | **std. dev.** | **28.35526** | **0** | **14.35481** | **35.07581** | **0.072444** | **0.004753** |
| | **cov** | **0.259131** | **0** | **0.031434** | **0.493951** | **0.470347** | **0.249008** |

Table 21: Summary of mid-point for thick 24 mm (1") specimen tested under compression. Scenario 7 consists of 6 specimens annealed for 12 hours under 8kg or 24 kPa at 149˚C (300˚F).

| | | Load (kN) | Length (mm) | dA (mm^2) | dU (J) | G | Ki (MPa*m^1/2) |
|---|---|---|---|---|---|---|---|
| SC07-01 | up | 105 | 20 | 440 | 52.419017 | 0.1191341 | 0.0172579 |
| | low | 140 | 20 | 440 | 73.790401 | 0.1677055 | 0.0204759 |
| SC07-02 | up | 106.66667 | 20 | 440 | 62.421397 | 0.1418668 | 0.0188326 |
| | low | 103.33333 | 20 | 440 | 58.532246 | 0.1330278 | 0.0182365 |
| SC07-03 | up | 140 | 24 | 552 | 102.52824 | 0.1857396 | 0.0215488 |
| | low | 140 | 20 | 460 | 102.52824 | 0.2228875 | 0.0236055 |
| SC07-04 | up | 126.66667 | 20 | 440 | 83.309618 | 0.18934 | 0.0217566 |
| | low | 120 | 20 | 440 | 79.805435 | 0.181376 | 0.0212941 |
| SC07-05 | up | 115 | 20 | 440 | 73.943713 | 0.1680539 | 0.0204972 |
| | low | 120 | 20 | 440 | 80.76385 | 0.1835542 | 0.0214216 |
| SC07-06 | up | 145 | 20 | 440 | 81.249353 | 0.1846576 | 0.0214859 |
| | low | 150 | 20 | 440 | 81.249353 | 0.1846576 | 0.0214859 |
| | **Average** | **125.9722** | **20.33333** | **451** | **77.71174** | **0.171833** | **0.020658** |
| | **std. dev.** | **16.64329** | **1.154701** | **32.32224** | **15.29327** | **0.028406** | **0.001755** |
| | **cov** | **0.132119** | **0.056789** | **0.071668** | **0.196795** | **0.165314** | **0.084931** |

Table 22: Summary of mid-point for thick 24 mm (1") specimen tested under compression. Scenario 8 consists of 6 specimens annealed for 24 hours under 8kg or 24 kPa at 149˚C (300˚F).

| | | **Load (kN)** | **Length (mm)** | **dA (mm^2)** | **dU (J)** | **G** | **Ki (MPa*m^1/2)** |
|---|---|---|---|---|---|---|---|
| SC08-01 | up | 107.5 | 20 | 440 | 65.037493 | 0.1478125 | 0.0192232 |
| | low | 133.33333 | 20 | 440 | 85.55615 | 0.1944458 | 0.022048 |
| SC08-02 | up | 106.66667 | 20 | 420 | 72.439233 | 0.1724744 | 0.020765 |
| | low | 100 | 20 | 420 | 63.570449 | 0.1513582 | 0.0194524 |
| SC08-03 | up | 119 | 20 | 440 | 68.446627 | 0.1555605 | 0.0197206 |
| | low | 138.5 | 20 | 440 | 68.446627 | 0.1555605 | 0.0197206 |
| SC08-04 | up | 96.666667 | 20 | 460 | 49.65611 | 0.1079481 | 0.0164277 |
| | low | 100 | 20 | 460 | 53.149388 | 0.1155421 | 0.0169957 |
| SC08-05 | up | 121.66667 | 20 | 440 | 82.971998 | 0.1885727 | 0.0217125 |
| | low | 126.66667 | 20 | 440 | 88.107502 | 0.2002443 | 0.0223743 |
| SC08-06 | up | 120 | 20 | 440 | 78.813928 | 0.1791226 | 0.0211614 |
| | low | 127.5 | 20 | 440 | 82.090837 | 0.1865701 | 0.0215969 |
| | **Average** | **116.4583** | **20** | **440** | **71.52386** | **0.162934** | **0.0201** |
| | **std. dev.** | **13.98847** | **0** | **12.06045** | **12.46345** | **0.029688** | **0.001906** |
| | **cov** | **0.120116** | **0** | **0.02741** | **0.174256** | **0.182207** | **0.094843** |

Table 23: Summary of mid-point for thick 24 mm (1") specimen tested under compression. Scenario 9 consists of 6 specimens annealed for 48 hours under 8kg or 24 kPa at 149˚C (300˚F).

| | | **Load (kN)** | **Length (mm)** | **dA (mm^2)** | **dU (J)** | **G** | **Ki (MPa*m^1/2)** |
|---|---|---|---|---|---|---|---|
| SC09-01 | up | 97.5 | 20 | 460 | 59.646176 | 0.1296656 | 0.0180046 |
| | low | 110 | 23 | 529 | 76.259515 | 0.1441579 | 0.0189841 |
| SC09-02 | up | 127.5 | 20 | 420 | 91.685818 | 0.2182996 | 0.0233613 |
| | low | 170 | 20 | 420 | 91.685818 | 0.2182996 | 0.0233613 |
| SC09-03 | up | 165 | 20 | 440 | 79.180605 | 0.1799559 | 0.0212106 |
| | low | 160 | 20 | 440 | 79.180605 | 0.1799559 | 0.0212106 |
| SC09-04 | up | 118 | 20 | 420 | 24.142733 | 0.0574827 | 0.0119878 |
| | low | 122.69231 | 20 | 420 | 24.142733 | 0.0574827 | 0.0119878 |
| SC09-05 | up | 120 | 20 | 420 | 84.948035 | 0.2022572 | 0.0224865 |
| | low | 125 | 20 | 420 | 85.423338 | 0.2033889 | 0.0225493 |
| SC09-06 | up | 140 | 20 | 440 | 92.848453 | 0.2110192 | 0.0229684 |
| | low | 127.5 | 20 | 440 | 92.848453 | 0.2110192 | 0.0229684 |
| | **Average** | **134.25** | **20.3** | **442.9** | **83.37068** | **0.189802** | **0.021711** |
| | **std. dev.** | **24.12496** | **0.948683** | **33.06038** | **10.39858** | **0.031195** | **0.001873** |
| | **cov** | **0.179702** | **0.046733** | **0.074645** | **0.124727** | **0.164354** | **0.086292** |

Comparison of results between the ultimate load approach and the mid-point approach as illustrated in figure 25. The ultimate point approach provides reliable results for the thick 24mm (1") specimens while the mid-point approach gives good results for the thin 12mm (1/2") specimens. This is because the data is truncated and this way the buckling effect is minimized.

Figure 25: Comparison of the results from the ultimate and mid-point approach for each scenario with annealed specimens tested under the compression proposed test.

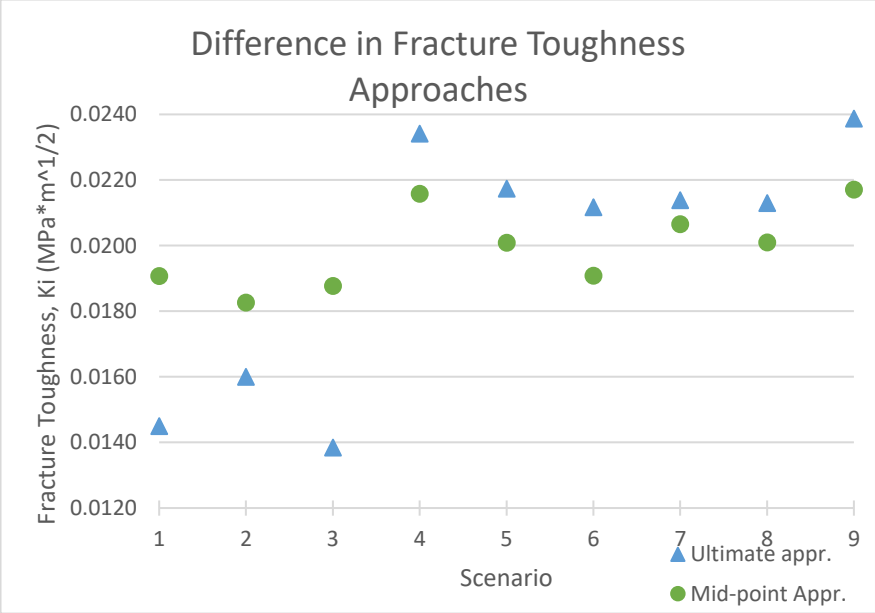


**Validation** of the uniaxial compressive test was carried out by testing 6 specimens prepared under the same conditions as those in scenario 9 and testing them using the Compact Tension (CT) standard testing methodology. The results are summarized in table 24. A comparison between the results of the solid intact specimens, scenario 9 tested under the proposed test and scenario 9 tested using the standard test can be seen in figure 26.

Table 24: Summary of validation assessment using thick 24 mm (1") specimen tested under standard CT methodology. Scenario 9CT consists of 6 specimens annealed for 48 hours under 8kg or 24 kPa at 149˚C (300˚F).

| | **Displ. (mm)** | **Load (kN)** | **Length (cm)** | **a/W** | **f(a/W)** | **Ki (MPa*m^1/2)** |
|---|---|---|---|---|---|---|
| SC09-01CT | 0.33 | 0.94 | 5.3 | 0.473214 | 8.96 | 0.990816 |
| SC09-02CT | 0.52 | 1.37 | 5.1 | 0.455357 | 8.46 | 1.385294 |
| SC09-03CT | 0.42 | 0.58 | 6.0 | 0.535714 | 10.63 | 0.736906 |
| SC09-04CT | 0.3 | 0.89 | 6.1 | 0.544643 | 11.17 | 1.188213 |
| SC09-05CT | 0.53 | 0.98 | 5.2 | 0.464286 | 11.19 | 1.310712 |
| SC09-06CT | 0.61 | 0.95 | 5.7 | 0.508929 | 9.81 | 1.113893 |
| **Average** | **0.451667** | **0.951667** | **5.566667** | **0.497024** | **10.03667** | **1.120972** |
| **std. dev.** | **0.122216** | **0.252144** | **0.427395** | **0.03816** | **1.154395** | **0.234472** |
| **cov** | **0.270588** | **0.26495** | **0.076778** | **0.076778** | **0.115018** | **0.209168** |

Figure 26: Comparison of the results between the intact specimen, the 9CT approach and an average of the fracture toughness of both approaches for scenario 9 tested under the compression proposed test.

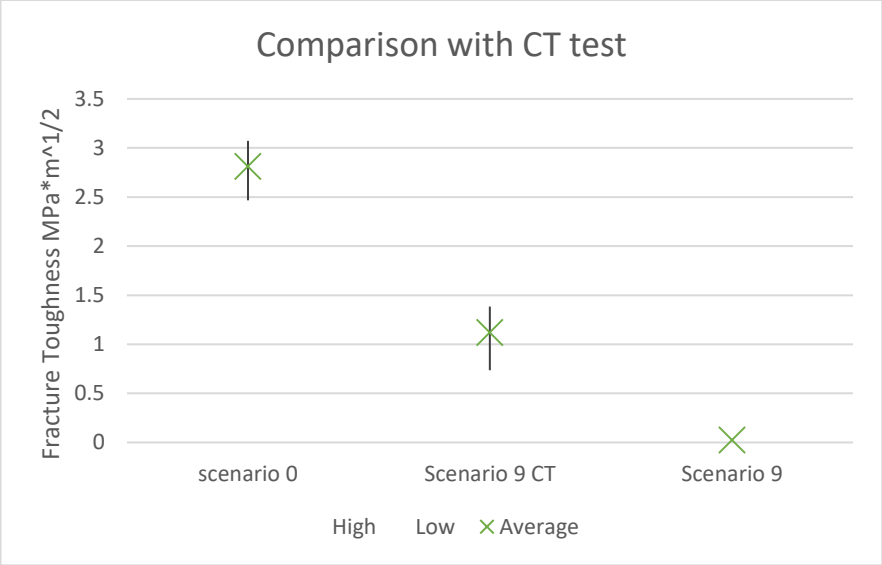


**Euler's calculation**

This was calculated using MathCAD

PMMA Properties

$E := 2.5GPa$

$rho := 1190\frac{kg}{m^3}$

Geometry of the specimen

$Length := 6in = 0.152m$

$Width := 4in = 0.102m$

$Base := 2in = 0.051m$

$LengthE := \frac{Length}{2} = 0.076m$

$HeigthA := \frac{1}{2}in = 0.013m$

$HeigthB := 1in = 0.025m$

$InertiaA := \frac{\left(Base \cdot HeigthA^3\right)}{12} = 8.671\times 10^{-9} m^4$

$InertiaB := \frac{\left(Base \cdot HeigthB^3\right)}{12} = 6.937\times 10^{-8} m^4$

$StressA := \frac{\left(\pi^2 \cdot E \cdot InertiaA\right)}{LengthE^2} = 3.685\times 10^4 N$

$StressB := \frac{\left(\pi^2 \cdot E \cdot InertiaB\right)}{LengthE^2} = 2.948\times 10^5 N$

$StressA = 3.685\times 10^4 N$

$StressB = 2.948\times 10^5 N$

# Appendix B: Conference Publication ARMA 2016[1]

[1] The contents of this appendix have been incorporated within a conference proceeding that was published by the American Rock Mechanics Association (ARMA) on its 50th Symposium.Gomez Rodriguez, D. M. ., Dusseault, M. B., & Gracie, R. (2016). "Cohesion and Fracturing in a Transparent Jointed Rock Analogue". *50th US Rock Mechanics / Geomechanics Symposium*.

# ARMA 16-418: Cohesion and Fracturing in a Transparent Jointed Rock Analogue

Gomez Rodriguez, D.M., Dusseault, M.B. and Gracie, R.

*University of Waterloo, Waterloo, Ontario, Canada*

**OVERVIEW:** A method to produce bonded surfaces with specific strengths to simulate joint cohesion and an experimental technique to measure the incremental fracture toughness were developed. PMMA was used as an analogue material to study cohesion of natural fractures because it has the ability to thermally bond, i.e., self-bond under high temperatures and stresses. Two PMMA blocks were fused along their long edges to form a bonded interface. Six different scenarios were studied using samples of two thickness, 12.7 mm and 25.4 mm (0.5 in and 1 in), and three applied compressive thermal bonding stresses – 6, 12 and 24 kPa. A hole drilled in the middle of the interface served as the fracture initiation point. A displacement controlled fracture toughness test was performed, where the sample is loaded by a compressive stress applied in the direction parallel to the cohesive interface. A visible stable fracture propagating towards both ends of the specimen is produced. The rate of displacement, load, and fracture growth were recorded. These data were used to determine the fracture toughness of the bonded interface.

## INTRODUCTION

Natural fracture (joint) cohesion plays an important role in rock mechanics; for example, small values of joint cohesion can significantly impact the results of slope and tunnel roof stability analyses. Natural fractures create complicated interactions with hydraulic fractures as implemented in the oil and gas industry to increase the rock mass permeability in the region surrounding the injection point. In fractured media, the hydraulic fracture influences a much larger volume of rock due to the shearing and distortions taking place in the rock mass (Dusseault 2015). This movement causes wedging (Mode I) and slip (Mode II) fracture among the solid matrix fragments. The amount of shearing and consequent shear dilation produced by the fluid injection is dependent on the cohesion level of the preexisting planes of weakness in the rock mass, as well as other mechanical properties of the rock mass. Cohesion is a parameter in Mohr–Coulomb theories of rock mass yielding/failure (Hossain et al., 2002). The aperture dilation of preexisting fractures during shear is also dependent on the roughness of the joint (Barton et al. 1985) and the shear displacements parallel to the joint walls. The higher the cohesion, the more energy the hydraulic fracture requires to open pre-existing or incipient fractures, therefore the smaller the stimulated volume

adjacent to the main fracture plane is likely to be. It is desirable to study these issues in a controlled laboratory setting.

The amount of energy required to open a sealed crack per unit of fracture area is called fracture toughness. This mechanical property is difficult to measure for brittle materials in experimental and field work (Bunger et al., 2004). In order to measure fracture toughness of brittle materials such as rock or ceramics, three-point tests are usually performed (Hooton et al., 1997). However, this process relies on the initiation of a crack under the central load along the tension side of the specimen and results are influenced by the size of initial imperfections. Similarly, a four point test is used for plastics and other materials (ASTM INTERNATIONAL, 2010), but issues of imperfection size and orientation on the bottom fiber remain important. Both of these tests develop unstable cracks that propagate at large velocities once the critical load is reached.

A different method to measure the fracture toughness of a bonded interface was developed by generating a stable fracture growth condition. The interface was created using polymethylmethacrylate (PMMA), a clear plastic. Two pieces of the same thickness were put under compression in an oven at 150ºC (300ºF) for 6 hours leading to the bonding of the surfaces and the creation of a single specimen with a plane of weakness. This bonded interface represents a useful analogue to partially cemented joints in naturally fractured rock masses.

**BACKGROUND**

Stresses are generated within a material subjected to loads that are distributed along its surfaces. The resulting stress distribution follows the geometry of the loaded section leading to local stress concentrations at imperfections, holes, and notches. Based on the dimensions of macroscopic imperfections such as an elliptical crack, a stress concentration factor can be calculated to determine the state of local stress around the opening tip. This is more challenging for planar fractures as the tip of the propagating crack is sharp and its aperture approaches zero. Therefore, the mathematically calculated stress concentration has a singularity at the tip of the fracture (Ashby et al., 2007, p. 168).

The stress intensity (K) is calculated based on the mode of fracture: tension (Mode I), sliding (Mode II), and tearing (Mode III). In this study only the Mode I stress intensity factor ($K_I$) was evaluated, because Modes II and III have a shear component which does not exist in the experimental setup described herein (Gdoutos, 1993, p. 16). Fracture toughness is defined as the critical value of the stress intensity at which a crack propagates. It indicates the disposition of a material to allow growth of a fracture in the presence of the imperfections that lead to local stress concentrations.

Researchers have used analogue materials such as milled rock blocks, borosilicate glass and PMMA to study cohesive fracture mechanics. For example, Jiefan et al. (1990) used marble blocks 104×80×6 mm (4×3×0.2 in) and subjected them to uniaxial compression along the width and thickness face of the sample. These slabs contained 20 mm long by 1 mm wide central slots inclined at different angles as fracture initiation flaws. Slots were either hollow or filled with a mortar to see the effect the filling had in the failure mechanism of the plate. The results improved understanding on how the samples failed by the development of fractures and shear planes but the analyses did not examine cohesion effects within the fracture and its fracture toughness. Additionally, their results were limited to surface observations during the loading phase due to the opaque nature of the material. To better address this issue, Sahouryeh et al. (2002) created two transparent resin cubes of 100 mm (3.9 in) per side with an initial circular slot in the center of 10 mm (0.4 in) in diameter inclined at 30º to the loading axis. A sandstone and a concrete sample of the same dimensions and characteristics were tested as well under biaxial compression. The results showed the difference in fracture growth for biaxial loading in real time within the sample, but the sample did not have an existing plane of weakness (a joint).

Tang et al., (2015) created 60 rock-like samples of transparent resin, mixed with some aggregates, of overall size 50×50×100 mm (2×2×4 in). The blocks contained mica inclusions placed at different angles as fracture initiation points. The samples were tested using displacement-controlled uniaxial compression and the fracture growth was studied. The stress intensity factor was calculated for Mode I fracture. However, the preexisting flaws (boundaries between particles and resin) are randomly oriented throughout the sample and they do not extend across the sample as a single plane. Similarly, Lee and Jeon (2011) used PMMA, gypsum, and granite as materials for their specimens. Blocks of 60×120×25 mm (2.4×4.7×0.9 in) were used for the PMMA and gypsum samples, and 60×120×30 mm (2.4×4.7×1.2 in) for the granite samples. All samples contained at least one horizontal crack on the 60×120 mm (2.4×4.7 in) face as a fracture initiation point. Some samples had an additional small fracture in the center located at 10 mm (0.4 in) from the horizontal crack and inclined at angles between 30º and 90º. The samples were loaded until either failure or fracture coalescence was achieved. This study was then compared to numerical simulations performed using bond breakage information (discrete element models, not fracture mechanics models). Similarly, Ayatollahi et al. (2015) studied PMMA samples shaped as a "v-notch stepped cottage" of 6 mm (0.2 in) in thickness. These samples were subjected to uniaxial compression forces and the results were studied using fracture mechanics and finite element analysis.

However, the fracture growth within the aforementioned experiments—except for Tang et al. (2015)—is based on a homogeneous medium containing an induced flaw as a fracture initiation point or a v-notch

as in the case of Ayatollahi et al. (2015). In the literature, some experimental work has been carried out using frictional forces within the initial flaw such as Park & Bobet (2010). Specimens of dimensions 203.2×101.6×30 mm (8×4×1.2 in) were created using gypsum with three closed flaws of 12.7 mm (0.5 in) in length. These flaws were in the center of the 203.2×101.6 mm (8×4 in) face and they extended across the sample normal to this face. Samples were uniaxially compressed with growth of the fracture initiated from the tips of the flaws until failure took place. Shearing events occurred along the length of the closed flaws, but the experiment did not consider the growth of the fracture within the artificially created closed flaw, and only surface measurements could be taken due to the use of opaque material.

Therefore, an alternative method was sought to produce controlled bonded surfaces of varying strengths that could represent variations in joint cohesion, as well as a stable fracture propagation testing method to allow for incremental fracture toughness calculations to assess cohesion homogeneity. PMMA samples were created with a linear bonded interface along the length of the material which represents a partially cemented joint. The transparent testing material allows for visual fracture propagation tracking during loading tests and thus allows measurement of the fracture toughness along the interface. Stable fracture growth was achieved by applying a uniaxial compression load parallel to the bonded (vertical) interface. A small central circular opening was used as the fracture initiation point, and the stable fracture growth length measured as loads were incrementally increased.

## METHODOLOGY

### *Specimen Preparation and Testing*

In this research, 37 rectangular samples were made from PMMA, a homogeneous transparent material with a bulk modulus (E) of 2500 MPa, Poisson ratio (ν) of 0.4, and a fracture toughness in tension ($K_{Ic}$) of 1.4 $MPa \cdot m^{1/2}$.

PMMA can self-bond under high temperatures and pressures — the thermal bonding effect (Washabaugh & Knauss, 1995). To determine the range of temperature, pressure, and cooking times that produce a cohesive bond of a certain strength, a small pilot test was conducted. Bonding occurred consistently when the temperature was between 150°C and 177°C (300-350°F). However, weaker bonds that were easily broken even with careful handling of the specimens occurred when bonds were formed at temperatures around 120°C (250°F). Specimen bonding was tested at a temperature of 150°C (300°F) for 1 to 8 hours, and a 6-hour time was eventually chosen for all 37 specimens, as it yielded consistent bonding of the interface. The compressive stress applied normal to the interface that was applied during cooking was also considered. It was found that there was no bonding if no stress was applied, and that larger stresses resulted in stronger cohesive bonding, so stress on the sample was used during bonding for a 6-hour

period at a constant 150ºC temperature and the stress value could be varied to achieve different degrees of interface cohesion.

Slabs of PMMA of two different thicknesses were used, 12.7 and 25.4 mm (0.5 and 1 in). These slabs were cut into rectangular prisms of dimensions 152×50.8 mm (6×2 in). Each piece was milled and ground with emery cloth grade 400 and 500 for a smooth surface on the longitudinal and thickness face—152 mm (6 in) by 25.4 or 12.7 mm (1 or 0.5 in) Pairs of plates were bonded making them into a test specimen as shown in Figure. The bonded side is identified by the arrow in the figure and the numbers identify each pair of prisms.

Figure 1: PMMA slab pieces of 12.7 mm (0.5 in) thick cut and milled at 152mm by 50.8mm (6 in by 2 in) and ready to be trimmed and subsequently bonded.

The bonded interface of two PMMA slabs was created through thermal bonding. The processed slabs were placed within a compression chamber between steel plates as seen in Figure 2 and placed in an oven at 150°C (300°F) for 6 hours. There were three applied stresses used: 6, 12 and 24 kPa. Table 1 summarizes the different scenarios considered in this study. Six (6) samples were tested for each scenario 2 through 6 and seven (7) samples for scenario 1. The name convention SC0X-0X refers to its cooking conditions and sample number.

Table 1: Summary of the different geometry and cooking scenarios considered in this study. The temperature and time was kept constant while the thickness of the sample and applied stress while cooking was increased twice by a factor of 2

| Scenario | Mass | Pressure | Thickness | Temp | Time |
|---|---|---|---|---|---|
| 1 | 1 kg | 6 kPa | 12.7mm ½ in | 149ºC 300ºF | 6 hrs |
| 2 | 2 kg | 12 kPa | | | |
| 3 | 4 kg | 24 kPa | | | |
| 4 | 2 kg | 6 kPa | 25.4mm 1 in | | |
| 5 | 4 kg | 12 kPa | | | |
| 6 | 8 kg | 24 kPa | | | |

To prevent buckling of the sample during the bonding process, two thick steel plates were used to hold the pieces in place. The PMMA prisms were carefully placed in parchment paper to prevent contact with the steel plates. This was placed flush against the bottom face of the steel plates such that the PMMA supports its own weight, preventing any stress transfer to the steel plates and to keep the top portion between the two plates. A square steel bar was placed in the clearance between the plates and directly on top of the PMMA pieces to apply a homogenously distributed stress. This steel bar was milled for both thicknesses to perfectly fit between the plates and avoid load transfer between the bar and the steel plates. On top of the bar a thin steel plate was placed such that the dead weight plate can balance on top of the square bar as shown in figure 2. The oven was then turned on and the sample was left to cook for 6 consecutive hours at 150°C (300°F).


Figure 2: Compression chamber within the oven to create thermal bonding. Stress is applied normal to the thickness of the sample by the dead weight. Temperature is held at 150°C (300°F) and it is confirmed by the interior thermostat for 6 hours. Above, 12.7 mm (0.5 in) thick sample scenario 1 being bonded at high temperature. Below, 24.5 mm (1 in) thick sample scenarios 4 (left) and 5 (right) cooling down after 6 hours of cooking.

After the samples had completed its cooking time, the oven was turned off and its doors were opened to slowly cool down the sample. This was done to prevent unbonding arising from differential thermoelastic shrinkage. Once the steel compression cell and the PMMA sample reached room temperature, the PMMA bonded sample was retrieved and catalogued for further refinements prior to testing. Once all samples of the same scenario were bonded, the samples were milled along the width and thickness face to ensure evenly distributed loading. This is the face where the uniaxial compression load is applied during testing. All the samples of the same scenario were carefully milled to obtain similar final dimensions among them and among the other scenarios. Additionally, a circular opening of 6.35 mm (0.25 in) diameter was drilled at the center of the sample. This opening forced the fracture initiation point to be at the vertex of the interface and the perimeter of the circle. At this point the samples were ready to be tested in a uniaxial compression load frame.

The samples were tested using the MTS 810 frame for the 12.7 mm (0.5 in) thick and the MTS 322 frame for the 24.5 mm (1 in) thick. Additionally, scenario 2 was tested using both frame to ensure repeatability and compatibility of results. The MTS 810 (318.10) is a smaller frame with maximum load output of 100

kN whereas the 322 (322.31) is able to produce up to 250 kN. The thicker samples were expected to withstand the maximum output load of the MTS 810 machine and, hence, the MTS 322 was used to continue testing the thicker samples.

The same process was used when testing in both the MTS 810 and MTS 322 load frames. Each sample was measured for its external dimensions and positioned at the cylindrical base on the load frame parallel to the actuator as shown in Figure 3. The sample was placed so the interface was parallel to the loading direction. The actuator was then lowered using manual controls until just before touching the sample. Figure 4 shows sample SC03-04 at this point, ready to be tested in the loading frame MTS 810. The manual controls were turned off and the cylindrical safety barrier was secured around the sample. The displacement and load measurement were zeroed and the specimen loaded using a very small load (3 Pa) to secure the positioning of the sample. After this, the experiment is started by letting the load frame run in displacement controlled mode and the sample was compressed by at a rate of 0.01 mm/min (millimeter per minute). Displacement and forces were displayed as the experiment was running and they were recorded for data processing by the load frame. As the actuator was compressing the sample, the load increased and the fracture grew. At specific loads, marks were drawn on the sample surface showing the corresponding extension of the fracture at that given point and load. At these same point pictures were taken of the gradual fracture growth. The experiment was stopped when the load displacement curve displayed by the frame reached a maximum and the input load started to decline. Due to the slow displacement loading rate, the length of the test varied from 40 min to 80 min.

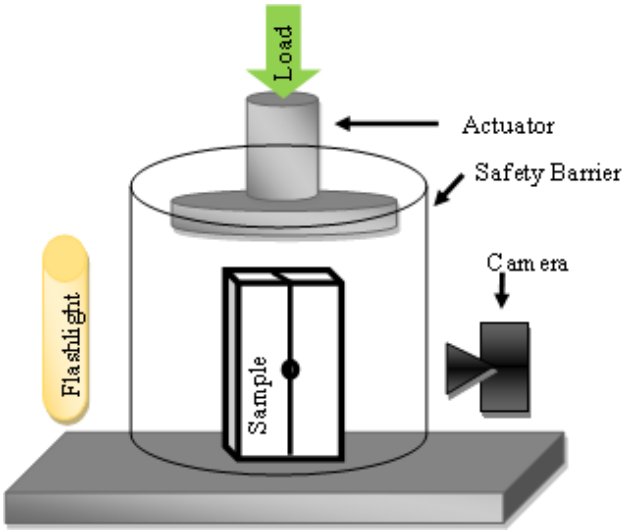


Figure 3: Schematic of test set up using both, MTS 810 and MTS 322, loading frames for all samples. The sample was place at an angle to the flashlight and the camera so that the light interference would show the fracture growth.

*Data acquisition and processing*

The bonded samples were tested using displacement rate control on the load frame to create stable fracture growth. During the procedure, the frame recorded the displacement and load applied on the sample every 0.5 seconds. At the same time, visual observations, photographs, and surface markings were recorded at given loads. After the sample was retrieved from the testing frame. The surface markings along the interface were measured from the vertex of the circular opening along the interface. These measurements represent the fracture growth at the given load as indicated on each marking on the upper and lower arms of the fracture as shown in figure 4.

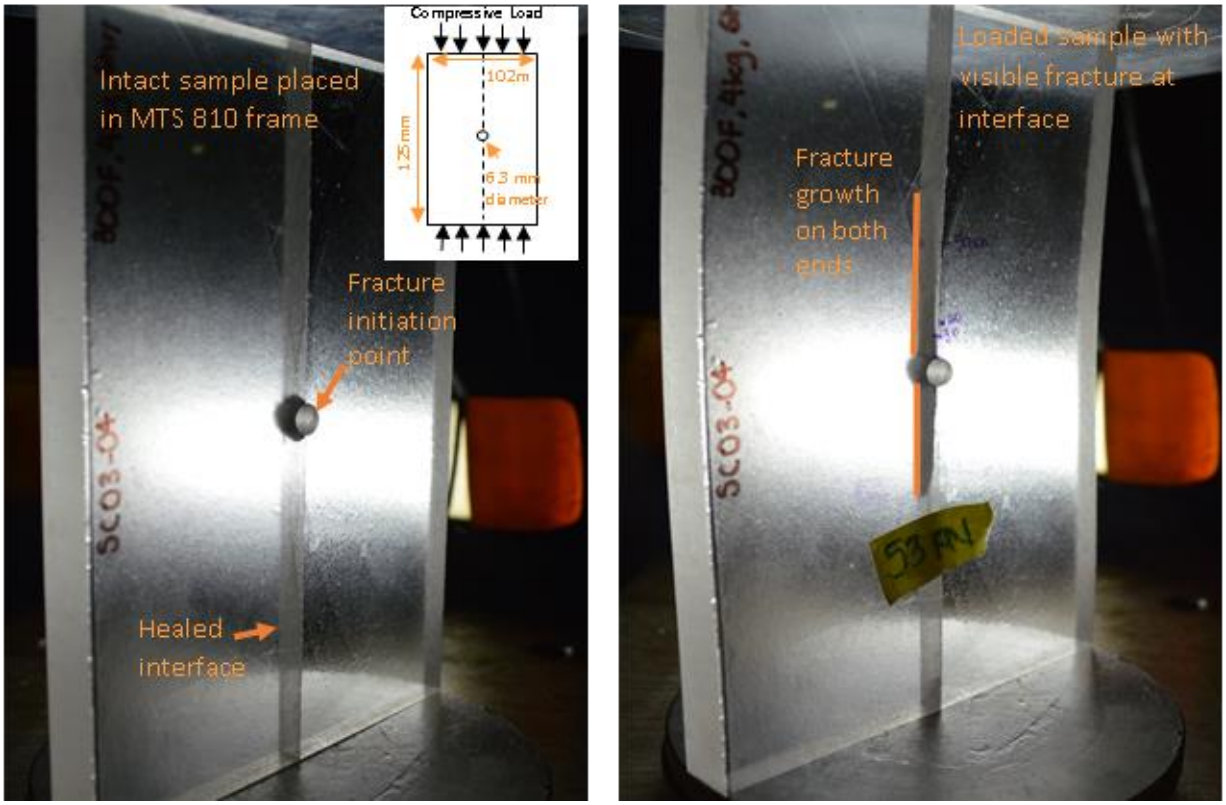


Figure 4: Left, prepared sample SC03-04, milled on all sides ends and a 6.3mm (0.25 in) diameter hole in the center to serve as fracture initiation point ready to be tested. Right, sample SC03-04 tested exhibiting buckling due to its geometry. Fracture is visible at the interface extending on both directions—upper and lower fractures—from the circular opening.

The fracture toughness or level of cohesion of the interface of each sample was calculated using the recorded information. This was done using a potential energy approach as defined for a brittle material by Griffith's theory

$$G = \frac{dU}{dA} \qquad (1)$$

where $G$ is the crack driving force, $dU$ is the energy realease in the experiment at some point, and $dA$ is the area of the crack opened at that same point (Gdoutos, 1993, p. 80). Additionally, the potential energy can be related to stress intensity factor for Mode I fracture of an in-plane stress by

$$G = \frac{K_I^2}{E} \qquad (2)$$

where $G$ is the potential energy or crack driving force, $E$ is the elastic modulus for plane stress of PMMA (2500MPa), and $K_I$ is the stress intensity value for Mode I fracture tensional cracks (Moës et al., 1999). Using (1) and (2), the stress intensity factor can be found as

$$K_I = \sqrt{E\left(\frac{dU}{dA}\right)} \qquad (3)$$

From the data collected during the experiment, the increment in the internal energy released ($\Delta U$) was estimated as the area under the load-displacement curve and above the elastic unloading curve, as illustrated in Figure 5. The area under the load-displacement curve was calculated using the trapezoidal rule for each step increment as the step increments were small for each sample. The elastic unloading curve was not recorded for all tested samples; hence a bilinear approximation was estimated with the recorded information and applied to all samples. PMMA is a homogeneous material manufactured with constant properties. Therefore, the recorded unloading elastic curves were only slightly different among samples and these curves were used to approximate the unloading curve for all samples. The integral of the elastic unbounding curve was negligible for displacements less than 1.5 mm, therefore the area bounded by the load displacement curve and elastic unbounding curve was used for loads which resulted from a compression greater than 1.5 mm. The area under the unloading elastic curve was subtracted from the area under the load-displacement curve of each sample if the sample had compressed more than 1.5 mm. The subtracted area was estimated by the integral of the linear curve evaluated between 1.5 mm and the point of interest, the corresponding displacement for a given load. The fractured area ($\Delta A$) was measured directly from the observed fracture. Assuming a perfectly square fracture tip across the sample thickness, the length of the fracture was multiplied by the thickness. Each $\Delta A$ has a given load associated with it. Using this associated load, the $\Delta U$ was retrieved and equation 1 was applied giving the crack driving force, $G$. Each sample has two values of fracture toughness for the recorded points corresponding to the upper (from the circular opening to the actuator) and lower (from the circular opening to the base of the sample) arms of the fracture, hence the $\Delta U$ was divided by 2 to represent both halves of the sample when calculating $K_I$.

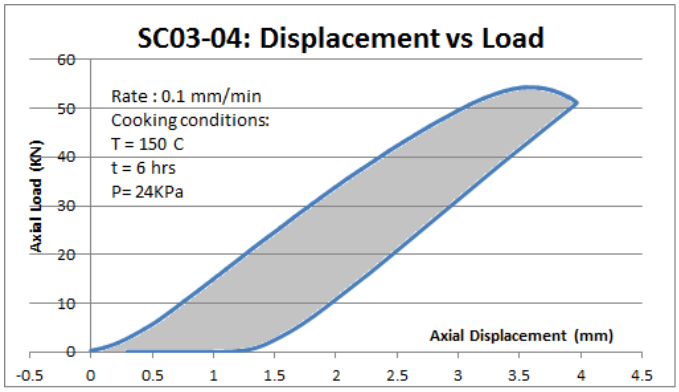


Figure 5: Load path displacement vs. load of sample SC03-04. The graph is a direct output from the load frame and the area under the curve (grey area) represents the energy release coefficient ($\Delta U$) used to calculate the fracture toughness of the interface.

**RESULTS**

The results were categorized by the different scenarios following the order shown in Table . They were compared to results of samples of the same thickness and same cooking conditions.

Scenarios 1, 2, and 3 used 12.7 mm thick PMMA slabs and were tested in the MTS 810 load frame. The fracture toughness for each arm of the fracture in one sample was considered to be, at first, at the ultimate load. This was at the maximum point on the displacement vs. load curve as the testing was ended soon after the peak was reached.

Scenario 1 specimens has the lowest curing load and resulted in an average ultimate loading of 55.6 kN, the average length of the fracture was 30.6 mm, and a toughness 0.014 MPa·m$^{1/2}$ with a standard deviation of 0.001 MPa·m$^{1/2}$ – coefficient of variability of 10%. Similarly, scenarios 2 and 3 had average loadings of 54.0 and 55.8 kN, and the average length of the fractures were 26.5 and 33.0 mm. The fracture toughness was 0.015 MPa·m$^{1/2}$ and 0.014 MPa·m$^{1/2}$ with a standard deviation of 0.002 MPa·m$^{1/2}$ and 0.002 MPa·m$^{1/2}$ – coefficient of variability of 15% and 14% respectively. These results for scenario 2 were gathered from additional tests conducted using the MTS 322 load frame using the same geometry as scenarios 1 and 3. The tests were first carried out on the MTS 810, however there was a high coefficient of variability as a consequence of a slightly different geometry in the samples which led to additional tests. The 15% coefficient of variability in the new results confirms that the change in loading frame did not affect the validity of the results. Though the coefficient of variability was low, the different scenarios yielded similar results. Scenarios 1 and 3 yielded the same fracture toughness average.

Scenarios 4, 5, and 6, used 25.4 mm thick samples that were tested in the MTS 322 load frame. Scenario 4 used the lowest curing load (equal to the load used in scenario 1) and resulted in an average loading of 143.7 kN and fracture toughness of 0.021 MPa·m$^{1/2}$ with a standard deviation of 0.004 MPa·m$^{1/2}$ –

coefficient of variability of 22%. Scenarios 5 and 6 had average loadings of 136.0 and 143.3 kN and fracture toughness of 0.020 MPa·m$^{1/2}$ and 0.021 MPa·m$^{1/2}$ and a standard deviation of 0.005 and 0.003 MPa·m$^{1/2}$ – coefficient of variability of 26% and 13% - respectively. See Table 2 for the summary of results.

Table 2: Summary of results for all scenarios at ultimate load excluding samples that were deemed damaged. Scenarios 1, 2, and 3 are made of PMMA of 12.7 mm (0.5 in) thickness. Scenarios 4, 5, and 6 are made with PMMA of 25.4mm (1 in) thickness. Length is given in mm and the load in kPa.

| | **Ki (MPa m$^{1/2}$)** | | | | |
|---|---|---|---|---|---|
| **Scenario** | **Ave** | **St.Dv.** | **Cov** | **Length** | **Load** |
| 1 | 0.0143 | 0.0015 | 10% | 31.0 | 55.6 |
| 2 | 0.0149 | 0.0023 | 15% | 26.5 | 54.1 |
| 3 | 0.0136 | 0.0019 | 14% | 33.0 | 55.8 |
| 4 | 0.0214 | 0.0048 | 22% | 35.0 | 143.7 |
| 5 | 0.0203 | 0.0053 | 26% | 22.0 | 136.0 |
| 6 | 0.0208 | 0.0028 | 13% | 37.0 | 143.3 |

There is a large discrepancy in the results of the same cooking conditions but of different thicknesses and very similar values results from the scenarios of the same thickness; this can be seen in Figure6. The thinner samples yield lower results as they were influenced by buckling during testing; this was the effect of having long but thin geometry. Thus some of scenario 2 samples were made smaller with 127 mm (5 in) in length while the other characteristics were kept constant. The shorter samples exhibited buckling during testing and thus the geometry was changed to samples twice as thick. Scenarios 4, 5, and 6 did not exhibit buckling and withstood a much larger load as shown in Figure7.

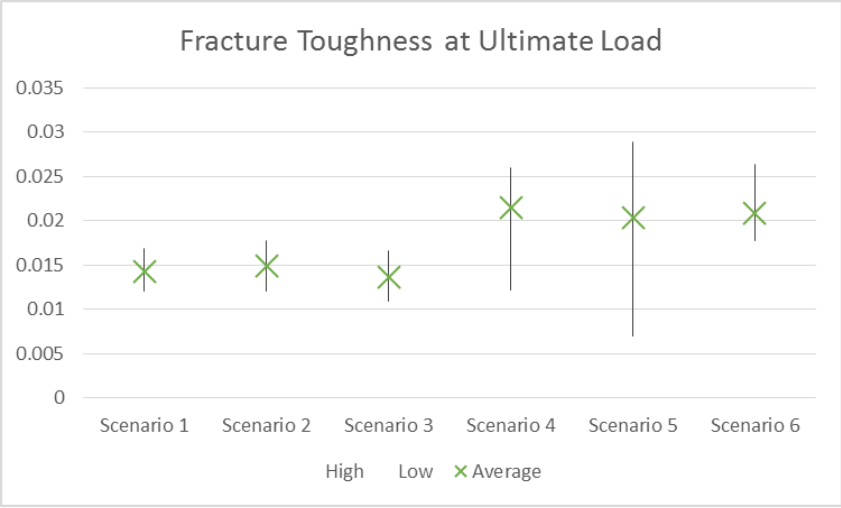


Figure 6: Maximum, minimum, and average fracture toughness at ultimate load for all scenarios. Scenarios 1, 2, and 3 used 12.7 mm thick PMMA plates while scenarios 4, 5, and 6 used 25.4 mm thick plates.

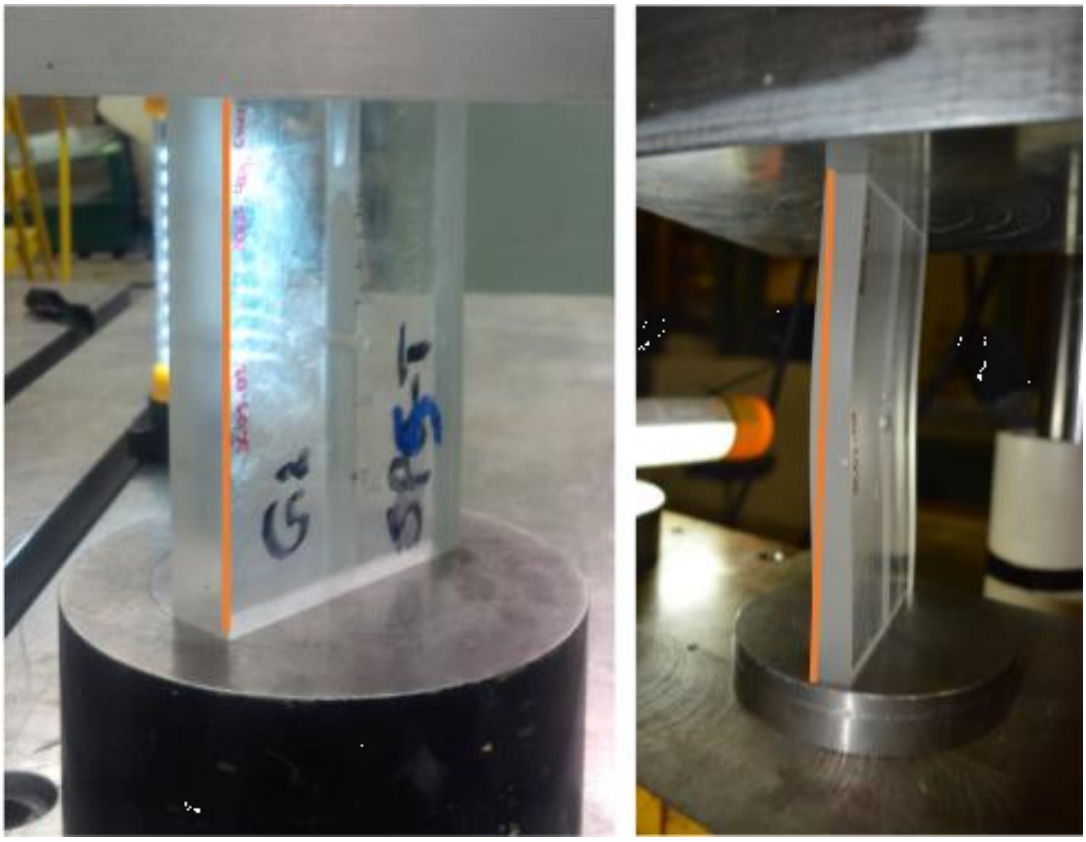

Figure 7: Left, thicker sample SC05-02 under ultimate load compression with no visible buckling. Right, thin sample SC01-05 under ultimate comprssion showing typical buckling of the thin samples

The complete length of the fracture is considered when calculating the fracture toughness at the ultimate load. The fracture length average varies between 26.5 mm to 33.0 mm. This represents a large portion of the sample as the fracture grows from the center towards both compressed ends. Since the sample length is 152 mm and each arm of the fracture is about 30 mm with a gap in the center of 6.3 mm, the fracture tips of the upper and lower portion of the samples are located almost halfway between the loading face and the center of the sample. Therefore, some errors would be generated by using the ultimate load approach as the collected data could be influenced by boundary conditions effects (end effects from frictional restraint). This is noticeable in the coefficient of variability of scenarios 1 and 2. Consequently, the fracture toughness data were analyzed at the point where the fracture length was 15 mm for the thin samples and 20 mm for the thick samples from the fracture initiation point. A slighter longer distance was used for the thicker scenarios as the fracture extension of 15 mm corresponded to very low loads suggesting influence from the fracture initiation point. See Table 3 for the summary of these results.

Table 3: Summary of results for scenarios 1, 2, and 3 for 15 mm length fracture and scenarios 4, 5, and 6 for 20 mm length from the fracture initiation point. Scenarios 1, 2, and 3 are made of PMMA of 12.7mm (0.5 in) thick. Scenarios 4, 5, and 6 are made with PMMA of 25.4mm (1 in) thick.

| | $K_I$ (MPa $m^{1/2}$) | | | | |
|---|---|---|---|---|---|
| **Scenario** | **Avera** | **Std. Dev.** | **Cov** | **Length** | **Load** |
| 1 | 0.0188 | 0.0011 | 6% | 15 mm | 51.4 |
| 2 | 0.0180 | 0.0014 | 8% | | 49.4 |
| 3 | 0.0185 | 0.0018 | 10% | | 50.6 |
| 4 | 0.0209 | 0.0067 | 32% | 20 mm | 117.4 |
| 5 | 0.0196 | 0.0064 | 32% | | 110.9 |
| 6 | 0.0183 | 0.0057 | 31% | | 105.0 |

Using the middle point approach, the results from the thinner samples, scenarios 1, 2, and 3, showed improved results by decreasing the coefficient of variability values from 10%, 15% and 14% to 6%, 8% and 10% for scenarios 1, 2, and 3, respectively. Furthermore, the fracture toughness significantly increased in all scenarios. Scenario 1 returned an average fracture toughness of 0.019 MPa·$m^{1/2}$ with a standard deviation of 0.001 MPa·$m^{1/2}$ a 24% increase in fracture toughness from the ultimate load approach. Scenarios 2 and 3 produced an average fracture toughness of 0.018 and 0.018 and 0.018 MPa·$m^{1/2}$ with a standard deviation of 0.001 and 0.002 MPa·$m^{1/2}$ a 17% and 26% increase in fracture toughness from the ultimate load approach. Therefore, it can be concluded that for the thin samples the ultimate load approach provides a much better estimation of the fracture toughness of the interface.

On the other hand, for the thicker samples, scenarios 4, 5, and 6, the results were more scattered. This is demonstrated by the significant increase in coefficient of variability from 22%, 26%, and 13% to 32%, 32%, and 31%,shown in Figure 8. The fracture toughness had an slight decrease in scenarios 4, 5, and 6 for the middle point approach. The ultimate load results present significantly less scatter of data while conserving almost the same values of fracture toughness of those of the middle point method. Although a 20 mm fracture length was considered, this represented a significantly smaller area of fracture than the area of the ultimate load to break due to the larger thickness. The proximity of the fracture tip to the center of the sample, the small fractured areas, and the small loads inputs suggest that the results from the middle point approach for the thicker samples are influenced by the damage from around the initiation point. This suggests that the results from this analysis method are not representative of the fracture toughness in the thicker samples and the improvement in results from the thinner samples is the consequence of decreasing the amount of buckling that each sample was subjected to at high loading levels. Therefore, it can be concluded that the middle point approach is not suitable for the analysis of results of the thicker samples.

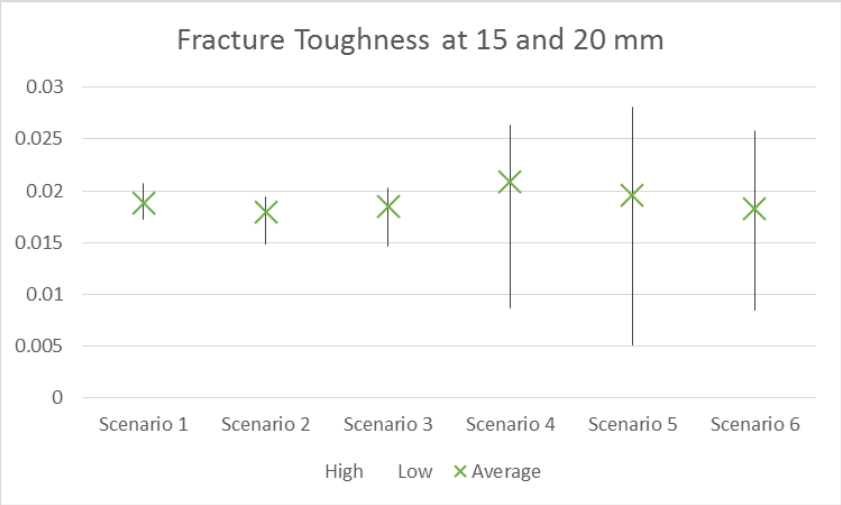


Figure 8: Maximum, minimum, and average fracture toughness at 15mm fracture length for scenarios 1, 2, and 3, and 20mm fracture length for scenarios 4, 5, and 6. Scenarios 1, 2, and 3 used 12.7mm thick PMMA plates while scenarios 4, 5, and 6 used 25.4 mm thick.

It is important to note that the fracture toughness for all values does not surpass that of the virgin sample and all the fracture toughness values are equivalent to those of rigid polymer foams, cork, or polymers elastomer such as ethylene-vinyl acetate EVA (Ashby et al., 2007). However, the fracture toughness values among all scenarios are similar through both evaluating methods except for scenario 4 ultimate load approach as previously mentioned. Similar results are produced from not having a large enough change in bonding stress to produce significant change in the cohesion of the interface. Additionally, a small difference in the recorded fracture lengths has a large impact on the final fracture toughness result. The length was hand drawn during sample testing and the accuracy of the markings might vary by ±2 mm. A more rigorous measuring process is needed for the exact determination of the fractured length and its corresponding area.

**DISCUSSION**

In order to produce different levels of cohesion through thermal bonding, a significantly large stress difference must be exerted on the interface during the cooking time, as suggested by Washabaugh & Knauss (1995). However, a more sophisticated cooking setting should be used to achieve a wider variation in cohesion strength.

Additionally, some samples were damaged during the preparation process while milling the loading sides and drilling the initiation point. This damage is generated by the vibration of the machine and the intrinsic nature of shaving material off in a surface milling machine. The damage around the center hole is

considered a sign of a weakened bond as damaged samples SC04-02 and SC05-02 resulted in much smaller fracture toughness values. This was addressed by excluding these results from the final analysis.

A more rigorous measuring methodology is now being designed to accurately assess the length and area of the debonded fracture zone. Similarly, the assumption that the fracture extends linearly across the interface should be revised to see the effects of this assumption on fracture toughness calculations. Image processing of the pictures was considered during this study, however the recorded photographs had some perspective distortions and resulted in discrepancies between the manually measured data vs. the image processed data. A more advanced fracture growth tracking method is being designed

**CONCLUSIONS**

Controlled cohesion is achievable in PMMA although similar fracture toughnesses were observed due to insufficiently large changes of stress when heating. Heating time can also be extended to control degree of cohesive bonding.

PMMA tested in a stable fracture propagation configuration gives good insight into fracture growth in real time because the leading edge of the propagating fracture can be observed and measured to a precision of better than a millimeter throughout the test without the use of special equipment (e.g. a high-speed camera). The thermal bonding technique also offers an alternative path to create analogue specimens for physical simulation of processes such as hydraulic fracturing in natural fractured rock mass.

Ultimate load analysis yielded good results for scenarios 4, 5, and 6 (thicker samples), while middle point extension analysis yielded good results for scenarios 1, 2, and 3 (thinner samples). This is because at ultimate loads, the thinner samples were influenced by buckling. Errors were addressed using the middle point approach, but it did not improve the quality of results for the thicker samples as they did not experience buckling. Therefore, the ultimate loading approach is reliable for data processing and it is applicable for data analysis of this test.

Most importantly, it was proven that compressional loading of the interface normal to the loading plane is a good testing method for stable controlled fracture toughness determination. The slow fracture growth permitted measurements in real time making it possible to calculate incremental fracture toughness through various parts of the test. These results have interesting implications for testing of rocks and other brittle materials, and will help us develop analogues for physical simulation of processes such as hydraulic fracturing in a jointed rock mass.

**Acknowledgements**

The authors acknowledge the help of William-Henri Sellier, Douglas Hirst and Anne Allen from the University of Waterloo for their assistance throughout this study. This research is supported by the Natural Sciences and Engineering Research Council of Canada (NSERC).

# Appendix C: Non-Destructive Testing Journal Article[2]

[2] The contents of this appendix have been incorporated within a journal article that will be submitted for publication in the Journal of Geotechnical and Geoenvironmental Engineering. Hassan, S., Gomez Rodriguez, D., Cascante, G., Basu, D., and Dusseault, M., "Effects of a fracture on ultrasonic wave veology and attenuation in a homogeneous medium".

# Effects of a fracture on ultrasonic wave velocity and attenuation in a homogeneous medium.

Sabah Hassan[3], Diana Gomez Rodriguez[4], Giovanni Cascante[5], Dipanjan Basu[6], C Eng., M. ASCE, and Maurice Dusseault[7]

## Overview

Nondestructive acoustic testing is used to assess damage in infrastructure as a function of the elastic wave velocity and attenuation variations. This study focuses on understanding the effects of a thin fracture on ultrasonic elastic wave velocity and attenuation. Experiments were performed on the effects of a thin interface fracture within Polymethylmethacrylate (PMMA) specimens. Wave velocity and attenuation were measured across the width of the homogeneous specimen using the ultrasonic pulse velocity (UPV) direct transmission method. Seventeen specimens (12.5 mm and 25.4 mm thicknesses) were tested under three different conditions. First, the intact annealed interface was tested; then, specimens with a small hole perpendicular to the interface and milled ends were tested; and finally specimens containing a centre hole and an induced fracture at the interface were tested. Four extra specimens, two annealed and two solid, were tested during the fracture growth process under uniaxial strain-controlled test. The results reveal that wave velocity shows a marginal reduction up to 4% when damage in the form of a thin fracture is present; whereas there is a reduction of up to 60% in attenuation readings. The findings confirmed the reliability of using wave attenuation to identify the presence of fractures in UPV condition assessment of construction materials.

**Keywords**: Ultrasonic Pulse velocity, fracture, attenuation, PMMA.

## Introduction:

Elastic wave propagation methods are commonly used in nondestructive testing (NDT) of materials such as rock, soil, and concrete because at low strains, wave propagation parameters depend on

[3] Graduate Student, Department of Civil and Environmental Engineering, University of Waterloo, 200 University Avenue W, Waterloo, ON N2L 3G1, Canada, E-mail: shalfart@uwaterloo.com
[4] Graduate student, Department of Earth and Environmental Sciences, University of Waterloo, 200 University Avenue W, Waterloo, ON N2L 3G1, Canada, E-mail: dmgomezr@uwaterloo.ca
[5] Professor, Department of Civil and Environmental Engineering, University of Waterloo, 200 University Avenue W, Waterloo, ON N2L 3G1, Canada, Telephone: 519 888 4567, E-mail: gcascant@uwaterloo.ca
[6] Associate Professor, Department of Civil and Environmental Engineering, University of Waterloo, 200 University Avenue W, Waterloo, ON N2L 3G1, Canada, Telephone: 519 888 4567, E-mail: Dipanjan.basu@uwaterloo.ca
[7] Professor, Department of Earth and Environmental Sciences, University of Waterloo, 200 University Avenue W, Waterloo, ON N2L 3G1, Canada, Telephone: 519 888 4590, E-mail: mauriced@uwaterloo.ca

the elastic material properties. Currently, UPV is being used in various fields such as medicine, chemistry, physics, biology, and engineering. Among NDT methods, the ultrasonic pulse velocity (UPV) method is the most used in practice. Ultrasonic waves are generated by different sources such as piezoelectric, laser, electromagnetic, or mechanical transducers (Ensminger & Bond, 2011). Piezoelectric transducers are used in UPV testing to both transmit and receive compressional waves (P-wave), and are used in this research.

Stable fracture growth is performed under uniaxial compression in a special configuration allowing stable propagation of the fracture, such that, as the load increases, the length of the fracture increases without complete rupture. This provides a way to calculate the fracture toughness at any time during the test. By contrast, standard fracture propagation tests use unstable propagation, reaching a maximum load when the fracture initiates and propagates "instantly" (Tattersall & Tappin, 1966; ASTM, 2001; ASTM, 2010), and only one value of fracture toughness can be calculated.

A transparent material allows visual tracking of fracture growth in real time of a bonded interface. Polymethylmethacrylate (PMMA) is selected for this purpose as it exhibits elastic and plastic deformation prior to catastrophic failure. This plastic has been widely studied as a material resulting in well-defined behaviour data, particularly in fracture characterization (Ayatollahi *et al*., 2015), and it has been used previously as an analogue material to study rock (Rubin, 1983). Furthermore, PMMA can anneal itself through thermal bonding when subjected to high pressure and temperatures for a given period of time (Yang, 2011), providing the possibility of creating specimens under conditions or scenarios that produce a specific bond strength of an interface.

Although the UPV method has been used for several decades to characterize materials (Hertlein, 2013), there is no reported study of using this technique for the condition assessment of PMMA with a stably propagating internal interface fracture. We investigate the interaction between thin fracture growth and pulse velocity and wave attenuation for a group of PMMA specimens under different load conditions. This has allowed us to better understand the fracture growth mechanisms along interfaces in materials under compressive loads.

## Background

### *Ultrasonic wave parameters*

The UPV technique is used in accordance to the American Concrete Institute (ACI 228.2R-13) to monitor the quality of natural rocks and concrete elements (Hertlein, 2013; Malek & Kaouther, 2014), to quantify environment effects on geomaterial and concrete (Chen *et al*., 2015; Duan *et al*., 2011), and to determine material elastic properties (Ensminger & Bond, 2011). In UPV, two piezoelectric

transducers with a frequency range of 20-100 kHz, are placed on opposite sides of the element being tested. A coupling material such as grease, petroleum jelly, or glycerin ensures full contact between transducers and the object being tested (Krautkrämer & Krautkrämer, 2013). This test is performed by emitting an ultrasonic wave pulse that passes through the material and is collected at the other side so that the velocity and attenuation can be measured. Moreover, the waveform amplitude is used as a measure of wave attenuation inside the medium. In a homogenous solid, the pulse velocity $V_p$ is calculated as (ASTM C 597-02, 2003):

$$V_p = \frac{L}{T} \tag{1}$$

where $L$ is the distance between centers of the transducers' faces and $T$ is the travel time.

The two wave characteristics that influence the measured waveforms are the wavelength ($\lambda$) and frequency ($f$), related to the wave velocity as

$$V_p = f.\lambda \tag{2}$$

Although velocity can be reliably used to characterize materials under certain conditions, UPV is not very sensitive to identify velocity heterogeneities in a material, and in the case of small-scale internal damage, wave attenuation from UPV test results is a more accurate measure (Chai et al., 2011; Kirlangic, 2013).

Attenuation is the decay of ultrasound intensity during wave propagation through a medium, and it can be evaluated from the following equation (Ensminger & Bond, 2011):

$$A_z = A_o.e^{-z\alpha} \tag{3}$$

Here:

$A_z$ and $A_o$ are the wave amplitudes at the beginning and after propagating a distance z in a medium, and $\alpha$ is the attenuation coefficient.

Attenuation arises from different mechanisms such as wave spreading, scattering, absorption and mode conversion ( Santamarina & Fratta, 1998; Hellier, 2001). Wave spreading is simply geometrical attenuation as a wave propagates out from a source, spreading outward in all available directions. Scattering is the reflection of waves at acoustic impedance oriented differently than the original direction of propagation. The conversion of wave energy to other forms of energy such as heat is known as absorption. Mode conversion occurs when an acoustic wave encounters an interface between materials of different acoustic impedance and part of the energy is transformed into different wave forms and is reflected or refracted along different ray paths.

The sensitivity of wave attenuation to inhomogeneities at many scales has motivated research into a combination of wave velocity and attenuation data to characterize defects and heterogeneities in different materials (Aggelis et al., 2009; Chai et al., 2011; Yim et al., 2012). For example, Gaydecki et al. (1992) proposed a frequency-dependent attenuation to assess the aggregate particle distribution in a concrete specimen. Moreover, Philippidis and Aggelis (2005) reported a significant effect of aggregate quantity on the wave velocity, whereas the attenuation was more influenced by the aggregate geometry. Chaix et al. (2003) evaluated thermal damage (microcracking) in concrete from wave attenuation data. Cerrillo et al. (2014) used ultrasonic P- and S-wave, on granite specimens to investigate the feasibility of wave attenuation to quantify the physical-mechanical properties of the medium. They pointed out the reliability of wave attenuation to assess properties such as apparent density, compressive strength, and dynamic elastic parameters.

***Fracture propagation in homogeneous medium***

Fracture propagation has been investigated extensively to better understand material failure of material because of crack nucleation, growth, and coalescences. Macroscale physical simulations have been carried out in a various materials, both homogeneous and heterogeneous such as concrete, metals and ceramics, and, to a lesser extent, plastics (Ayatollahi et al., 2015; Haeri *et al*., 2013; Jiefan *et al*., 1990; Yang, 2011). Standard procedures, such as the three-point test for concrete, exist to characterize fracture propagation in various materials (Gerstle, 2010). The three-point test measures the fracture work and flexural properties by loading rectangular prism at three points: two located at specimen ends for support, and the load is applied vertically at the centre between the supports (Tattersall & Tappin, 1966). A variation is the four-point test where two symmetrically placed vertical loads replace the single load to create a section between the two loads where the bottom fiber of the rectangular prism is in a uniform state of tension. This allows fracture to initiate at any flaw along this section and not merely under the single point where the tensile stress is a maximum (ASTM INTERNATIONAL, 2010). In metals, the tear test is standard procedure to measure fracture toughness (ASME, 2001), and the Charpy test is also widely used (Tattersall & Tappin, 1966).

These methods are standardized because analysis is straight forward and results from different studies are easily compared. The tearing and three-point tests involve loading the material in tension over some period of time, whereas impact tests almost instantaneously propagate the fracture. In all cases of brittle fracture using these tests, it is difficult to measure fracture growth in real time because once some threshold has been passed, propagation is uncontrollably unstable, and only the peak load measurement

can be taken. In the three-point and the impact test, the fracture initiation point is dictated by where the point load is applied or where a notch is placed. Tearing test and four-point tests let the fracture initiate in a flaw within a specified portion of the specimen, and this is regarded as an improvement, but unstable fracture growth remains a major limitation of these test procedures.

We developed and use a controlled fracture propagation test, achieved through propagating a tensile fracture along a pre-determined interface through the use of external compression forces (Gomez Rodriguez *et al*., 2016). Compressive stress methods to examine tensile strength have a long history in rock mechanics: the Brazilian Test is widely used and standardized (Ulusay, 2015). Yang (2011) tested sandstone specimens containing two artificially created coplanar flaws to study fracture coalescence under uniaxial compressive load. Haeri *et al*. (2013) used rock-like specimens under uniaxial compressive load for testing fracture propagation and coalescence of two randomly oriented flaws under uniaxial load. The rock-like specimens were produced from a combination of sand, cement, and water in a cylindrical mold (Fig.1a). Ayatollahi *et al*. (2015) used polymethylmethacrylate (PMMA) to study fracture development in brittle material. A V-notch was used as fracture initiation point and the stepped cottage shaped sample was put under compression and loaded at 0.000075/s strain rate until a fracture was developed from the tip of the notch and eventually reached the other end of the specimen.

In this paper, a similar approach was used to create and propagate a fracture. The specimens were created of two identical solid PMMA rectangular prisms annealed along the long and narrow edge by heating under stress for many hours. The specimens used are of 101.6 mm × 152.4 mm rectangular shape, either 25.4 or 12.7 mm thick (Fig. 1b, 1c). A hole is drilled normal to the interface. Fig. 1c illustrates the growth of a fracture along the bonded (partially annealed) interface as the axial compressive load is increased.

## Methodology and experimental set up

PMMA specimens are used for fracture growth in a brittle material, and ultrasonic measurements are taken at different levels of fracture propagation to study the relative effect of the thin fracture on wave velocity and wave attenuation.

### *PMMA specimen fabrication*

Seventeen (17) annealed PMMA specimens and two (2) solid specimens were tested ultrasonically at different stages from the beginning to the end of specimen creation and testing; of the 19 specimens, two annealed and two solid specimens were tested during fracture propagation under uniaxial compression load.

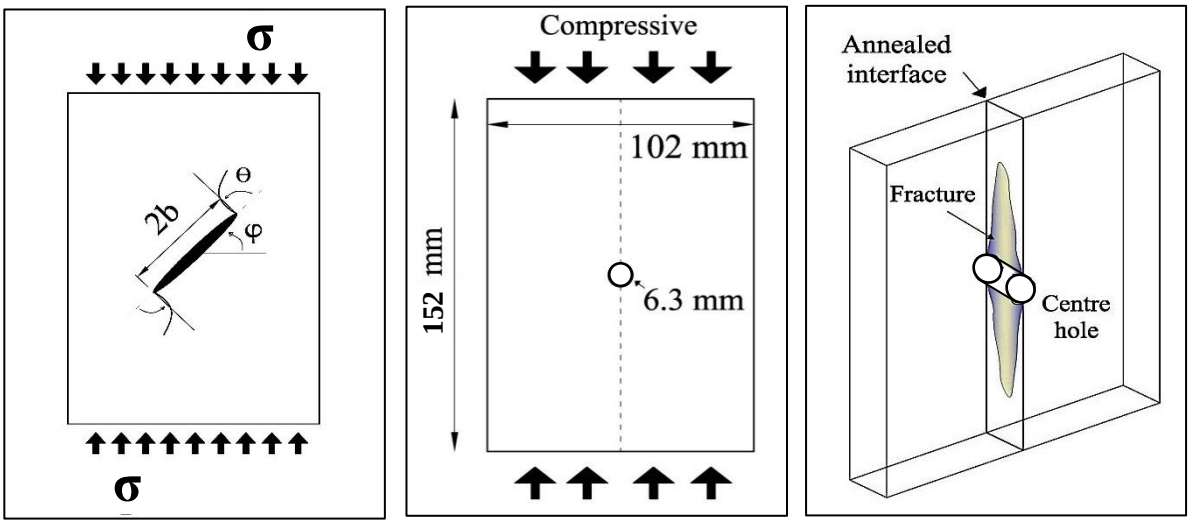


(a) (b) (c)

Figure *1*. (a) Schematic of a general fracture in a specimen during a compressional test,*(Haeri et al., 2013)*(b) schematic of PMMA specimen, and (c) perspective view of PMMA specimen with hole and fracture.

Annealing under different conditions as described in Table 1 generated the 17 specimens with a weak interface, and the two solid specimens were directly cut from a large PMMA sheet. Out of the 19 tested specimens, seven annealed specimens are 12.7 mm (1/2 in) thick while the rest are 25.4 mm (1 in) thick.

Table 1: List of PMMA specimens tested and their corresponding bonding conditions

| | | | | **Fabrication conditions of PMMA** | | |
|---|---|---|---|---|---|---|
| **Specimen #** | Type | Thick. (mm) | No. | Temperature (C°) | Duration (Hrs) | Pressure (KPa) |
| PA-(1-4) | Annealed | 25.4 | 4 | 150 | 6 | 24 |
| PA-(5-8) | Annealed | 25.4 | 4 | 150 | 6 | 12 |
| PA-(9-10) | Annealed | 25.4 | 2 | 150 | 6 | 6 |
| PA-(11-13) | Annealed | 12.7 | 3 | 150 | 6 | 12 |
| PA-(14-16) | Annealed | 12.7 | 3 | 177 | 6 | 6 |
| PA-17 | Annealed | 12.7 | 1 | 177 | 6 | 12 |
| PS-(1-2) | Solid | 25.4 | 2 | - | - | - |

For annealing the interface, two PMMA prisms are adjacently placed in a steel jig that restrains out-of-plane movement but allow compressive stress to be applied on the edges, normal to the plane of the interface. The jig is in the oven, and a steel bar placed on the thin edge to distribute the load, and a

dead weight load is applied to the steel bar. This set up is heated to a temperature of 150$^{o}$ C. After a prescribed time that is set by the desired degree of annealing of the interface, the heating is ceased and the specimen cools in the oven under load. The specimens are then retrieved from the jig and subjected to a first ultrasonic test.

The specimens are then milled on the shortest faces on which the compressive load will be applied to smooth parallel surfaces to be in contact with the loading frame. Finally, specimens are 150 × 100 × 12.7 (or 25.4) mm in size. Then, a 6.3 mm hole is drilled located at the centre of the large face of each specimen and symmetrically through the annealed interface (Fig. 1b).

At this point, a second ultrasonic testing phase is performed to assess the impact of the milling and the creation of the hole in the acoustic signals.

Once this is completed, the specimens are loaded in a MTS (322) frame set on displacement control at 0.1 mm/min (Figure. 2), recording load and displacement continuously. The four specimens ultrasonically tested during fracture propagation had piezoelectric transducers glued on the thin edges after the centre hole was drilled, but prior to loading. These transducers remained during loading and unloading stages until the maximum load was reached.

Fractures initiated from the contact of the interface with the centre hole and propagated along the annealed interface towards both ends of the specimen (Fig. 1c). As specified loads were reached, the fracture length was recorded and a UPV reading taken until the end of the test. A final UPV reading was taken for all specimens once the maximum fracture length was reached and the specimens were retrieved from the loading frame.

***Ultrasonic testing setup***

The UPV setup consists of two transducers, a function generator, an oscilloscope, and a laptop that serves as part of data acquisition and storage system (Fig. 3). Transducers of nominal frequency 54 kHz and 50 mm diameter were used for emitting and capturing the ultrasonic. Plastic transducer holders were created using a 3D printer and connected by two elastic cords to sustain a constant contact pressure on both transducers. Coupling grease was applied between the transducers and PMMA surfaces to reduce signal losses due to air voids. Excitation consisted of a square wave form from the function generator, with a centre frequency of 60 kHz and amplitude of 10 [volt peak to peak].

The signal was sampled at every microsecond for 4000 $\mu$s. The signals are processed using Mathcad 14 to determine arrival times and UPVs. To minimize the effect of random noise and enhance

.

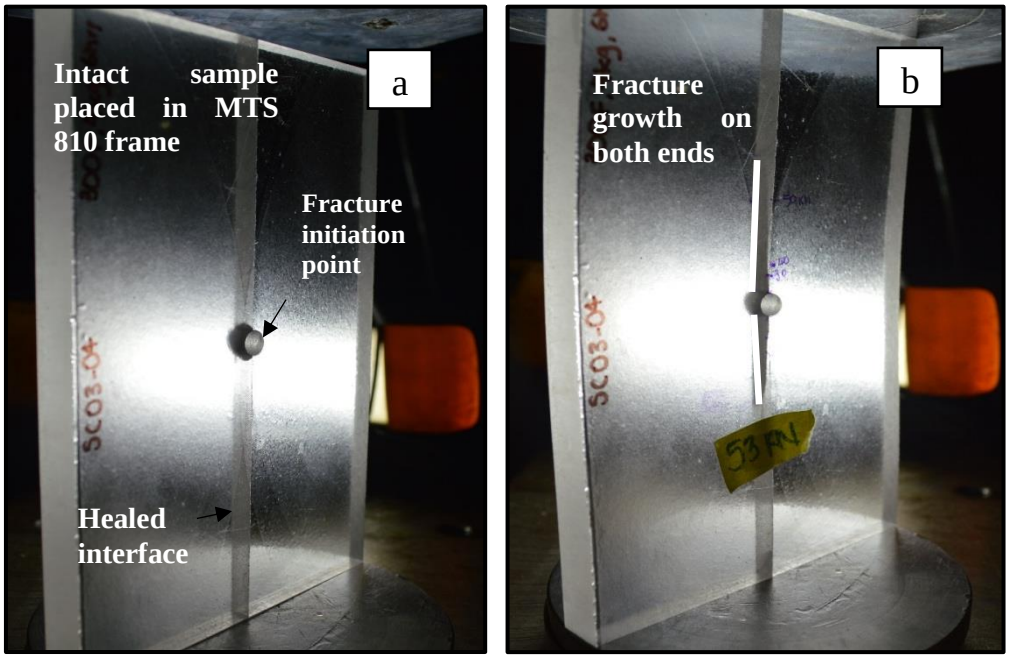


Figure 2. (a) Prepared specimen of dimensions 152 mm by 100 mm (6 in by 4 in), milled short ends and hole in the centre ready to be tested, (b) fully fractured specimen loaded in compressive displacement mode at 0.01mm/min. It exhibits buckling at the ultimate load.

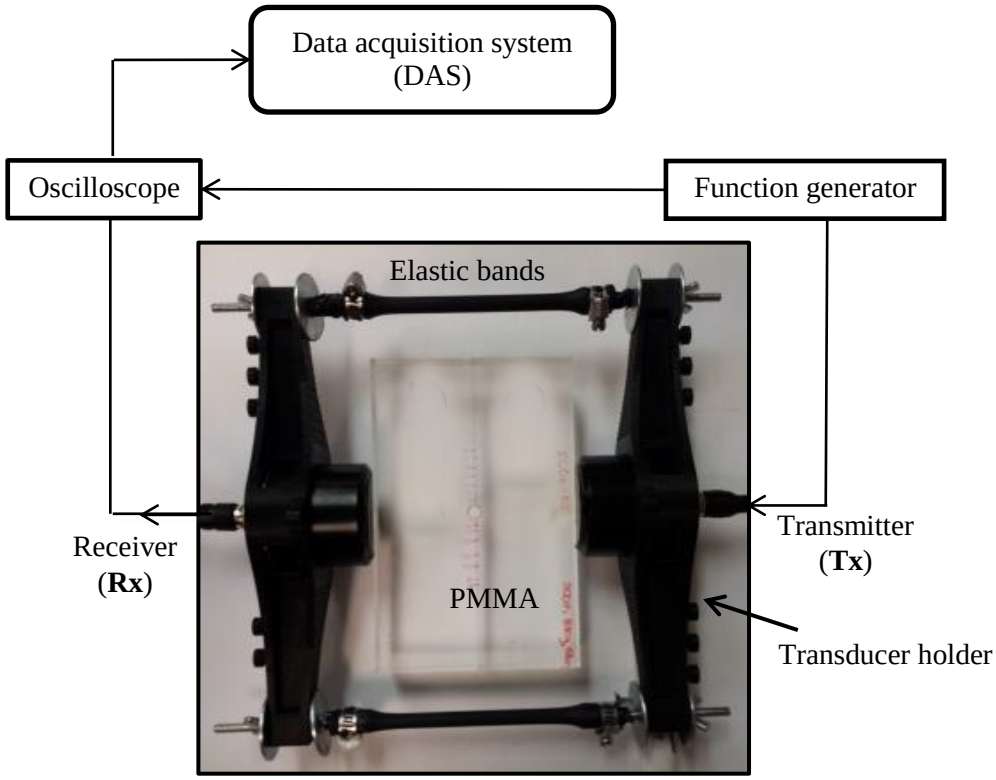


Figure 3. The ultrasonic pulse velocity instrumentation setup using fabricated plastic transducer holder.

the signal quality, the signals were averaged during the UPV test. For this study, average of 16 readings was measured for each individual UPV test carried out with a standard deviation less than 0.0001 [V] which can be considered acceptable. The time signal is then converted to a frequency spectrum using the fast Fourier transform [FFT] technique. The area under this spectrum is proposed as a parameter to quantify signal attenuation during fracture growth.

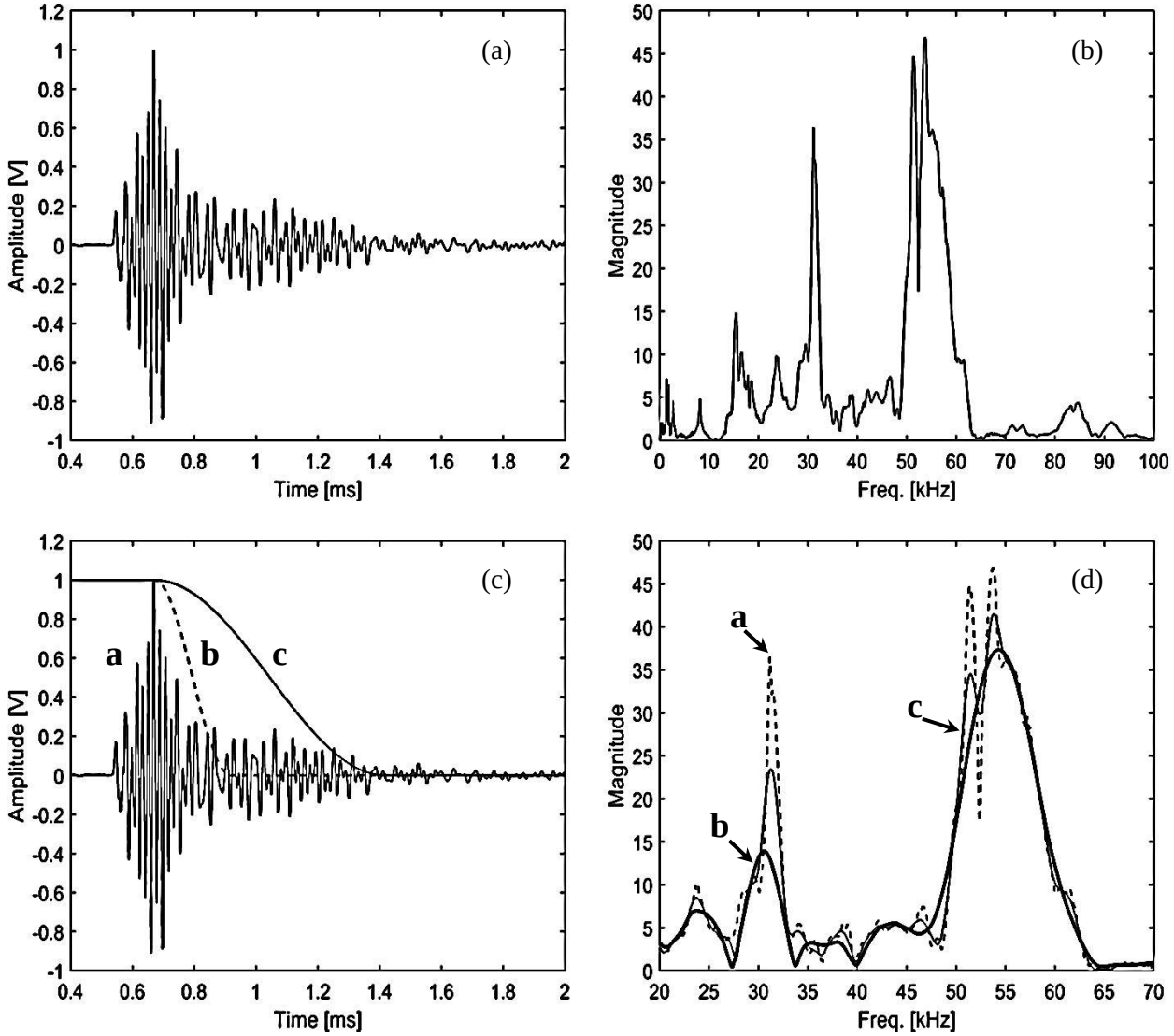


Figure 4**.** Typical measurements**, (**a) sixteen averages in time series**, (**b) corresponding sixteen averages spectrum, (c) signal with applied time widow, (d) signal and windows spectra. where (***a)*** is original time signal and (***b,c***) are time window factors ***0.1*** and ***0.3***, respectively.

Fig. 4a and 4b show the means of the sixteen signals obtained for each test in both time and frequency domains, with standard deviations of $5.7\times10^{-4}$ (V) and $4.37\times10^{-6}$, respectively. The delay time was determined in two ways: by a face-to-face test, and by testing standard test specimens such as aluminum and steel of various lengths. In this study, the delay time obtained was $2\times10^{-6}$ s. This delay time is subtracted from the arrival time determined from the signals to calculate the wave velocity.

For the signals acquired during testing of the PMMA specimens under strain in the load frame, signal processing using a time window is performed to reduce the noise and improve the identification of spectrum peaks. Fig. 4c and 4d show the improvements that occurred when various time windows (called Tukey windows) are used.

## Results and discussion

***Load-displacement behavior of PMMA specimens.***

During the fracture propagation test, the frame constantly measured the applied load and displacement of the actuator. Using this information combined with the information about the geometry of each specimen the average stresses and strains are calculated and plotted (Fig. 5).

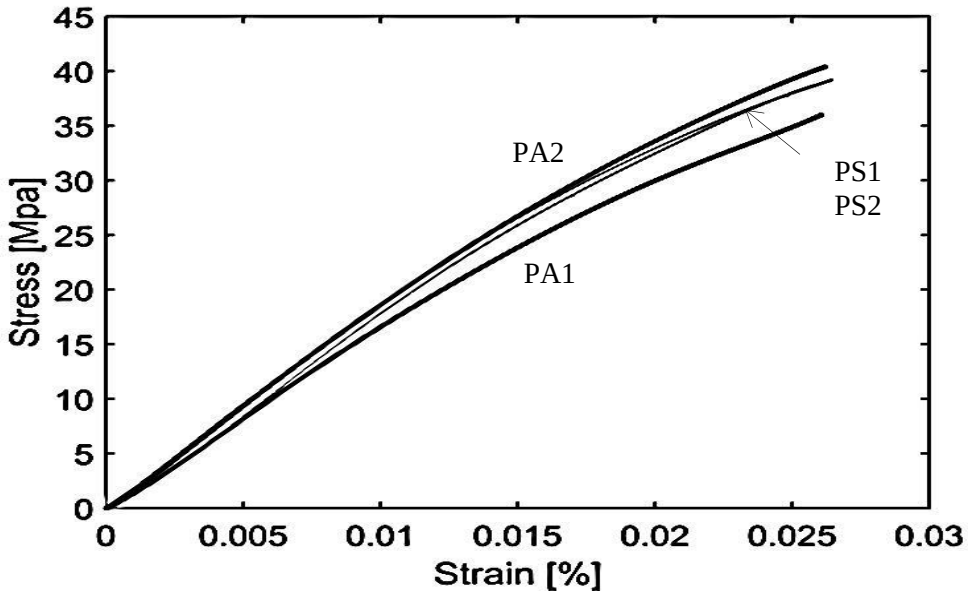


Figure 5. Typical average stress – average strain curves for annealed and solid PMMA specimens.

From the slope of the stress-strain plots, the elastic modulus (*E*) was calculated in the conventional manner to give an estimate of the stiffness of the specimens. Two distinct zones are

identified: the initial part of the curve with a steeper average slope is called the initial zone (zone A in Fig. 6) and the terminal part of the curve with a flatter average slope is called the final zone (zone B in Fig. 6). Thus, two moduli $E_a$ and $E_b$ are determined from the stress-strain plots (Fig. 6). In this figure, the regions are shown for a typical PMMA specimen.

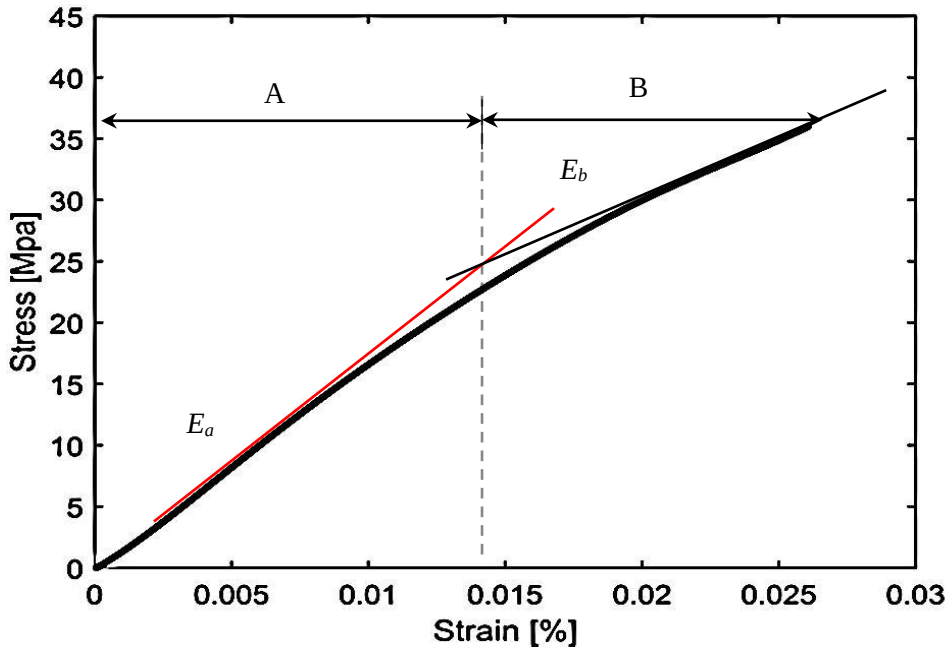


Figure 6**.** Typical defined zones in stress-strain curve of PMMA specimen. where A and B are initial and final zones, respectively.

This procedure was repeated for the four specimens in which UPV tests were carried out during fracture propagation. The results are summarized in Table 2. The final zone moduli, which represent the system stiffness when the fracture has propagated some distance along the interface, are roughly consistent at about 55% of the zone A system stiffness.

Table 2: Elastic moduli of specimens tested under strain controlled test.

| **Static elastic modulus, *E* [GPa]** | | | | |
|---|---|---|---|---|
| **Zone #** | PA-1 | PA-2 | PS-1 | PS-2 |
| A | 1.69 | 1.85 | 1.87 | 1.80 |
| B | 0.86 | 1.07 | 1.05 | 0.93 |

The zone A elastic moduli ($E_a$) are close to the values for PMMA found in the literature (1.8 – 31 GPa), as expected, because of the effects of the small circular hole and the fracture propagation along the interface are not having a significant impact. The dynamic modulus of elasticity was determined based

on the UPV measurements and found to be 4.96 GPa for annealed and 4.66 GPa for solid specimens, about three times greater than the zone A static elastic moduli.

Our controlled fracture propagation approach allows fracture length to grow stably as a function of a greater compressive load on the specimen. Fig. 7 is a plot of the load versus the observed fracture length of four PMMA specimens measured. The relationship for the annealed specimens demonstrates approximately linear growth until 90 kN load, thereafter, fracture lengths increased at higher rates with added load. Solid specimens exhibited a linear trend until load 90 kN (SP1), and 120 kN (SP2), respectively, at which point macroscopic fractures formed in the solid specimens and propagated, but at a lower rate than in the annealed specimens, which is the expected behavior because of the low fracture toughness of the annealed interface.

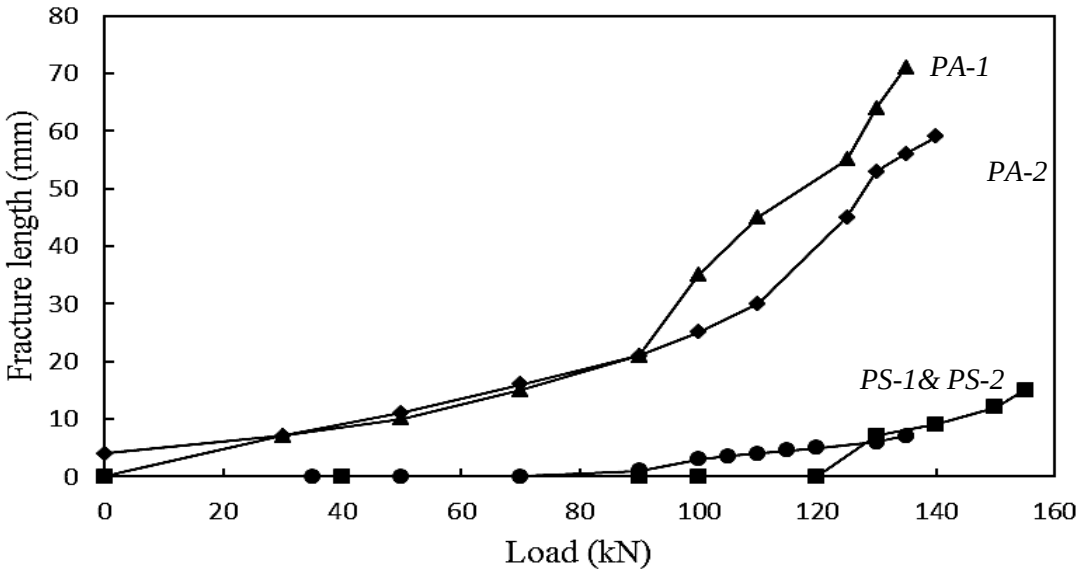


Figure 7**.** Fracture propagation of four PMMA specimens, annealed (PA) and solid (PS), tested under strain controlled test**.**

An interesting outcome from this plot is that each kind of specimens exhibits a similar growth trend, in regards to fracture propagation rate. It is noted that the size of fractures observed in annealed specimens show higher values than the solid ones; whereas the maximum fracture observed in annealed specimens was 7.1cm. In contrast, the maximum value in the solid was 1.5 cm. This can be explained by the existence of the interface line in annealed specimens requiring lower loads to produce fracture. It is worth mentioning here that the fracture orientations in all PMMA specimens were normal to the load direction. Based on these findings, the fabrication method used to produce annealed PMMA specimens provides an effective procedure to monitor fracture growth.

***Fracture interaction with wave velocity***

The UPV measurements of PMMA specimens tested at three (3) scenarios were analyzed to determine the arrival times and P-wave velocities. Fig. 8 shows the ultrasonic pulse velocities of PMMA specimens with different thicknesses (12.7 mm & 25.4 mm) versus the specimen number for all scenarios. The average wave velocities for the thin PMMA specimens were determined for (1) intact to be 2720 m/s ± 12, (2) hole 2718 m/s ± 10, and for (3) damage 2630 m/s ± 10. On the other hand, the UPVs of thick PMMA specimens were found to be 2803 m/s for (1) intact and (2) hole scenarios, respectively. While for (3) damage case the UPV was 2709 m/s. From the test results, it can concluded that wave velocities of the intact and hole scenarios are almost identical with small variations. When comparing the average values of UPVs obtained in testing PMMA specimens at initial and final scenarios (intact and damage) for both thicknesses, only slight differences were observed, approximately equals 2% and 3.6% respectively. These findings highlight the issues that arise from using wave velocity as a single parameter to study the internal condition of interface within PMMA specimen. As the difference between reference initial cases and damage ones cannot be considered as enough indicator to quantify the propagated fracture. Moreover, the variability observed in the results of the thin thickness can be attributed to the testing conditions and the narrow surface area used to take UPV measurements.

Meanwhile, Fig. 9 shows the variations of the UPV determined after testing two PMMA specimens annealed and solid of typical behaviour. In Fig. 9a, the wave velocity was slightly decreased due the influence of fracture within annealed zone when the load exceeds 70 kN. After 125 kN, the wave velocity decreased linearly which may be attributed to the travel path of wave becoming longer than the reference case due to the existence of fracture. Unlike the annealed specimens, the wave velocities of solid specimens did not show any kind of variation because the wave had not influence by the fracture growth which is lower than the annealed one.

***Fracture interaction with wave attenuation in time domain***

The wave characteristics under study in this article are wave velocity and attenuation. As mentioned before, the sensitivity of wave velocity is less than the sensitivity of wave attenuation to any change in the medium. In this investigation, the effect of propagated fracture on signal acquired in both time and frequency domain is studied under different conditions. Fig.10 shows typical waveforms obtained for PMMA specimens 12.7 mm. In this figure, the time signals of the (1) intact case and the case with the (2) hole exhibit a slight reduction in maximum amplitude (13%); while in the (3) damage case, waveforms experienced a noticeable reduction due to the fracture existence (62%). The reduction

of signal amplitude can be related to the absorption and scattering mechanisms (Krautkrämer & Krautkrämer, 2013) due to the presence of the fracture at the annealed zone. Similar findings were obtained for the other PMMA specimens tested using the same procedure.

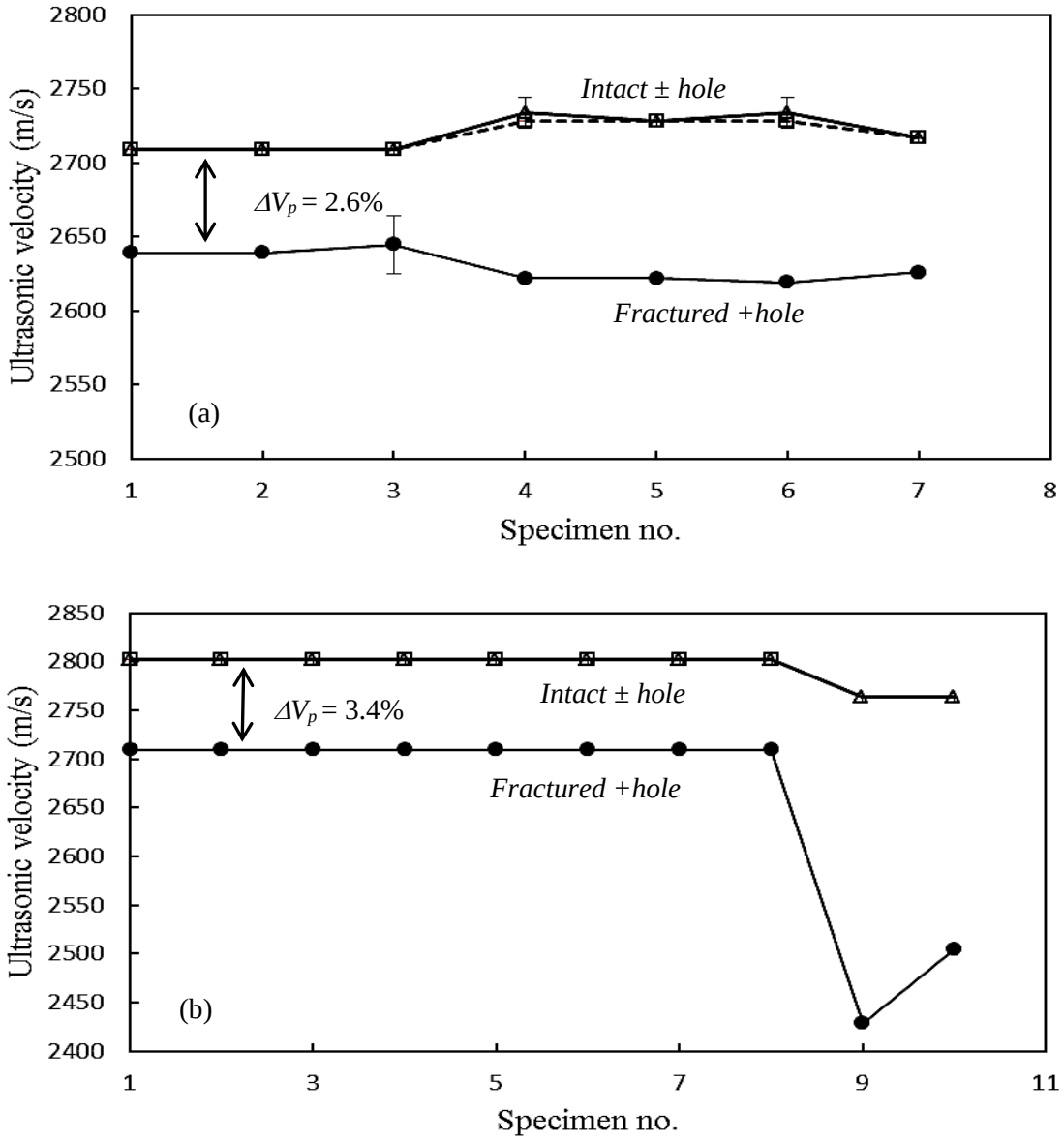


Figure 8**.** Average ultrasonic wave velocity of PMMA specimens (a) 12.7 mm thick. (b) 25.4 mm thick.

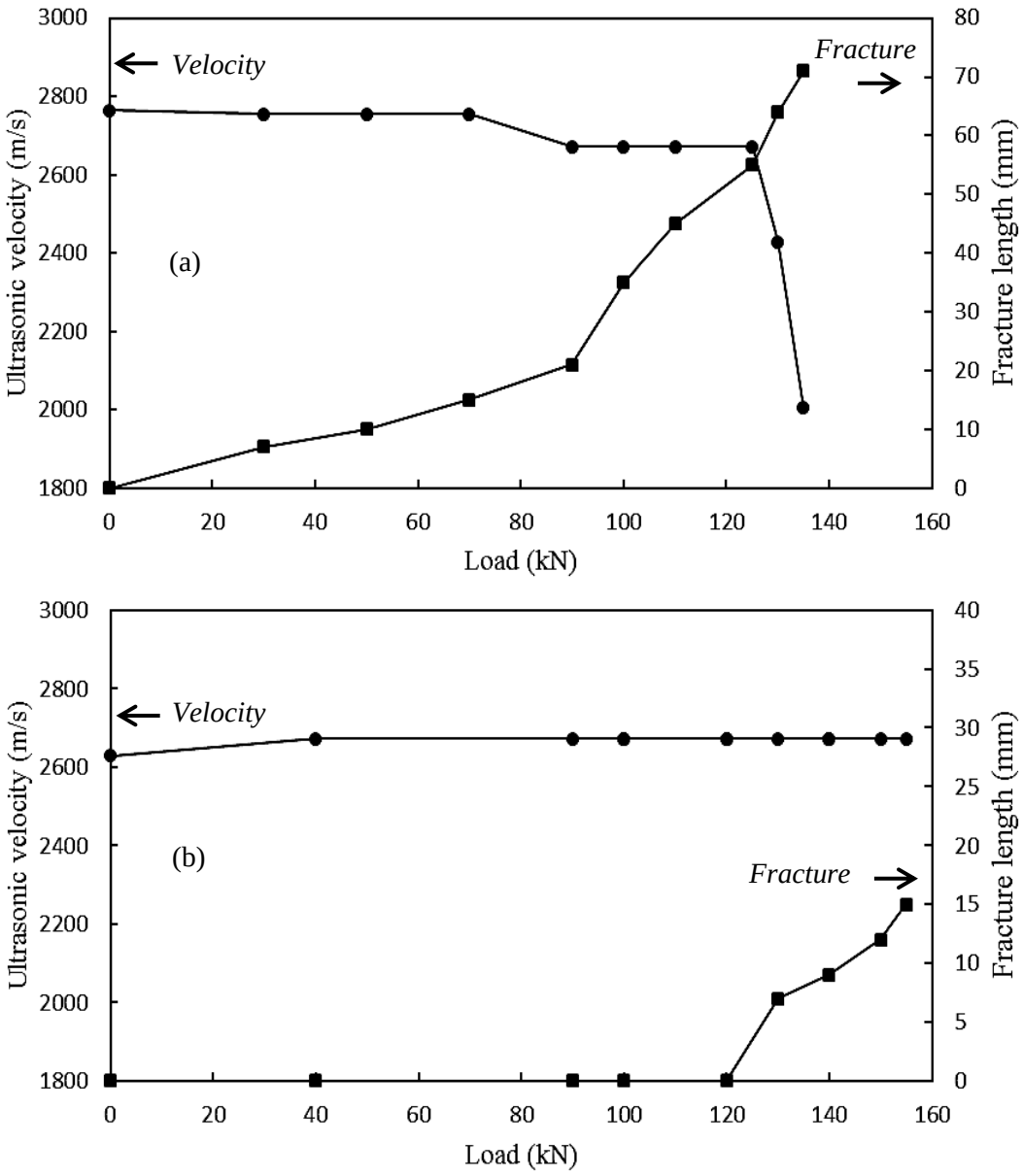


Figure 9. Typical effect of fracture propagation with respect to ultrasonic wave velocity of PMMA specimens (a) annealed condition (b) solid condition.

Thick PMMA specimens of 25 mm show a similar trend to that observed in the thin 12.7mm specimens. Fig. 11 shows typical variations in waveforms with respect to the configuration adopted, the differences between intact and the other two cases were found to be around 13% for hole, and 45% for the damage case. This provides another example of using signal attenuation as a complementary tool to study the interaction between the ultrasonic waves and internal condition of a homogenous medium.

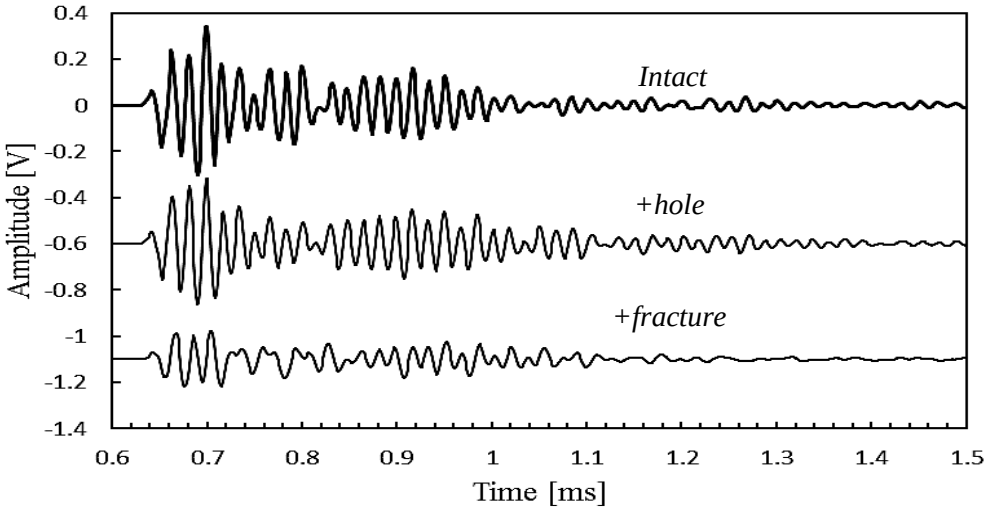


Figure 10. Typical signals in time domain of PMMA specimen (12.7mm) tested at three configurations.

UPV measurements were obtained during the fracture propagation of the PMMA specimens within the loading frame to monitor the impact of fracture growth over the ultrasonic wave energy in the annealed and solid conditions. Fig. 12 shows waveforms corresponding to three selected load steps upon loading, at 10 mm fracture, and at the end of the test for both conditions annealed and solid of PMMA specimens. The observed reductions in maximum amplitudes between waveforms with respect to the initial measurement were 36% and 68% for the annealed PMMA condition, 50% and 76% for the solid PMMA.

***Fracture interaction with wave attenuation in frequency domain***

To quantify the attenuation of waveforms during the fracture propagation, the areas under frequency spectra of signals are calculated. The investigation also studies the relationship between frequency and the fracture existence. This was conducted by defining zones under frequency spectrum as low band zone (LB) 20-40 kHz, and high band zone (HB) 40-70 kHz (Fig. 13). Then, for all specimens, a comparison was made over results of three cases: low band, high band, and total area.

Figs. 13 and 14 show the frequency spectra of the signals obtained of PMMA specimens tested at three configurations; intact, hole, and hole plus fracture. It can be observed from these figures that spectra results confirm the results obtained in the time domain of the testing signals. There were slight variations in spectra between (1) intact and (2) hole scenarios. The existence of hole was not enough to cause attenuation in signals. While the comparison between intact and damage had revealed a noticeable

influence of the fracture on the signal spectrum. It is worth to mention, that all spectra obtained from the PMMA specimens tested at the three configurations exhibit similar patterns.

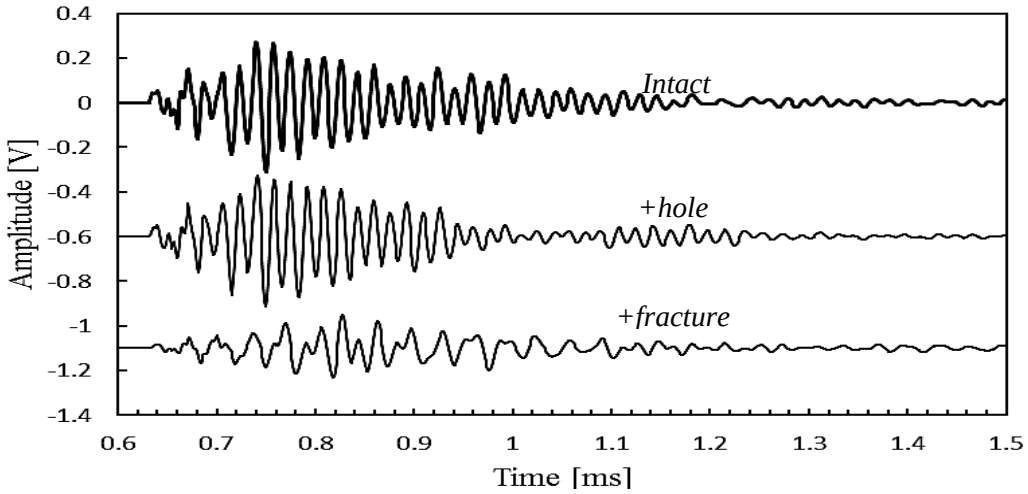


Figure 11. Typical time signals of PMMA specimen (25.4mm) tested at three configurations.

Figs. 13 and 14 show the frequency spectra of the signals obtained of PMMA specimens tested at three configurations; intact, hole, and hole plus fracture. It can be observed from these figures that spectra results confirm the results obtained in the time domain of the testing signals. There were slight variations in spectra between (1) intact and (2) hole scenarios. The existence of hole was not enough to cause attenuation in signals. While the comparison between intact and damage had revealed a noticeable influence of the fracture on the signal spectrum. It is worth to mention, that all spectra obtained from the PMMA specimens tested at the three configurations exhibit similar patterns.

However, the areas under frequency spectra of testing signals at the three configurations were used to evaluate the fracture influence. Then, areas under the low and high band frequencies are examined by defining the limits of these bands. This is beneficial to assess the sensitivity of frequency to the fracture at the interface zone. For example, the difference in total area of the intact case versus that of the hole and damage cases of a typical PMMA specimen were found to be 15% and 52%, respectively (see Fig. 13).

These findings show that the influence of the fracture on the wave energy was higher than hole case. In the case of low and high frequency bands for the annealed specimen, the low bands did not exhibit any variation whereas reduction percentages for high bands were 15% and 57%, respectively.

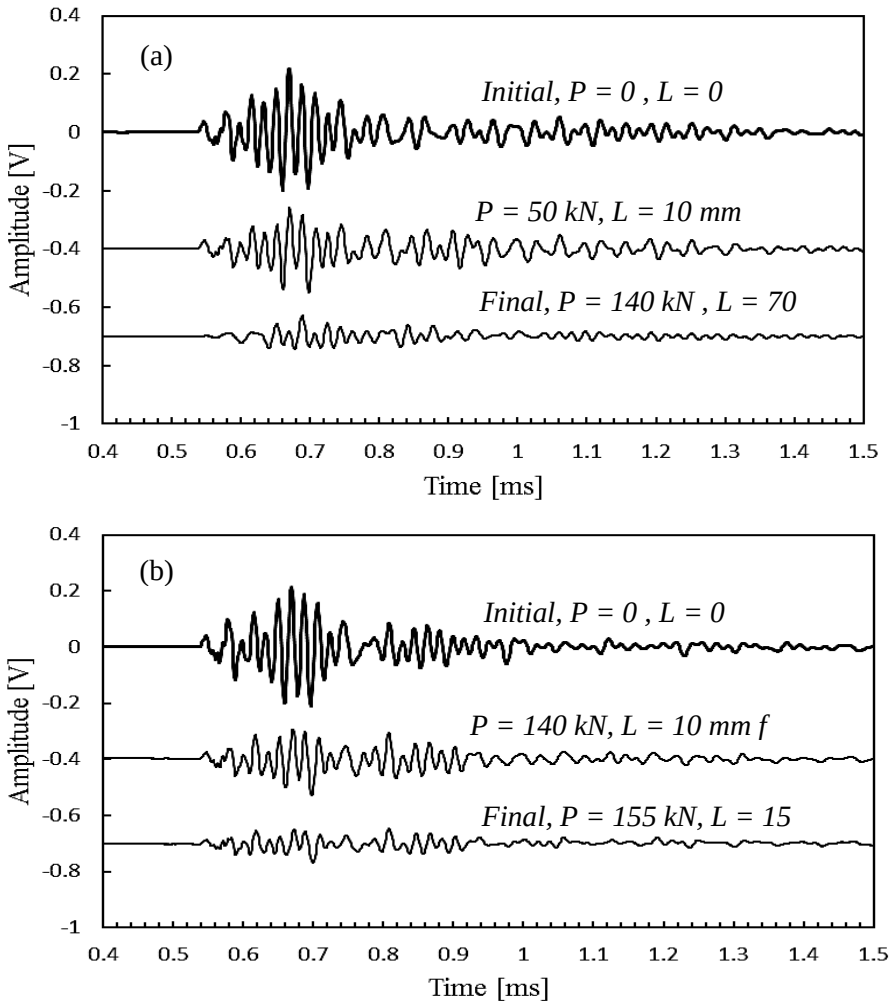


Figure 12**.** Time signals of two PMMA specimens (25.4mm) measured at three different loading steps (10 mm fracture): a. annealed specimen. b. solid specimen. *P* is the load and *L* is the fracture length.

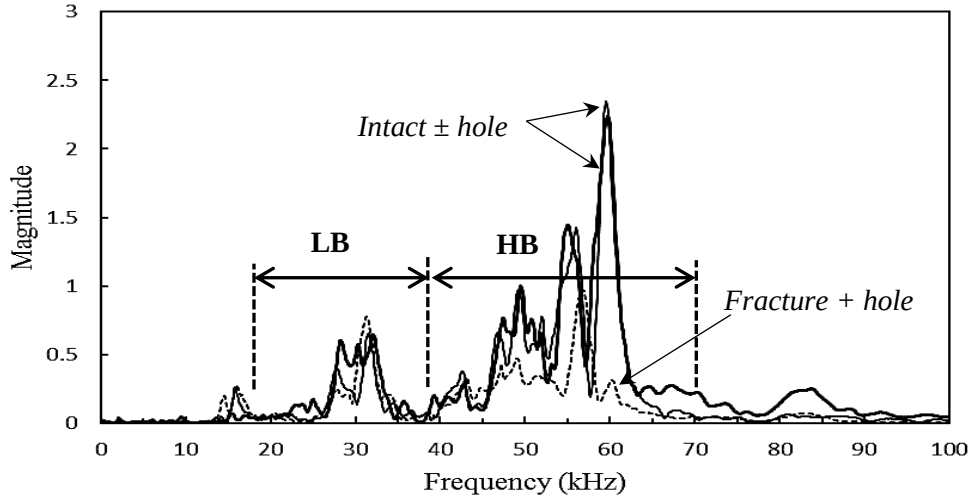


Figure 13**.** Typical average spectra of two PMMA specimens (12.7mm) tested at three cases.

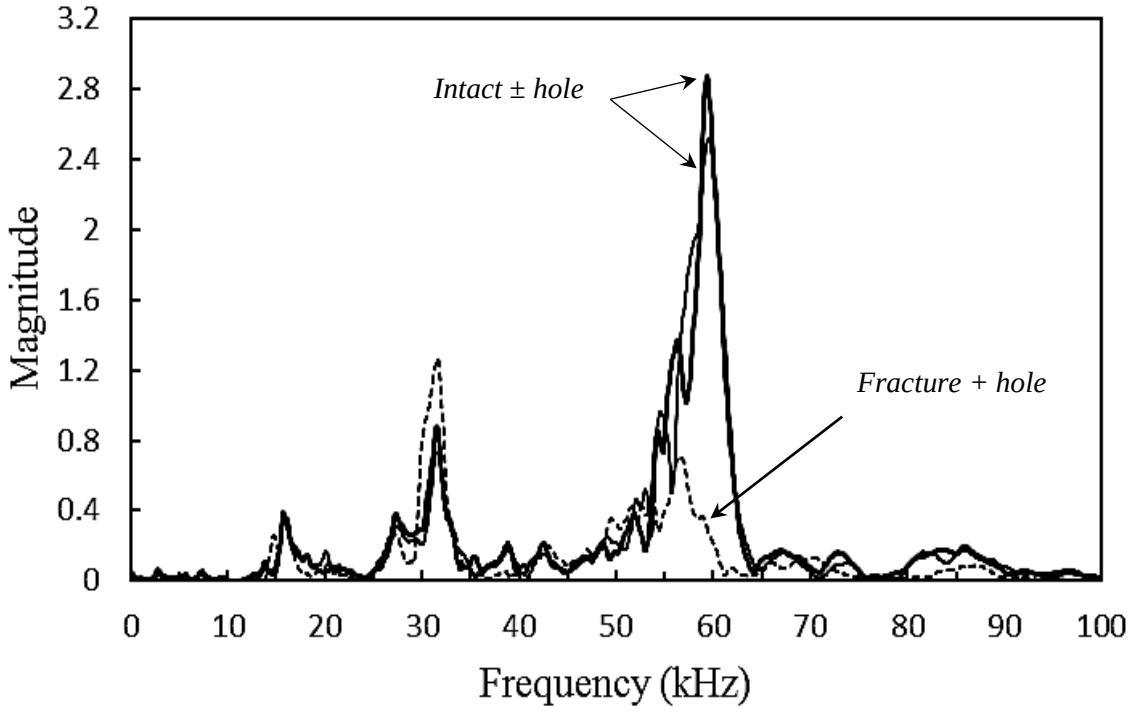


Figure 14**.** Typical frequency spectra of PMMA specimens (25.4 mm) tested under three configurations.

The results of others PMMA specimens revealed similar trend. Figs. 13 and 14 illustrate the correlation observed between the high frequency and the fracture growth in PMMA material. During the test of PMMA specimens under strain loading, ultrasonic signals were acquired. The frequency spectra of these signals were used to evaluate the potential effect of fracture induced under the applied load. The transducers were glued to the PMMA surfaces to help provide a constant bond to obtain identical waveforms during the tests.

The peaks of signal spectra were not easily identifiable and require applying a time window technique to obtain clear peaks. To do so, a time window with factor (0.1) was used to enhance the peaks. Fig. 15 shows the window signals corresponding to selected load steps of a typical annealed specimen. It can be see that frequency spectra become easily identifiable after applying the window. In the case of annealed configuration, the wave velocity exhibits slight variation until the test reaches the load of 130 kN, beyond, the reduction in velocity was pronounced. In contrast, the attenuation of signal spectrum reveals more sensitivity to the fracture at earlier load steps, (Fig. 15).

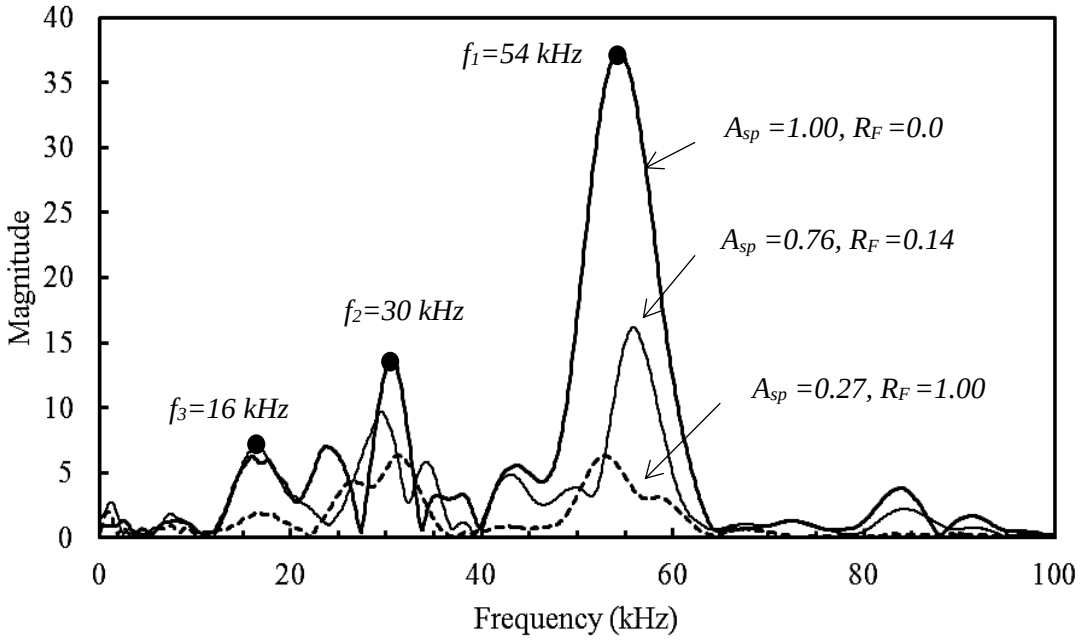


Figure 15**.** Application of Tukey window on signals acquired during testing a typical annealed specimen under strain test in frequency domain. $A_{sp}$ is total area percentage with respect to the reference spectrum, and $R_F$ is fracture percentage with respect to the maximum fracture length.

At the end of the test, the reduction observed in signal attenuation was significant. It is important to note that all PMMA specimens exhibit similar results. Close examination of the spectrum upon loading, reveals three peaks can be identified which are correspond to frequencies *f1*=54, *f2*=30, and *f2*=16 kHz. When the load increased, the peaks in spectra experienced a slight shifting which can be attributed to the fracture conditions in the annealed specimens.

Another interesting outcome is the peak under *f1 = 54 kHz* was the most susceptible to fracture than the other two peaks. The corresponding wavelengths for the aforementioned frequencies (*f1=54, f2=30, and f3=16 kHz*) λ1=5 cm, λ2= 9 cm, and λ3= 16.7 cm for wave velocity of 2715 m/s. The wavelengths determined for the end test results were λ1=4.8 cm, λ2= 8.9 cm, and λ3= 17.8 cm for wave velocity of 2004 m/s. The variations in wavelengths were attributed to the reduction that occurs to the wave velocity.

Fig. 16 shows the results obtained from the signals of a typical solid specimen during the fracture propagation. The findings were identical to that observed in annealed specimen with exception that peaks exhibit slight variations. For the cases of initial upon loading measurements and at 10 mm of fracture propagation, the peaks observed correspond to frequencies *f*1=56 kHz (λ1=4.8 cm), *f2*=30 kHz (λ2= 8.9 cm), and *f2*=15 kHz (λ3= 17.8 cm), respectively. While the values of end test waveform were found to

be *f*1=56 kHz (λ1=4.8 cm), *f2*=30 kHz (λ2= 8.9 cm), and *f2*=16.5 kHz (λ3= 16.2 cm), respectively. Thus, like annealed specimen, the peak under high frequency band ( *f1=56 kHz*) was more susceptible to fracture in comparison to other peaks.

To investigate the interaction between the fracture and wave attenuation, the same procedure was followed after testing 15 PMMA specimens under the aforementioned three configurations. The relation between the fracture with respect of wave energy was quantified by identifying the total, low band and high band areas of wave spectrum.

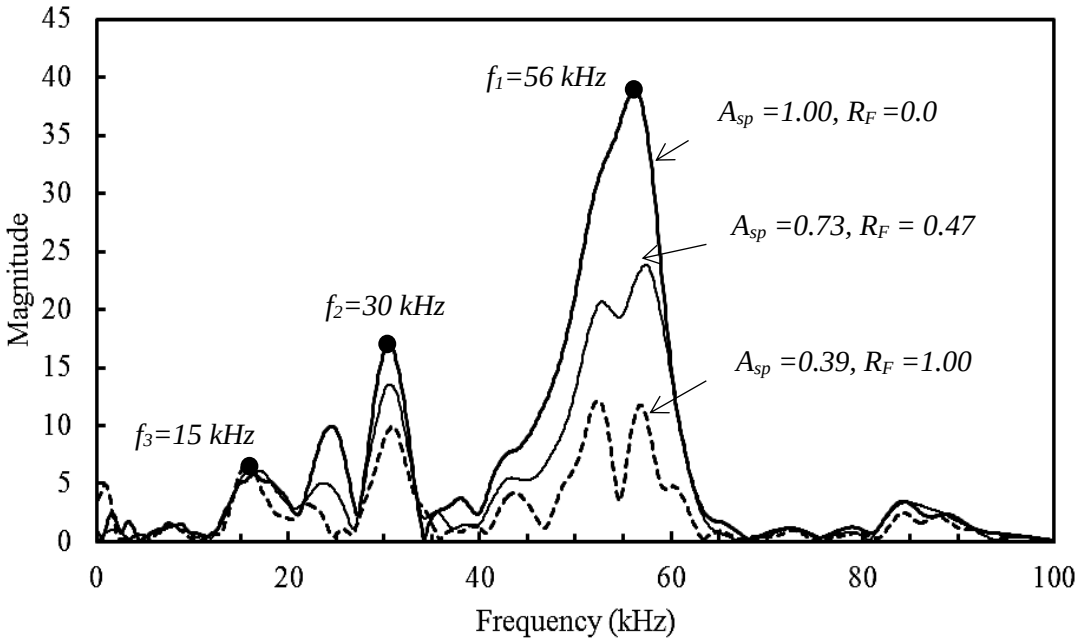


Figure 16. Application of Tukey window on signals acquired during testing solid specimen under strain controlled machine in frequency domain. where $A_{sp}$ is total area percentage with respect to the reference spectrum, and $R_F$ is fracture percentage with respect to the maximum fracture length.

In Fig. 17, the relationship among fracture, spectra areas and load steps is depicted and the gradual reduction of the wave energy in two scenarios, annealed and solid, can be observed. This was accompanied by a noticeable propagation of fracture at the centre lines of both cases. Furthermore, the high band was more sensitive to the fracture propagation than the low band as it was noticed in previous discussion in this article. The sensitivity of wave attenuation to fracture induced by loading can be a potential indicator for quantifying damage in PMMA specimens.

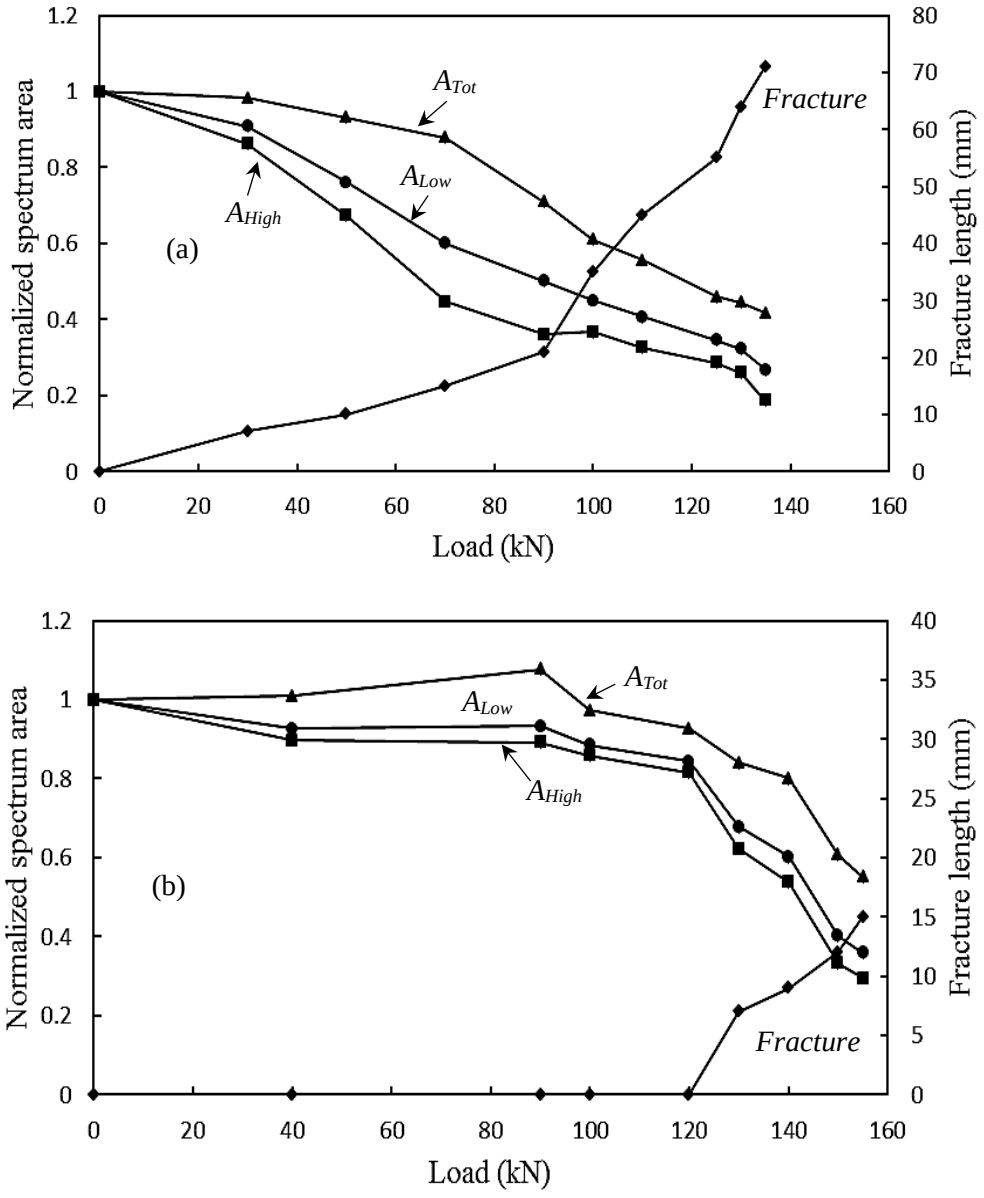


Figure 17 Typical effect of fracture propagation on spectra areas of PMMA specimens tested under strain controlled machine (a) annealed specimen and (b) solid specimen.

## Conclusions

The ultrasonic pulse velocity test was performed on 19 PMMA specimens of two different thicknesses under three scenarios; intact, hole, and hole with fracture. While four PMMA specimens of annealed and solid conditions were tested under strain controlled test during fracture propagation. The direct transmission method was carried out to determine the attenuation characteristics of the fracture in PMMA specimens. In this article, the complementary use of ultrasonic pulse velocity and signal

attenuation was used to characterize the fracture conditions of PMMA specimens. The results show the questionable correlation between wave velocities and fracture. Nevertheless, the results of the time signal and the frequency spectra obtained from the ultrasonic measurements indicated that a change occurred in the condition of the specimens. Moreover, the comparison of frequency spectra confirms the increase of wave attenuation due to fracture growth. The peaks of frequency spectrum were improved by using a time window with factor (0.1). The high frequency ($f > 50\ khz$) was more susceptible to the fracture propagation than the others at lower range. The calculated dynamic modulus of elasticity of the PMMA specimen based on UPV was three times greater than static modulus.

The testing of the PMMA specimens pointed out that a single measurement of the pulse velocity may not be sufficient to detect internal damage in homogenous medium. Therefore, it is recommended to explore the use of attenuation to overcome the limited sensitivity of the pulse velocity measurements to assess the fracture conditions in PMMA material. The most interesting finding of this study is the sensitivity of wave amplitude to characterize the discontinuous (fractures) in geomaterial such as crystalline rocks.